Experimental implementation of complex multiqubit quantum logic gates on platform of linear optics and their applications

a Ph.D. thesis

by

Robert Stárek

Faculty of Science | Palacký University

Olomouc
2022

Abstract

This thesis presents the realization, characterization, and application of three linear optical probabilistic quantum logic gates. The presented quantum gates are controlled-Z with three control qubits, controlled-phase with three control qubits, and quantum Fredkin gate. The construction of these gates relies on two-photon interference and encoding multiple qubits into a single photon. Thanks to their design, the realized gates have a higher success rate than their equivalents constructed straightforwardly from multiple linear-optical two-qubit gates. The relatively high success probability allows us a thorough characterization of the realized gates and demonstrations of their capabilities in various quantum information protocols. Namely, the thesis presents the experimental implementation of protocols for protecting qubits from dephasing and decoherence, protocols for direct non-destructive measurement of non-linear functionals of a density matrix, qubit purification, and approximate quantum cloning. We also study back-action of such direct non-destructive measurement.

The described experiments utilize single-photon generation, two-photon interference and coincidence measurements, inherently stable interferometers, path and polarization qubit encoding, and tomography of quantum states and channels. The corresponding chapter discusses these methods together with relevant experimental imperfections and practical aspects of the experiment.

Keywords: qubit, quantum gate, CZ, Fredkin, controlled-phase, photon, optics, decoherence

Title:	Experimental implementation of complex multiqubit quantum logic gates on platform of linear optics and their applications
Author:	Mgr. Robert Stárek
Advisor:	prof. Mgr. Jaromír Fiurášek, Ph.D.
Consultant:	Mgr. Michal Mičuda, Ph.D.
Study programme:	Optics and Optoelectronics
Institution:	Department of Optics, Faculty of Science, Palacký University
Year:	2022
Pages:	131

Experimentální implementace komplexních multiqubitových lineárně optických kvantových hradel a jejich aplikace

Dizertační práce

Robert Stárek

Přírodovědecká fakulta | Univerzita Palackého

Olomouc
2022

Anotace

Tato práce se zabývá realizací, charakterizací a využitím nedeterministických, lineárně optických logických kvantových hradel. Jedná se o tzv. CZ hradlo kontrolované třemi kvantovými bity (qubity), fázové hradlo kontrolované dvěma qubity a Fredkinovo kvantové hradlo. Hradla byla realizována pomocí dvoufotonové interference, koincidenčních měření a využití více stupňů volnosti jednoho fotonu pro zakódování qubitů. Díky této konstrukci mají hradla vyšší pravděpodobnost úspěchu nežli jejich realizace přímočarým spojením více lineárně-optických hradel. Díky tomu můžeme provést jejich důkladnou experimentální charakterizaci a používat je pro demonstraci různých kvantově informačních protokolů a schémat. V práci jsou uvedeny experimentální realizace dvou protokolů na ochranu qubitu před dekoherencí, protokolu pro přímé nedestruktivní měření nelineárních funkcionálů matice hustoty kvantového stavu, dále tzv. purifikace a klonování kvantových stavů. V případě přímého měření nelineárních funkcionálů diskutujeme i vliv tohoto měření na měřený systém.

Popsané experimenty využívají generování jednotlivých fotonů, dvoufotonovou interferenci, koincidenční měření, inherentně stabilní interferometry, kódování qubitu do polarizace a dráhy fotonů and tomografii kvantových stavů a procesů. Práce popisuje tyto použité experimentální metody spolu se souvisejícími nedokonalostmi a dalšími praktickými aspekty experimentu.

Klíčová slova: qubit, kvantové hradlo, CZ, Fredkin, controlled-phase, foton, optika, dekoherence

Název práce:	Experimentální implementace komplexních multiqubitových lineárně optických kvantových hradel a jejich aplikace
Autor:	Mgr. Robert Stárek
Vedoucí práce:	prof. Mgr. Jaromír Fiurášek, Ph.D.
Konzultant:	Mgr. Michal Mičuda, Ph.D.
Studijní obor:	Optika a optoelektronika
Instituce:	Katedra optiky, Přírodovědecká Fakulta, Univerzita Palackého
Rok:	2022
Počet stran:	131

Acknowledgements

First, I would like to thank my consultant Michal Mičuda for bringing me to the QOLO team, sharing the experimental know-how, and for the great collaboration in all the realized projects. Then I would like to thank Jaromír Fiurásek for his mentoring, sharing his tips and ideas, and the support he provided both in the role of supervisor of my Ph.D. studies as well in the role of head of the department. Next, I want to express my gratitude to Miroslav Jezek for many fruitful discussions, his support, and great patience with the plethora of my questions on various subjects.

Also, I would not be able to achieve the presented results without the help and cooperation of my colleagues Ivo Straka and Michal Dudka. Ivo Straka built and maintained the single-photon source, a crucial and necessary element of all the presented experiments. Michal Dudka provided his expertise in electronics whenever the experiments needed a custom electronic device. Here I must also thank Jaroslav Chmel. He manufactured all the custom-made mechanical elements in the presented experiments, all with great care, precision, and in time. A special thanks also go to Honza Provazník who showed me many nice programming tricks, helped me many times when I got lost in the world of IT and was open to many interesting discussions on various topics. Of course, I also have to thank the administrative workers of the department who keep the department running, albeit my slight tendency to mess up the papers.

Naturally, let me thank all the members of the Department of Optics for keeping the nice working environment and atmosphere, making the department my second home. I would like to thank especially Pepa Hloušek for being so nice office-mate and friend.

I am grateful to my whole family for their continuous support and love. I also would like to especially thank my beloved wife. The list of things for which I am grateful is longer than this thesis.

Contents

Preface

The goal of this thesis is to present the results of my postgraduate research of linear-optical quantum logic gates. The thesis is based on publications [A1–A5].

These publications were focused on the construction and characterization of linear-optical quantum logic gates as well as their applications in specific quantum information protocols. The goal of the presented experiments was to prove the principles of various protocols and strategies in quantum information using the currently available photonic technology. The results presented in the thesis were achieved by an effort of the whole team of researchers. The gates and experiments were designed by my supervisor, Jaromír Fiurášek. Radim Filip was searching for the application of the implemented gates, mainly novel protocols and theoretical concepts. Both professors contributed to data analysis and interpretation and contributed directly to writing the manuscripts. In the early stage of my studies, I was mainly building the experiments and conducting the experiments under the supervision of Michal Mičuda. The necessary part of the presented experiments was the photon source constructed and maintained by Ivo Straka [1].

Let me here explain my personal contribution. In the first experiments with the C^3Z gate [A1] I was responsible for modifying the existing experimental setup [2], writing the acquisition software, and running the experiments. I also contributed to data processing and manuscript writing. In the presented experiments with Fredkin gate [A3, A4] and CCP gate [A5], I built the experimental setup from scratch, developed necessary alignment methods, automated them, performed all measurements and data processing. With my consultant Michal Mičuda, we designed the necessary custom mechanical mounts for optics. Along with other authors, I contributed to writing the manuscript.

In the publications, we had to omit many experimental details to keep the papers short and comprehensive. I tried to repay this debt by detailed explanations of the experimental principles in the Methods section. The goal is to provide the information that was perhaps too technical for the publications but crucial for performing the actual experiment. I skipped the detailed explanation of every used optical component, as it already was carefully done earlier by Martina Nováková (Miková) in her thesis [3]. Instead, I focus on explaining how to set the experiment to be working, mitigate errors and avoid getting lost in data. In my opinion, these aspects are equally important yet often neglected. I hope the Methods section will help anyone who would like to perform similar experiments in the future.

The experimental part reviews the published experiments. Because the used tech-

niques were very similar in all three experiments, I modified the published text to avoid repeating the same information multiple times. In the case of the CCP and Fredkin experiments, I also slightly changed the text structure to reflect my contribution and fit this thesis's scope. In the Fredkin experiment, I also added content that we had to omit in the published paper due to the length.

Olomouc
January 2022

Robert Stárek
starek@optics.upol.cz
starek.robert@gmail.com

Chapter 1

Introduction

The 20th century brought to physics a new direction – quantum physics. Schrödinger, Bohr, Einstein, Heisenberg, Bell, and others discovered remarkable features of nature, such as the principle of superposition, discrete nature of some physical quantities, intrinsic randomness in nature, wave-particle duality, measurement-induced back-action or nonlocality.

With the invention of the electronic computer in the late 1940s, computer science also flourished. In the 1980s, the computer already conquered many fields – physics among them. There was, and still is, a big challenge. How to simulate a quantum system? With the increasing number of particles, the number of simulated parameters grows exponentially.

In 1982, Feynman in his keynote speech [4] suggested using a controlled quantum system as a tool to simulate another quantum system of interest. Later, Deutsch and Penrose introduced the concept of a *universal quantum computer* [5] – a machine that uses the superposition principle and interference to enhance computational power. These ideas, to utilize nature's quantum features in applications, is the central motivation of *quantum information science*. Quantum information science searches for applications of quantum phenomena in computing, communication, simulation, and metrology. It explores the underlying principles and extends classical information science with quantum features.

One of the important questions is: *can a quantum computer outperform a classical one?* Deutsch and Jozsa showed that with the use of superposition, inter-system coupling, interference, and filtering, one could perform some computational tasks exponentially more efficiently than the classical computer [6]. Shor adopted these ideas and introduced an algorithm with a practical application – factoring numbers [7]. His work motivated the progress in quantum information science. Notably, DiVincenzo formulated criteria for a universal quantum computer [8].

Albeit the recent technological progress, the construction of the universal quantum computer is a very difficult task. The question is, what physical system is the best candidate for a quantum computer. Superconducting circuits and atomic platforms (such as trapped ions) appear to be promising candidates. This belief is even strengthened by a recent demonstration from the *Google AI Quantum* group. They came with a specific task at which their superconducting quantum processor clearly outperformed a state-of-the-art classical computer [9]. Soon, a similar experiment with even more (66) qubits followed

[10].

The exponential growth of a quantum system complexity motivates the research for efficient state and process certification methods [11, 12]. A way to study complex quantum systems is to come up with measures that characterize the system, for example the recent cross-entropy benchmarking [9] of superconducting quantum circuits. Sometimes, it is sufficient to know a few elements of a process matrix that could be measured directly [13–16]. It is also possible to reconstruct the process from the tomographically incomplete set of data [17–20]. One possibility is to use prior information about the characterized state, the other is to remove reconstruction ambiguity by selecting a process with maximal entropy [21]. Also, one can directly estimate the quantities of interest [2, 22–27], for example fidelity. The computer memory requirements for the description of a quantum system also scale exponentially. Recently it was, however, found that noisy quantum devices could be described using just a fraction of the original Hilbert space [28].

Aside from computation, other applications emerged, for example, quantum distribution of cryptographic key[29–31], random number generation [32], or sensitivity enhancements in metrology [33, 34]. While solid-state systems appear to be a great candidate for computing, photonic systems are promising for metrology and communication.

This thesis describes the construction and applications of linear-optical quantum logic gates, devices that use photons for manipulating quantum information. We categorize the presented work in the physical discipline of quantum information science and optics. Chapter 2 introduces the concept of linear quantum optics, its strengths, and its weaknesses. I also included a small review of related single-photon technology.

Chapter 3, *Methods and tools*, describes the used notation, key theoretical concepts and discusses in detail the used experimental techniques. Quantum bits, logic circuits, and their theoretical description are introduced. There are sections dedicated to the two-photon interference (Hong-Ou-Mandel effect) and quantum tomography. Both topics are essential to all presented experiments. Our experiments utilized the encoding of quantum bits into path and polarization degrees of freedom of a single photon. This encoding is discussed thoroughly in Section 3.2.2. Section 3.2.3 reviews how to apply the two-photon interference to construct a two-photon quantum logic CZ gate, including mathematical description, analysis of possible experimental imperfections, and practical experimental aspects. The CZ gate is the core of all presented experiments. Another important approach we use in our experiments is *hyperencoding*, which is explained in Section 3.2.4. Sections describing systematic errors and data processing recipes conclude Chapter 3. The majority of experimental details and principles shared by all the presented experiments are contained in Chapter 3, and therefore it is referenced often in the following chapters.

Chapter 4 presents our results published in [A1, A2]. There we demonstrate a linear-optical four-qubit controlled-Z gate. Due to a large number of qubits, the tomographic description starts to be impractical. The work brings a walkthrough for practical verification of quantum processes of similar size. Another new result is the demonstration of a specific quantum gate operating in a decoherence-free subspace [A2]. The protection from decoherence is of great interest because decoherence is a severe obstacle in quantum information processing.

The protection from decoherence is also a topic of Chapter 5 which is based on paper [A5]. We first demonstrate and characterize the linear-optical phase gate controlled by two qubits with a tunable phase shift. The gate serves in a physical simulator of decoherence mechanism on which we tested a protocol for qubit protection. We showed that a quantum state of the environment could be, under some circumstances, driven into a dark state without direct control over it. We manipulated the environment indirectly solely by its interaction with an auxiliary qubit and its subsequent measurement. We also used the described experimental setup, slightly modified, in the other two experiments. First, we tested the improvement of weak-value amplification phase measurements with entangled auxiliary photons [35]. Then we used the gate to prepare a state for attacking a cryptographic protocol for oblivious transfer [36]. These works are not covered by the thesis.

The last experimental chapter, Chapter 6, introduces a quantum Fredkin gate. The chapter is based on our publications [A3] and [A4]. The main scientific contribution of work [A3] was the experimental investigation of direct and non-destructive quantum measurements and their influence on the measured qubits. In Chapter 6, we first describe the design and experimentally characterize the swap gate for photonic qubits [A4] and then the Fredkin gate itself. Then we use it to perform projections on symmetric and antisymmetric subspaces of Hilbert space. These projections serve to measure purity, overlap, Hilbert-Schmidt distance, perform approximate quantum cloning, purification, and a POVM measurement controlled by another quantum state directly and with access to the post-measurement state. We later used the same experimental setup to prepare a quantum state with a remarkable property: measurements on its separable marginals suffice for verifying its three-qubit entanglement [37]. The paper is not covered by Chapter 6, but all principles and techniques needed to prepare such a state are already covered by the thesis. The thesis concludes with a summary of the presented results.

Chapter 2

State of the art

In this thesis, tests of quantum protocols and algorithms are performed on linear quantum optics platform. The goal of this chapter is to briefly introduce photons as a platform for quantum information experiments and the current state of photonics in this field.

2.1 Linear quantum optics

Are photons good carriers of quantum information? The feasibility of preparation, high purity, and great degree of control are the strong aspects in the context of quantum information processing. While photons are a clear choice for communication, due to their robustness and natural transport ability, the use of photons for quantum computation was believed to be unfeasible due to the lack of natural interaction of photons.

The schemes for two-photon interaction rely on the Kerr effect in a nonlinear medium which is alone too weak. In 2001, Knill, Laflamme, and Milburn proposed a scheme [38] for optical quantum computing that used beam splitters, phase shifters, single-photon sources, and photon-number resolving detectors. The proposal showed how to construct probabilistic quantum logic gates and a way how to increase the success probability by gate teleportation and quantum error correction protocols. They called this approach linear-optical quantum computation (LOQC). The core of the scheme is a nonlinear phase shift gate which introduces π-phase shift for a state with two photons while phases of states with one or zero photons are intact. The nonlinear phase shift gate consists of a Mach-Zehnder interferometer with a single ancillary photon in the first input port and photon-number resolving detectors at both output ports. The signal state is coupled into one arm of the interferometer with another beam splitter. There is a set of ways in which each photon can travel through the optical circuit. Based on detector readings, we select only suitable possibilities at the expense of success probability. Simply put, sometimes we have to discard the output of the gate. With the photon-bunching effect [39] on a beam splitter the nonlinear phase shift is achieved. The nonlinear phase shift is utilized for building conditional sign flip gates, also known as controlled-Z gates. More ancillary photons, teleportation schemes and suitable encoding boost the success probability.

The article have had a big impact and more similar schemes emerged [40, 41]. The two-photon interference is a common underlying concept of such schemes [39]. Shortly, successful experimental demonstrations followed [41–48]. The KLM scheme is not the only paradigm of photonic quantum computing. One can utilize quantum correlations in a specially prepared quantum state, and by performing a series of measurements and correction operations, quantum computation is achieved [49–51]. Also, one can utilize the continuous Hilbert space of light quadratures to encode logical quantum bits into superpositions of coherent states and use them for computation [52, 53].

Let us note that one can induce the nonlinearity also with the help of conditional photon additions and subtractions [54]. It is also possible to leverage the strong interaction between matter and light [55]. The matter strongly interacts with the first photon and thus changes its state according to the photon's state. Subsequently, the matter interacts with the second photon and changes its state. Effectively, one photon controls the state of the other. The Kimble-Duan scheme [56] uses a neutral atom in an optical resonator. The current experimental implementation [57] is however demanding. It requires several lasers for trapping the atom in a magneto-optical trap, control of the atoms population and cavity locking. The experiment also required fast optical switching and fast electronic signal processing to implement feed-forward modulation. Another example of a matter-assisted photon-photon interaction uses Rydberg blockade [58] in an ensemble of atoms [59–61]. The matter-assisted interactions pave the way for deterministic quantum gates, but currently the experiments are highly experimentally demanding and difficult to scale. In the end, the linear quantum optics turned out to be a good platform for *proof-of-principle* tests of various quantum algorithms and protocols, such as experimental number factoring [62]. The scaling is currently technologically limited and the requirements for quantum resources are high. Consequently, the more quantum bits are required, the more difficult optical implementation gets. In proof-of-principle experiments, one can partially circumvent this problem by careful experiment design and by utilizing the richness of photonic modes [63]. This can be interpreted as a photonic simulation of quantum computation [64]. This approach can still be combined with the KLM scheme to allow experimental verification of low-dimensional quantum protocols and algorithms with the comfort and flexibility of optical technology [65, 66].

2.2 Single-photon technology

Progress in quantum optics increased the demand for further photonics developments. The sources and detectors of light are constantly improving, as well as various light modulators, integrated optical chips, and optics in general. And vice-versa, the advances in photonics allow further progress in optics generally, including quantum information science.

Typically, the photonic quantum experiment consists of photon generation, manipulation within some optical network and detection. The ideal single-photon source produces on demand indistinguishable single-photons at high repetition rates, with high purity and probability of a single emission. The photon's indistinguishability is an important requirement for two-photon interference and thus the purity of implemented linear-optical quan-

tum gates. Purity expresses how close to ideal single quantum the produced light is. The probability of generation is a limiting factor for the success probability of the quantum gates, especially when using ancillary photons. It also determines how fast we can collect data in the experiments. Usually, multiple photons have to be generated simultaneously for the correct operation of the quantum logic circuit. Therefore, on-demand photon generation is desirable.

A *spontaneous parametric down-conversion* (SPDC) is a nonlinear optical effect in which vacuum fluctuations stimulate the decay of a pump photon into two photons, conserving the energy and momentum. This effect is utilized to produce single photons, including entangled photons. Both early [39, 67, 68] and contemporary experiments are using this method. It is possible to use one photon from the generated pair as a heralding photon to ensure that the generation succeeded. However, even when is the nonlinear medium pumped with pulsed laser [69], it does not generate single photons on demand. The number of photons is distributed with the Poissonian distribution. Usually, no photons are generated at most of the pulses, sometimes a single photon is generated and with even lower probability, multiple photons are generated. Increasing the pulse power increase the probability of single photon generation, but also increases the probability of multiple photon generation. More elaborate schemes are needed to at least approximate the on-demand SPDC source. For example, use of cavity for photon storage, SPDC repetition and photon-counting could approximate on-demand SPDC [70]. Alternatively, one can use the photon-blockade effect in a resonator to suppress multi-photon generation [71].

Another desired property of the single-photons is their indistinguishability. The indistinguishability in temporal and spatial modes could be controlled by using optical delay lines and waveguides. But the indistinguishability is also connected to a frequency bandwidth of the generated photons. One can increase the coherence length by spectral filtering of the generated photons [72], but this comes at the expense of the generation rate. The use of longer crystals or enclosing the crystals into resonators increases the coherence length of the generated photons [73, 74].

The generation probability can be boosted by multiplexing SPDC sources [75]. Entangled multi-photon states can be prepared by cascading SPDC sources with the help of a linear-optical network. This way, 6-photon [62, 76], 8-photon [77], 10-photon [78], and 12-photon entangled states were achieved [79]. Increasing the pump laser power increases generation rate, but at the same time increases chance of multiple photon generation, thus reducing the purity. Increasing the length of the nonlinear material can also increase the generation rate, but at the same time reduces the indistinguishably. Four-wave mixing (FWM), an effect emerging in materials with a third-order optical nonlinearity, is also investigated as a method for generating single photons [80, 81]. An important feature of any single-photon source technology is the possibility of on-chip integration, which has been demonstrated for SPDC [82].

Although SPDC and FWM sources are practical and reliable, solid-state single-photon sources, such as color centers [83–85], organic dye molecules [86–91] or quantum dots [92–99], are currently investigated and developed [100]. On these platforms, indistinguishable generation [84, 89, 96] and on-chip waveguide integration [85, 91, 101, 102] were demon-

strated. The Purcell effect is often used to improve the emission probability and photon indistinguishability. Solid-state sources typically require cryogenic conditions. The performance of solid-state devices is sensitive to perturbations such as electromagnetic field and thermal fluctuations, or mechanical strain of substrate material. These factors lead to spectral diffusion and emission instability. Current research aims to combat these adversary effects.

Linear-optical quantum information processing is also developing. While classical bulk optics offers comfort and flexibility for constructing experiments, the mechanical and interferometric stability, as well as the scalability, is limited. The on-chip integration of optical experiments overcomes these limitations. Optical integration offers stable interferometers with excellent mode-matching, thermal or electro-optical control of phase and the ability to concatenate many of them in complex interferometric structures [103, 104]. An interferometer with a tunable phase shift serves as a variable beam splitter, which is a building block for linear quantum optics. While integrated optics is an excellent platform for manipulating a single photon's path degree of freedom, the manipulation of polarization remains a challenge despite the recent advancements [105, 106]. To demonstrate feasibility of integrated quantum photonics, the pioneering quantum protocols are often implemented using a photonic chip [107–109].

Single-photon detection is a crucial step in a majority of optical experiments. The efficiency of detection is an important limiting factor in linear quantum optics. Initially, photo-multiplying tubes inherited from nuclear physics instrumentation were used, for example in Hong-Ou-Mandel experiment [39]. Later, single-photon avalanche diodes conquered the field, mainly due to available higher quantum efficiencies in near-infrared region, where typical SPDC sources operate. The development aims to improve quantum efficiency, reduce dark counts and dead time, increase response bandwidth and lower response time jitter. Also, on-chip integration was demonstrated [110]. Recently, a new technology of superconductive nano-wires appeared. These detectors offer greater quantum efficiency, lower dark counts and dead-time in exchange for cryogenic operation. Also, the on-chip integration of superconducting nano-wires was demonstrated [111].

Chapter 3

Methods and tools

3.1 Key concepts

This section introduces the main theoretical concepts that we utilize later in experiments. Its purpose is to introduce the reader to the terms, representations, and notations used in the thesis. We refer the reader to the classical textbooks, such as [B1], for careful and rigorous explanations of the introduced theoretical concepts. The only two exceptions are the discussion of two-photon interference and quantum tomography, adopted from [112]. Both topics are essential for our experiments.

3.1.1 Quantum bits

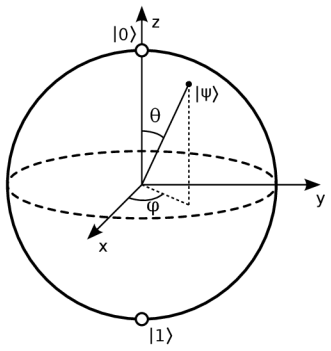

Figure 3.1: Bloch sphere. Computation basis states are on poles. Colatitude θ and longitude φ describe the state $|\psi\rangle$. Adopted from Wikipedia Commons by Smite-Meister/CC BY-SA (https://creativecommons.org/licenses/by-sa/3.0)

Quantum bit, or *qubit*, is a quantum analogy to a classical bit. In the Dirac notation, we introduce two *computational basis* states, $|1\rangle$ and $|0\rangle$. In analogy to classical computing, the first state represents the *on*-value of the qubit and the latter state represents the *off*-value of the qubit.

States $|0\rangle$ and $|1\rangle$ span a two-dimensional Hilbert space. A vector in this space describes the qubit. Arbitrary superposition

$$\alpha|0\rangle + \beta|1\rangle, \tag{3.1}$$

with $|\alpha|^2 + |\beta|^2 = 1$ is also a valid state. Complex numbers α, β represent probability amplitudes. This feature is important for parallelism in quantum computing [B1].

We often represent qubit as a point on the *Bloch sphere* with colatitude θ and longitude φ, as depicted in Fig. 3.1. The corresponding state is

$$|(\theta, \varphi)\rangle = \cos(\theta/2)|0\rangle + \sin(\theta/2)e^{i\varphi}|1\rangle. \tag{3.2}$$

A vector in 2^N-dimensional Hilbert space describes N qubits. Application of the Kronecker product $\otimes$ on single qubits $|a_i\rangle$ constructs the N-qubit product state

$$|a_{N-1} \ldots a_1 a_0\rangle = |a_{N-1}\rangle \otimes \cdots \otimes |a_1\rangle \otimes |a_0\rangle. \tag{3.3}$$

We use the following concise notation for N-qubit computational basis states.

$$|\mathrm{b}K\rangle = |i_{N-1}\rangle \otimes \ldots |i_1\rangle \otimes |i_0\rangle \tag{3.4}$$

$$K = \sum_{j=0}^{N-1} i_j 2^j, \tag{3.5}$$

where $i \in \{0; 1\}$ and $|i\rangle$ are the computational basis states. The binary representation $i_{N-1} \ldots i_1 i_0$ of the number K is the usual computational label of the state. Conveniently, computational basis state $|\mathrm{b}K\rangle$ contains value 1 at K-th row (counted starting with zero) and zeros otherwise. For example, $N = 2$,

$$|\mathrm{b}3\rangle = |11\rangle = \begin{pmatrix} 0 \\ 0 \\ 0 \\ 1 \end{pmatrix}.$$

There are many possible physical realizations of a qubit. In our experiments, we use *photonic qubits*, which we specifically discuss in section 3.2.2. A qubit can be generalized from 2-dimensional vectors to d-dimensional vectors. Then, we speak of *qudit*.

We use the density matrix formalism to describe the mixed states. To visualize the density matrix, we plot it as two-dimensional color maps. In Fig. 3.2, there is an example color plot for the density matrix

$$\rho = \frac{3}{10}\left(|00\rangle + i|11\rangle\right)\left(\langle 00| - i\langle 11|\right) + \frac{1}{10}\mathbb{1}_4,$$

where $\mathbb{1}_4$ is the 4×4 identity matrix. Its numerical value is written in traditional form in panel (a). The color plot in panels (b,c) represents real and imaginary parts of the density matrix with colored cells. Row and column indices of the cell are marked as ticks and define which matrix element the cell represents. The color of the cell with row-index i and column-index j represents the numerical value of matrix element $|\mathrm{b}i\rangle\langle\mathrm{b}j|$, in the concise notation. The color scale in the right section of panel (c) is the link between color and numerical value.

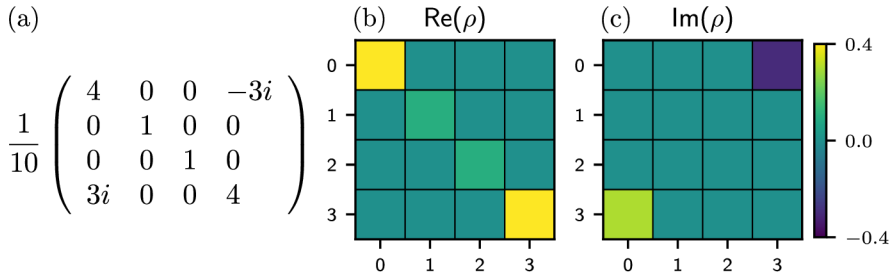

Figure 3.2: Example color plot of density matrix ρ. Density matrix ρ in the traditional matrix form (a). Real (b) and imaginary (c) parts of ρ. Both matrix plots share the same color scale.

3.1.2 Quantum gates, circuits, and channels

Quantum gates

A classical logic gate is a device that manipulates bits. It takes bit values from the input terminals, applies some logical operation on them and provides the result at the output terminal. Analogically, a quantum gate is a device that manipulates qubits. Unlike the classical gates, the quantum gates always have an equal number of input and output terminals, and their operation is reversible. A *unitary* matrix describes the action of a quantum gate.

Parameters Θ, Φ_1, and Φ_2 parameterize arbitrary single-qubit quantum gate

$$U_{1q}(\Theta, \Phi_1, \Phi_2) = \begin{pmatrix} \cos\Theta e^{i\Phi_1} & -\sin\Theta e^{-i\Phi_2} \\ \sin\Theta e^{i\Phi_2} & \cos\Theta e^{-i\Phi_1} \end{pmatrix} e^{i\delta}. \tag{3.6}$$

We can omit the global phase term $e^{i\delta}$ when it is not important. When we consider separable qubits that are not going to interact with each other, the global phase can be without doubt neglected. In the case of interacting qubits, the global phase can't be neglected, but it can be compensated for with additional phase shifts.

Gate	Symbol	Θ	Φ_1	Φ_2	δ	Operator
Identity	$\mathbb{1}$	0	0	0	0	$\|0\rangle\langle 0\| + \|1\rangle\langle 1\|$
NOT	σ_x	$\pi/2$	0	$\pi/2$	$-\pi/2$	$\|0\rangle\langle 1\| + \|1\rangle\langle 0\|$
Y-gate	σ_y	$\pi/2$	0	0	$\pi/2$	$-i\|0\rangle\langle 1\| + i\|1\rangle\langle 0\|$
Phase flip	σ_z	0	$\pi/2$	0	$-\pi/2$	$\|0\rangle\langle 0\| - \|1\rangle\langle 1\|$
Hadamard	H	$\pi/4$	$\pi/2$	$\pi/2$	$-\pi/2$	$\|+\rangle\langle 0\| + \|-\rangle\langle 1\|$
Phase shift	$V(\varphi)$	0	$-\varphi/2$	0	$\varphi/2$	$\|0\rangle\langle 0\| - e^{i\varphi}\|1\rangle\langle 1\|$

Table 3.1: Parameters for Eq. (3.6) to represent a quantum logic gate as a matrix. The following definition is used $|\pm\rangle = \frac{1}{\sqrt{2}}(|0\rangle \pm |1\rangle)$.

It is worth mentioning explicitly some fundamental single-qubit gates [B1]. The identity gate $\mathbb{1}$ does not introduce any change. It is an analogy to a classical buffer gate. Pauli

operators $\sigma_x = |0\rangle\langle 1| + |1\rangle\langle 0|$, $\sigma_y = i|1\rangle\langle 0| - i|0\rangle\langle 1|$, and $\sigma_z = |0\rangle\langle 0| - |1\rangle\langle 1|$ rotate the state about the given axis in Bloch sphere representation by π radians.

The operator σ_j generates φ-rotation $\exp(i\sigma_j\varphi/2)$ about axis j. σ_x operator is a quantum analogy to classical NOT gate. The Hadamard gate H turns a computational state into a balanced superposition of computational states and vice versa. Phase gate V introduces a phase shift φ between $|0\rangle$, $|1\rangle$ components. Table 3.1 provides parameters Θ, ϕ_1, ϕ_2, and δ for each gate. Together with Eq. (3.6), it provides explicit matrix-representation of each discussed gate. With these gates, it is possible to compose an arbitrary single-qubit gate [B1].

Bit readout is an important elementary operation in information processing. The elementary readout of a qubit is a projective measurement in the computational basis and it yields either value 0 or 1 and leaves the measured qubit in state $|0\rangle$ or $|1\rangle$, respectively. The readout is not limited to states $|0\rangle$ and $|1\rangle$. Single-qubit gates allow arbitrary-basis measurement. When the qubit is destroyed in the process, we speak of a *destructive* measurement.

In classical information processing, multiple-input gates, such as OR, AND, or XOR, are essential for computation. In quantum information processing, multi-qubit quantum gates are also crucial. These gates typically control the state of one qubit with the state of the other. This type of control can entangle qubits.

In this work, we mainly use controlled-NOT and controlled-Z two-qubit gates. The controlled-NOT gate performs σ_x operation on the target qubit if the control qubit is in state $|1\rangle$. The unitary matrix

$$U_{\mathrm{CNOT}} = |0\rangle\langle 0| \otimes \mathbb{1} + |1\rangle\langle 1| \otimes \sigma_x \tag{3.7}$$

describes the CNOT operation. Similarly, the controlled-Z gate introduces a π phase shift if and only if both qubits are in state $|1\rangle$. The corresponding unitary matrix is

$$U_{\mathrm{CZ}} = |0\rangle\langle 0| \otimes \mathbb{1} + |1\rangle\langle 1| \otimes \sigma_z. \tag{3.8}$$

These two gates are equivalent up to Hadamard operations on input and output of the target qubits. Generally, controlled-U gate is described with the matrix

$$U_{\mathrm{C}} = |0\rangle\langle 0| \otimes \mathbb{1} + |1\rangle\langle 1| \otimes U \tag{3.9}$$

and applies a unitary U on its target qubit when the control qubit is in state $|1\rangle$.

Another gate we use is the swap gate that interchanges the value of two qubits. The unitary matrix of swap gate is

$$U_{\mathrm{swap}} = |00\rangle\langle 00| + |01\rangle\langle 10| + |10\rangle\langle 01| + |11\rangle\langle 11|. \tag{3.10}$$

The swap gate, however, is not an entangling gate.

A network of universal single- and two-qubit quantum gates applied on multiple qubits can create a *multi-qubit quantum gate*. An important three-qubit gate is the Toffoli gate. The Toffoli gate is a three-qubit generalization of the CNOT gate and its operator description is

$$U_{\mathrm{CCNOT}} = \mathbb{1}_8 + |11\rangle\langle 11| \otimes (\sigma_x - \mathbb{1}_2), \tag{3.11}$$

where identity matrix indices denote its dimension. The Toffoli gate is important because together with Hadamard gate, phase gate, and CNOT gate forms a universal set of gates, capable of realizing arbitrary multi-qubit operation.

A quantum Fredkin gate, one of the goals of this thesis, is another important three-qubit quantum gate. It is a controlled version of the SWAP gate.

$$U_{\text{CSWAP}} = |0\rangle\langle 0| \otimes \mathbb{1}_4 + |1\rangle\langle 1| \otimes U_{\text{swap}}. \tag{3.12}$$

Unlike SWAP gate, the Fredkin gate entangling.

The goals of this thesis also contain the construction of a controlled-controlled-phase (CCP) gate with variable phase shift φ and a four-qubit version of CZ gate, a controlled^3-Z (C^3Z) gate. Their operator representation are

$$U_{\text{CCP}} = \mathbb{1}_8 + |11\rangle\langle 11| \otimes (V(\varphi) - \mathbb{1}_2), \tag{3.13}$$

$$U_{\text{C}^3\text{Z}}(\varphi) = \mathbb{1}_{16} - 2|1111\rangle\langle 1111|, \tag{3.14}$$

where $V(\varphi)$ is a single-qubit phase-shifting operation, see Tab. 3.1 and Eq. 3.6.

Quantum circuit diagram

A *quantum circuit diagram* schematically represents a sequence of gates and readouts. An example of a quantum diagram for a single qubit is depicted in Fig. 3.3 (a). Labeled boxes in the diagram represent individual gates and readouts. Their horizontal left-to-right ordering specifies their execution order. A horizontal line, representing a qubit, connects the neighboring elements. Multiple qubits are depicted as parallel horizontal lines, as shown in the example diagram in Fig. 3.3 (b). Vertical lines symbolize interaction between qubits. A list of used circuit diagram symbols is provided in Fig. 3.4.

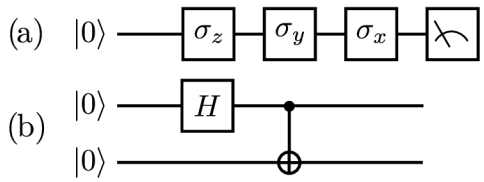

Figure 3.3: Examples of quantum circuit diagrams. (a) A qubit is initialized in state $|0\rangle$ and then σ_z, σ_y, and σ_x are applied in this order. Finally, the qubit is measured in the computational basis. (b) Two-qubit circuit which produces an entangled state.

Quantum process

The quantum gates are a special case of quantum processes. A *completely positive map* ϵ describes a quantum process that turns input density matrix ρ into output density matrix ρ':

$$\rho' = \epsilon(\rho). \tag{3.15}$$

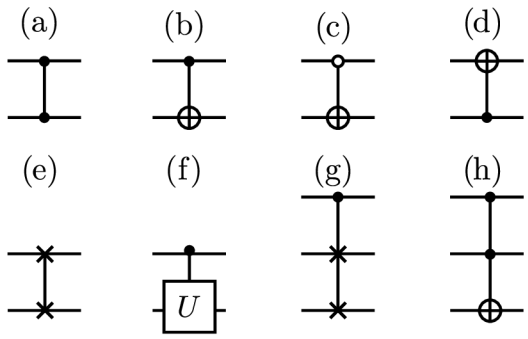

Figure 3.4: Used circuit diagram symbols. (a) CZ gate; (b) CNOT gate, black dot - control terminal, circled cross - target terminal; (c) open circle - control terminal activated by $|0\rangle$; (d) CNOT controlled with the second qubit; (e) swap gate; (f) controlled-unitary gate, (g) Fredkin gate, (h) Toffoli gate.

Unlike projective or unitary operators, the formalism of quantum processes can describe operations that are not completely under control or involve randomness. This capability is useful for the description of nonideal gates that we construct in a laboratory.

A set of Kraus operators $\{E_k\}$ describes a map ϵ, which transforms the input state ρ in the following way:

$$\epsilon(\rho) = \sum_k E_k \rho E_k^\dagger, \tag{3.16}$$

with $\sum_k E_k E_k^\dagger \leq \mathbb{1}$.

In this work, we use the alternative *channel-state duality* approach based on Choi-Jamiołkovski isomorphism[113, 114]. This approach is equivalent to Kraus operators [B1]. A density matrix χ of an entangled state represents a linear map.

For example, state

$$|\chi\rangle = (\mathbb{1} \otimes U)\left(|00\rangle + |11\rangle\right), \tag{3.17}$$

represents a single-qubit unitary operation U. Fig. 3.5 (a) represents the experimental interpretation. The described unitary operation U transforms the second part of the maximally entangled state. Note that we use a different normalization, where we omitted the factor $1/\sqrt{2}$ on purpose. This is due to the input-output relation, which we will discuss a bit later.

Measuring the first part of χ with POVM ρ^* causes the second part of χ to collapse into the output state $\rho' = U\rho U^\dagger$. Fig. 3.5 (b) depicts the situation schematically and shows the similarity with quantum teleportation.

Ket $|\chi\rangle$ can only describe operations that do not introduce statistical mixing of the states. Unitary operations and projectors onto a pure state are pure processes. A statistical mixture of various $|\chi_k\rangle$, $\chi = \sum_k p_k |\chi_k\rangle\langle\chi_k|$, with $\sum p_k = 1$, describes an impure process. Then, the density matrix χ represents the linear map that describes the process by mapping the input states onto output states.

The generalization to multiple qubits and impure processes follows. Suppose that a quantum process applies n-qubit operation U_k with some probability p_k. With a 2-n qubit

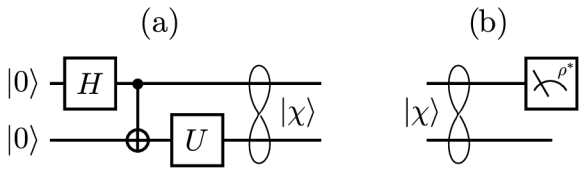

Figure 3.5: Experimental interpretation of Choi's formalism. a) Preparation of $|\chi\rangle$. The CNOT gate turns input qubits into the maximally entangled state. b) Output generation. The first subsystem of $|\chi\rangle$ is projected to ρ^*, the phase-conjugated input state.

maximally entangled state

$$|\Psi_{2n}^{+}\rangle = \sum_{i=0}^{2^n-1} |\mathrm{b}i\rangle \otimes |\mathrm{b}i\rangle, \tag{3.18}$$

written in the concise notation (3.5), we define the Choi matrix

$$\chi = \sum_k p_k \left(\mathbb{1}_{2^n} \otimes U_k\right) |\Psi_{2n}^{+}\rangle\langle\Psi_{2n}^{+}| \left(\mathbb{1}_{2^n} \otimes U_k\right)^{\dagger}, \tag{3.19}$$

which characterizes the operation.

The input-output relation for density matrices is

$$\rho' = \mathrm{Tr}_1[(\rho^* \otimes \mathbb{1})\,\chi] \tag{3.20}$$

where Tr_1 is a partial trace over the first subsystem. The relation formally describes projecting the first subsystem of χ to ρ^*. In the case of deterministic operations, we require $\mathrm{Tr}\rho' = 1$ and this is the reason for the choice of normalization of n-qubit deterministic processes to $\mathrm{Tr}\chi = 2^n$. In various calculations, like comparing two processes by means of their fidelity, we often normalize the process matrix to $\mathrm{Tr}\chi = 1$ for convenience.

A map can decrease the trace,

$$1 \geq \mathrm{Tr}(\rho) > \mathrm{Tr}\left[\epsilon(\rho)\right] \geq 0.$$

A trace-decreasing map describes a probabilistic quantum process, with the trace value being the success probability. In the case of trace-decreasing processes, we usually trace-normalize the output density matrix ρ' again to ensure normalization $\mathrm{Tr}\left[\epsilon(\rho)\right] = 1$, which is often assumed in various other calculations.

With the Choi-Jamiołkovski approach, we can work with quantum processes the same way as with quantum states. This ability is useful, for example, when comparing two processes or when we need to quantify the purity of a process.

3.1.3 Two-photon interference

Two- and multi-qubit gates require interaction between the qubits. An underlying principle of how linear quantum optics achieve this interaction is a *two-photon interference* [39].

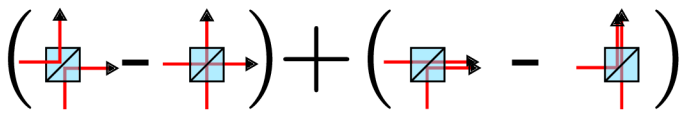

Figure 3.6: Two-photon interference on a beam splitter. There are four possibilities of photon propagation. The possibilities depicted in the left parenthesis destructively interfere in the case of indistinguishable photons on a balanced beam splitter.

In this section, we describe this effect. We will apply it later in Section 3.2.3 to explain the working principle of a two-qubit logic gate into detail.

Consider two indistinguishable photons, each entering one input port of a beam splitter with transmittance $T = tt^*$. The expression

$$|\psi_\mathrm{i}\rangle = a_\mathrm{i}^\dagger b_\mathrm{i}^\dagger |\mathrm{vac}\rangle \tag{3.21}$$

describes the quantum state of the photons in front of the beam splitter in Fock basis, where $a_\mathrm{i}^\dagger$ and $b_\mathrm{i}^\dagger$ are the creation operators for each beam splitter's input mode and $|\mathrm{vac}\rangle$ is the vacuum state. The beam splitter mixes the optical modes in the following way

$$a_\mathrm{i}^\dagger \rightarrow a_\mathrm{o}^\dagger t - b_\mathrm{o}^\dagger r^*, \tag{3.22}$$

$$b_\mathrm{i}^\dagger \rightarrow b_\mathrm{o}^\dagger t^* + a_\mathrm{o}^\dagger r, \tag{3.23}$$

where t and r are complex numbers and satisfy condition $|t|^2 + |r|^2 = 1$. Following the Heisenberg approach, we write the state at the beam splitter output as the transformed operators applied on the vacuum state

$$|\psi_\mathrm{o}\rangle = \left[\left(a_\mathrm{o}^\dagger a_\mathrm{o}^\dagger rt - b_\mathrm{o}^\dagger b_\mathrm{o}^\dagger (rt)^*\right) + \left(|t|^2 - |r|^2\right) a_\mathrm{o}^\dagger b_\mathrm{o}^\dagger\right] |\mathrm{vac}\rangle. \tag{3.24}$$

The four terms represent four possible scenarios, depicted in Fig. 3.6, of how photons are reflected or transmitted. Terms containing $a_\mathrm{o}^\dagger a_\mathrm{o}^\dagger$ or $b_\mathrm{o}^\dagger b_\mathrm{o}^\dagger$ represent the scenarios in which both photons leave together through a single output port. The term containing $a_\mathrm{o}^\dagger b_\mathrm{o}^\dagger$ represents the scenario in which each photon leaves the beam splitter separately via its own output port. Remarkably, the scenarios interfere. Factor $\left(|t|^2 - |r|^2\right) a_\mathrm{o}^\dagger b_\mathrm{o}^\dagger$ is the probability amplitude for both photons leaving the beam splitter separately and it can vanish when the beam splitter is balanced ($|t|^2 = |r|^2$). In the case of $|t|^2 < |r|^2$, the factor $|t|^2 - |r|^2$ is negative and we interpret it as a π-phase shift. This phase shift is essential for our implementation of two-qubit quantum gates, which we discuss in detail in Section 3.2.3.

To observe the destructive two-photon interference experimentally, we realize *coincidence basis measurements*. We place a single-photon detector into each output port of the beam splitter and connect their signal to a classical AND logic gate. The event counter is connected to the output of the AND gate and registers the simultaneous detection events. Only the term $\left(|t|^2 - |r|^2\right) a_\mathrm{o}^\dagger b_\mathrm{o}^\dagger$ is relevant in the coincidence basis measurement.

Let us now consider two distinguishable photons entering the beam splitter. Formally, we introduce a new degree of freedom to the modes a, b and label it with a subscript.

The new degree of freedom makes photons distinguishable. It can be for example time of arrival, early (E) or late (L). The output state takes the form

$$|\psi_o\rangle = \left[\left(a^\dagger_{E,o}a^\dagger_{L,o}rt - b^\dagger_{E,o}b^\dagger_{L,o}(rt)^*\right) + \left(|t|^2a^\dagger_{E,o}b^\dagger_{L,o} - |r|^2a^\dagger_{L,o}b^\dagger_{E,o}\right)\right]|\text{vac}\rangle. \tag{3.25}$$

The rightmost term in Eq. 3.25 does not vanish, and consequently, the probability of a coincidence event is 1/2. A statistical mixture of distinguishable and indistinguishable photons describes partially distinguishable photons. We can control the degree of indistinguishability temporally by delaying one photon from the pair. To see the typical Hong-Ou-Mandel (HOM) dip [39], we plot the coincidence rate as a function of temporal delay. Fig. 3.7 shows an example of a HOM dip measured in our experiments.

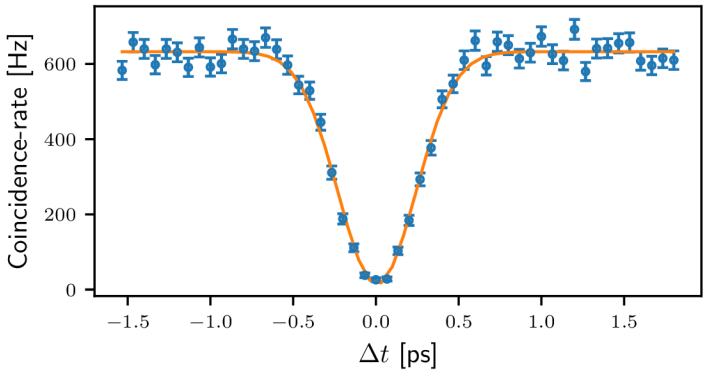

Figure 3.7: A typical Hong-Ou-Mandel dip, recorded in our experiments. The coincidence rate is plotted against the relative temporal delay Δt of two photons. Error bars represent one standard deviation and the orange curve is Gaussian fit to data.

The dip shape is related via Fourier transform to the frequency spectrum of used photons. Therefore the temporal width of the dip is inversely proportional to the spectral width. The HOM visibility V quantifies the indistinguishability of the photons. It is expressed with minimal and maximal coincidence rates $C_{12,\text{min}}$, and $C_{12,\text{max}}$

$$V = \frac{C_{12,\text{max}} - C_{12,\text{min}}}{C_{12,\text{max}}}. \tag{3.26}$$

3.1.4 Quantum state tomography

The *quantum state tomography* is a useful tool for obtaining information about a quantum state ρ from a certain set of measurements. Usually, there is an ensemble of quantum systems, all prepared in a state ρ, which we split into groups and perform measurements in various basis on them. We call the resulting set of outcomes a *tomogram*. The tomogram contains information about the state and the *quantum state reconstruction* turns the tomograms into a density matrix of a measured quantum state [112, 115].

Let us start with an example of single-qubit tomography. Suppose we have a source that produces photons in state ρ. We sequentially perform the projections in states $|0\rangle$, $|1\rangle$, $|\pm\rangle = \frac{1}{\sqrt{2}}(|0\rangle \pm |1\rangle)$, $|\circlearrowright\rangle = \frac{1}{\sqrt{2}}(|0\rangle + i|1\rangle)$, and $|\circlearrowleft\rangle = \frac{1}{\sqrt{2}}(|0\rangle - i|1\rangle)$. These states are eigenstates of Pauli operators. For the later use, we denote the set of these states as

$$\mathbf{S} = \{|0\rangle; |1\rangle; |+\rangle; |-\rangle; |\circlearrowright\rangle; |\circlearrowleft\rangle\}. \tag{3.27}$$

The tomogram T consists of six elements

$$\mathbf{T} = \{T_i\}_{i=0,\cdots,5} = \{\langle 0|\rho|0\rangle; \langle 1|\rho|1\rangle; \langle +|\rho|+\rangle; \langle -|\rho|-\rangle; \langle \circlearrowright|\rho|\circlearrowright\rangle; \langle \circlearrowleft|\rho|\circlearrowleft\rangle\}.$$

Theoretically, the elements are projection probabilities, but in practice, we obtain relative frequencies T_i. The relative frequencies suffer from noise, which is dependent on state ρ. In the presence of noise, we may not always find ρ with all projection probabilities simultaneously matching their measured estimates T_i. The better signal-to-noise ratio in tomogram we have, the more precise reconstruction we can get. Practically, a large number of state copies is desired.

Choice of measurements is important. Consider a single qubit. We need to measure at least four different projections, otherwise we speak of *incomplete* data. When reconstructing an incomplete tomogram, multiple density matrices can match the measured data equally well. The specific choice of measurement state matters [116–118]. Also, the number of projection states matters. According to [118], the precision of tomography increases with the number of projections.

In this work, we mainly use Pauli tomography. We project the examined qubit onto states from set **S**. This is an over-complete measurement, but in comparison to the minimal four-state scheme, it provides better precision [116]. Because we use the **S**-states to probe various processes, the tomogram obtained by Pauli-tomography has a clear and intuitive interpretation.

The size of a tomogram scales *exponentially* with the number of qubits n. If the measurement scheme requires m projections for a single qubit, then the n-qubit state would require m^n projections. The projection set consists of all combinations $\pi_{i_0} \otimes \cdots \otimes \pi_{i_{n-1}}$ of single-qubit projectors. As a result, the standard quantum state tomography is a great tool for low-dimensional system analysis but gets impractical for larger systems.

Linear inversion

A way to reconstruct the quantum state from a tomogram is to parameterize its density matrix, construct a system of equations describing the measurement using these parameters and invert it to find the parameters.

Expansion into a sum of operators:

$$\rho = \sum_i M_i m_i, \tag{3.28}$$

where M_i is the expansion operator and parameter m_i its weight, parameterizes a density matrix. For example, an identity operator and the three Pauli operators compose an arbi-

trary single-qubit density matrix. For a n-qubit state, the number of free parameters m is $2^{2n} - 1$.

The j-th entry in the tomogram is proportional to the probability of projection on the projection state $|\pi_j\rangle$:

$$\langle\pi_j|\rho|\pi_j\rangle = \sum_i \langle\pi_j|M_i|\pi_j\rangle m_i = T_j. \tag{3.29}$$

Let us define a matrix $\mathcal{M}$ with matrix elements

$$\mathcal{M}_{ji} = \langle\pi_j|M_i|\pi_j\rangle. \tag{3.30}$$

Then equations (3.29) are equivalent to the matrix equation

$$\mathcal{M} \cdot \vec{m} = \vec{T}, \tag{3.31}$$

where $\vec{m}$ is a vector of parameters m_i, $\vec{T}$ is a vector with tomogram values and symbol $\cdot$ stands for an inner product. In the linear inversion method, we attempt to solve the system of equations 3.31 to obtain parameters m, formally:

$$\vec{m} = \mathcal{M}^{-1} \cdot \vec{T}. \tag{3.32}$$

One problem is the inversion because $\mathcal{M}$ may not be invertible. We need to use pseudo-inverse methods instead. Another problem comes in the presence of noise in a tomogram. Then, the properties of the reconstructed matrix might not meet the requirements for a proper density matrix. Namely, we can not guarantee the positivity of the reconstruction. Negative eigenvalues of the reconstructed density matrix would implicate negative measurement probabilities. Such a result is *unphysical*.

We mostly do not use this method. There is an exception, however. When we are interested in a linear functional $f(\rho)$, the other reconstruction methods, like least-square fitting or maximum likelihood, provide biased estimates. The bias is quite small and scales down with increasing signal-to-noise ratio, but in the case of precise measurement it can be an obstacle. The linear inversion gives unbiased estimates of $f(\rho)$. In the case of a nonlinear functional, the unphysical reconstructions are problematic. One can avoid this problem by estimating the state ρ, linearizing the functional at this point, and then using linear-inversion reconstruction to estimate the nonlinear functional [119]. Alternatively, one can estimate the direction of bias using theory and numerical simulation and take it into account when evaluating the nonlinear functional.

Maximum likelihood reconstruction

Maximum likelihood (ML) reconstruction is a method that finds the physical density matrix ρ that is most consistent with the measured tomogram $\vec{T}$, expressed in terms of relative frequencies T_i. The consistency is quantified with the likelihood function

$$\mathcal{L} = \prod_i \mathrm{Tr}[\rho\pi_i]^{T_i N}, \tag{3.33}$$

where N is the total number of measured copies of an investigated system, $\pi_i = |\pi_i\rangle\langle\pi_i|$ is the projector operator. The likelihood is proportional to the probability of obtaining the measured tomogram with an assumption density matrix ρ.

From the likelihood definition and *Jensen inequality*, one can derive the following extremal equation in Hermitian form

$$K\rho K = \rho, \tag{3.34}$$

which sets the condition on ρ which maximizes the likelihood [112]. The Hermitian operator

$$K = \sum_i \frac{T_i \pi_i}{\mathrm{Tr}\,(\rho\pi_i)} \tag{3.35}$$

is a convex sum of projective operators. The extremal ρ is found using the expectation-maximization algorithm [112]. It is an iterative algorithm that starts with an initial guess $\rho_0 = \mathbb{1}_d$. Recurrent equation

$$\rho_{n+1} = \frac{K_n \rho_n K_n}{\mathrm{Tr}\,(K_n \rho_n K_n)} \tag{3.36}$$

describes the iterative process. The iteration is stopped when the change in the iteration step is small enough,

$$||\rho_{n+1} - \rho_n|| < \epsilon, \tag{3.37}$$

with $||\cdot||$ representing the Frobenius measure, or when the iteration limit is exceeded. The resulting reconstructed density matrix fully describes the measured quantum state.

Maximum likelihood reconstruction in Python

Python is a high-level computer scripting language that currently gains popularity in many fields, including science and engineering. One of the reasons is development speed. However, it is an interpreted language, and in comparison to compiled languages, like C++, the performance in some tasks is limited. Specifically, loops are slow. Listing 3.1 shows the part of the reconstruction code. It implements Eq. 3.35 and Eq. 3.36 straightforwardly.

Listing 3.1: Straightforward implementation of ML reconstruction. At sign (@) represents matrix multiplication.

```
while iters<max_iters and distance < epsilon:
    RhoPrev = Rho
    K = np.zeros((d,d), dtype=complex)
    for Ti, Pi in zip(Tomogram, Projectors):
        K = K + (Ti * Pi)/np.trace(Rho @ Pi)
    Rho = K @ Rho @ K
    Rho = Rho/np.trace(Rho)
    distance = abs(np.linalg.norm(Rho - RhoPrev))
```

With a set `Projectors` containing measurement operators `Pi` and corresponding tomogram `Ti` elements, the code constructs K operators and performs the iteration to reconstruct the density matrix. Binary operator `@` represents the inner product.

The code would not run efficiently in plain Python due to its two nested loops, even when *Numpy* governs the matrix multiplications. Numpy is a library for Python that performs computational tasks with numerical arrays with a performance that is comparable to compiled programs. Rewriting an algorithm from explicit loops to algebraic operations on numerical arrays can significantly speed up the computations. This approach is known as *vectorization*.

For example, we compute a scalar product by looping over elements of two arrays while incrementing the result variable with the product of two elements in each step. On a standard personal computer, the explicit Python code would run almost 30 times slower than calling a dedicated compiled routine in Numpy. Although there are ways to compile parts of the Python code, vectorization is a useful optimization technique.

Line 5 of code 3.1 is the first thing to optimize. The numerator `(Ti * Pi)` does not change in the iteration process. Time-consuming Kronecker and outer products construct the measurement operator π_i from the constituent single-qubit kets that describe the measurement. It is unnecessary to calculate the projector again in every step. When there is enough memory, the script should compute it only once, store the results, and later refer to them.

The denominator `np.trace(Rho @ Pi)` on line 5 changes in each iteration. This computation is not economical because it performs full matrix multiplication but sums only diagonal elements. For a $d \times d$ density matrix, it does d^3 multiplications but keeps only results of d^2 multiplications. For two $d \times d$ matrices A and B with elements A_{ij} and B_{ij}, respectively, the following identity holds

$$\mathrm{Tr}\,(AB) = \sum_{i=0}^{d-1}\sum_{j=0}^{d-1} A_{ji}B_{ij}. \tag{3.38}$$

This identity shows that only d^2 multiplications are needed. Let $\vec{A}$ and $\vec{B}$ be vectors that contain serialized elements of matrices A and B. Then $\mathrm{Tr}\,(AB) = \vec{A}^{\mathrm{T}} \cdot \vec{B}$. Numpy can efficiently calculate such inner products.

In noncompiled Python, the inner loop in lines 4 and 5 is another bottleneck. The loop constructs K operator in every iteration. One can avoid an explicit loop with a proper serialization of projector operators π_i and matrix multiplication. Assume d-dimensional Hilbert space. Let tomogram have m elements T_i. Let a j-th column of the $d^2 \times m$ matrix $\mathbb{m}$ with elements $\mathbb{m}_{ij}$ contain $d^2 \times 1$ serialized operator π_j. Let $\vec{\rho}^{\mathrm{T}}$ be $1 \times d^2$ vector containing serialized transposed density matrix ρ^T. The denominator in the i-th sum element of Eq. 3.35 is

$$D_i = \left(\vec{\rho}\mathbb{m}\right)_i. \tag{3.39}$$

We show the calculation of the denominator terms on the example of Pauli-tomography and density matrix $\rho_{\circlearrowleft} = |\circlearrowleft\rangle\langle\circlearrowleft|$

$$D = \vec{\rho}^{\mathrm{T}}{}_{\circlearrowleft} \cdot \mathbb{m} = \begin{pmatrix} \frac{1}{2} & \frac{i}{2} & -\frac{i}{2} & \frac{1}{2} \end{pmatrix} \cdot \begin{pmatrix} 1 & 0 & 1/2 & 1/2 & 1/2 & 1/2 \\ 0 & 0 & 1/2 & -1/2 & -i/2 & i/2 \\ 0 & 0 & 1/2 & -1/2 & i/2 & -i/2 \\ 0 & 1 & 1/2 & 1/2 & 1/2 & 1/2 \end{pmatrix}$$

$$D = \begin{pmatrix} 1/2 & 1/2 & 1/2 & 1/2 & 1 & 0 \end{pmatrix}.$$

Matrix multiplication efficiently computes the vector D with elements D_i. With D, T, and π, Numpy calculates the K operator without an explicit loop in the Python code with a vectorized assignment

$$K = \sum_i^m \pi_i \frac{T_i}{D_i}. \tag{3.40}$$

The performance improvement comes at the expense of computer memory, in which we store intermediate results. Tab. 3.2 provides the memory requirements for storing the intermediate results in 16-byte complex floating-point numbers. In cases with less than seven qubits, it is not a problem for contemporary personal computers. With the increasing number of qubits, memory consumption quickly becomes an issue, and we have to resign on storing π operators in memory. Our implementation uses the discussed optimizations and is freely available on Git Hub [120].

n	memory consumption	
1	384	B
2	9.2	kB
4	5.0	MB
6	2.8	GB
7	68	GB
8	1640	GB
n	$(4m)^n \cdot 16$	B

Table 3.2: Memory consumption for n-qubit vectorized ML reconstruction. Six states per qubit are used ($m = 6$).

Quantum process tomography

In this thesis, we experimentally implement various quantum gates. To fully characterize the realized quantum operation, we use the *quantum process tomography*, a generalization of quantum state tomography.

The characterized quantum process M is sequentially probed with known states ρ_i. Each corresponding output state is then tomographically analyzed. The copies of the output states are sequentially projected to state $|\pi_j\rangle$, and tomogram elements T_{ij} are recorded. This process is depicted schematically in Fig. 3.8.

Here we utilize the channel-state duality to describe the quantum process. In such formalism, the process is described the same way as a state and consequently we can apply quantum state to reconstruct processes as well. Eq. 3.20 describes how a process χ transforms an input state ρ_i. The output state is further projected onto $|\pi_j\rangle$ with the probability

$$p_{ij} = \mathrm{Tr}_2\left(\mathrm{Tr}_1[\left(\rho_i^* \otimes \mathbb{1}\right)\chi]\pi_j\right) = \mathrm{Tr}[\left(\rho_i^* \otimes \pi_j\right)\chi]. \tag{3.41}$$

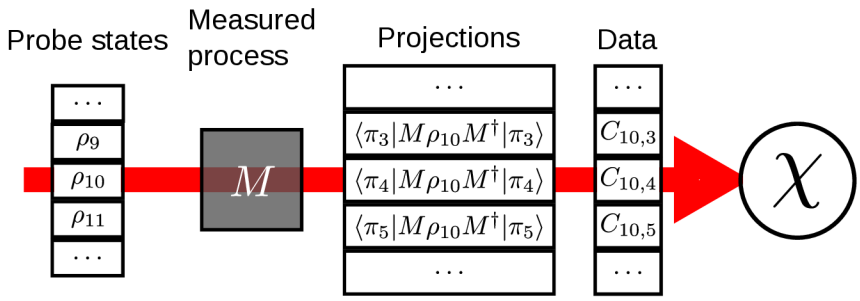

Figure 3.8: Quantum process tomography. Measured pure process M is probed with known states ρ_i. The corresponding output states are tomographically characterized to obtain the process tomogram. The tomogram is then reconstructed into process matrix χ.

In the equation, the term $\left(\rho_i^* \otimes \pi_j\right)$ defines the measurement operator. Using Eq. 3.41 and Eq. 3.35 we get

$$K_p = \sum_{ij} \frac{T_{ij}\left(\rho_i^* \otimes \pi_j\right)}{\mathrm{Tr}[\left(\rho_i^* \otimes \pi_j\right)\chi]}. \tag{3.42}$$

Iteration (3.37) is then used, just with operator K_p (3.42) instead of K (3.35), to reconstruct the process matrix χ. As a result, the same numerical procedure can reconstruct both quantum process and quantum state, just with different definitions of measurement operators.

For n qubits, m probe states per qubit, and k projection states per qubit, the size of the tomogram is $m^n k^n$. For example, for Pauli-tomography with Pauli-probe states the tomogram size scales as 6^{2n}. We would need nearly $1.7 \cdot 10^6$ measurements to scale the tomography to four-qubit process. With additional assumptions, like high purity of the reconstructed state or process, it is possible to reduce the required number of measurements using the compressed sensing techniques [17, 18]. The full characterization of a process is not always necessary, and sometimes estimating bounds on quantities of interest [22] is sufficient. In Section 4, we will use such an approach.

3.1.5 Commonly used measures

Before we proceed to the experimental implementation, we introduce the quantities of interest that we frequently use in our experiments.

Purity characterizes the amount of noise in a quantum state. It is defined as

$$P(\rho) = \mathrm{Tr}\left(\rho^2\right) = \sum_i \lambda_i^2, \tag{3.43}$$

where λ_i are the eigenvalues of ρ. The purity of a pure state is 1, while the purity of the n-qubit maximally mixed state is 2^{-n}. Purity of partially mixed states is bounded by these values.

Fidelity measures the similarity of states of the same dimension ρ_1 and ρ_2 and is defined as

$$F = \left(\mathrm{Tr}\left[\sqrt{\sqrt{\rho_1}\rho_2\sqrt{\rho_1}}\right]\right)^2. \tag{3.44}$$

If at least ρ_i is pure, then $\sqrt{\rho_i} = \rho_i$ and Eq. 3.44 simplifies to

$$F = \mathrm{Tr}[\rho_1\rho_2]. \tag{3.45}$$

Eq. (3.45) represents the probability of projecting ρ_1 to state ρ_2 and provides the intuitive meaning of fidelity. Usually, the density matrices are trace-normalized, $\mathrm{Tr}\rho = 1$. In other cases, we normalize them for the fidelity computation. If two states are identical, their respective fidelity is 1. For two orthogonal states, the fidelity is 0. The fidelity of any pure n-qubit state with a maximally mixed n-qubit state is 2^{-n}.

Practical computation of fidelity using Eq. (3.44) requires matrix square root computation. Some mathematical libraries have dedicated function for computing the square root of a matrix, but some of these methods fail for singular matrices. Unfortunately, density matrices of pure states are singular. Another way to compute the matrix square root is the spectral theorem

$$f(\rho) = Uf(\Lambda)U^{-1}, \tag{3.46}$$

which decomposes ρ into matrices U, U^{-1}, and a diagonal matrix Λ. Matrix Λ contains eigenvalues λ_i on its diagonal and function f turns it into a matrix with $f(\lambda_i)$ on its diagonal. Matrix U consists of horizontally concatenated eigenstates of ρ expressed as column vectors. U is unitary because ρ is Hermitian and as a consequence, the matrix inverse can be replaced with Hermite conjugation. In the case of fidelity computation, $f(x) = \sqrt{x}$.

It is important to use a proper method for finding the eigensystem of a Hermitian matrix. Otherwise, when some eigenvalues are zero, the numerical routine might not find orthogonal eigenvectors. The reason is that we have eigenstates $|u_i\rangle$ with vanishing eigenvalues $\rho|u_i\rangle = 0$. Then any linear combination of such eigenvectors is also an eigenvector

$$\rho\left(\sum_i a_i|u_i\rangle\right) = \sum a_i\rho|u_i\rangle = 0.$$

and might be numerically found instead. Then, the row vectors forming U are nonorthogonal, and consequently, U is not unitary, identity $U^\dagger U = UU^\dagger = \mathbb{1}$ does not hold and the computation might provide wrong results.

Let us illustrate this problem with an example of state $\rho = (|+\rangle\langle+|)^{\otimes 2}$. Numerical routine in Python's Numpy `linalg.eig` found eigenvalues 0,1,0, and 0 corresponding to

$$U = \begin{pmatrix} 0.866 & -0.5 & -0.866 & 0.646 \\ -0.289 & -0.5 & 0.289 & -0.328 \\ -0.289 & -0.5 & 0.289 & -0.487 \\ -0.289 & -0.5 & 0.289 & -0.487 \end{pmatrix}.$$

The eigenvectors are not orthogonal and $U^\dagger U$ has nonzero off-diagonal elements. The problem remains even for mixed states. If $|u_i\rangle$ is the eigenvector of a pure part, it is also an

eigenvector of any mixture with a maximally mixed state and linear combination $\sum_i a_i|u_i\rangle$ is also an eigenvector. Function `linalg.eigh` should be used instead. If the used programming language does not have dedicated reliable function for finding an eigensystem of a Hermitian matrix, one has to ensure that all eigenstates are orthogonal. The Gram–Schmidt process [B2] is suitable for orthogonalizing the eigenvectors.

Von Neumann entropy

$$S(\rho) = -\mathrm{Tr}\left(\rho \log_2(\rho)\right) \tag{3.47}$$

expresses the information disorder of a state. When ρ is diagonalized with eigenvalues λ_i, then

$$S(\rho) = -\sum_i \left(\lambda_i \log_2(\lambda_i)\right) \tag{3.48}$$

is formally identical to the classical Shannon entropy. The classical Shannon entropy gives a number of bits required to store information from the channel [B1]. If, for example, a classical binary communication channel always outputs zeroes, we do not need any memory to store that information. We know that every transmitted message is zero. On the other hand, if the channel outputs values zero and one with equal probability, we need at least one bit to store the message. Generally, classical Shannon entropy gives the average minimum number of bits required to store a message from a channel that emits them with some known probability distribution. A fully ordered system has $S = 0$ bits. A channel that emits 2^n different messages with uniform probability has maximal entropy, n bits. Similarly, in the case of the quantum Von Neumann entropy, a pure state has $S = 0$ and the maximally mixed n-qubit state has $S = n$ bits. We use the Von Neumann entropy to calculate *mutual quantum information*.

The mutual quantum information quantifies the correlation strength between two parts, ρ_A and ρ_B of a composite quantum state ρ_{AB}. It is computed from entropies

$$I(\rho_{AB}) = S(\rho_A) + S(\rho_B) - S(\rho_{AB}), \tag{3.49}$$

where partial traces are taken over subsystems. I of uncorrelated states is 0. On the other hand, I of entangled symmetric bipartite $2n$-qubit states is $2n$.

In quantum information, entanglement is a valuable resource. An entanglement criterion is a tool to indicate whether a state is entangled. Entanglement measures are used to quantify the entanglement.

The partial-transpose criterion [121] tests whether a bipartite quantum state is inseparable. If a state after partial transpose has a negative eigenvalue,

$$\min(\mathrm{eig}\,\rho^{T_1}) < 0, \tag{3.50}$$

where ρ^{T_1} is the partial transpose of ρ, then ρ is not separable. The criterion is insensitive to the choice of the transposed part. We use this criterion on two-qubit states. Following index relabeling of matrix elements transposes the first part of a two-qubit density matrix

$$\rho^{T_1}_{(2i_1+i_0,2j_1+j_0)} = \rho_{(2j_1+i_0,2i_1+j_0)} \;:\; i_0,\, i_1,\, j_0,\, j_1 \in \{0;1\}, \tag{3.51}$$

where $2i_1 + i_0$ and $2j_1 + j_0$ are row and column indices of a matrix element expressed as binary number.

Concurrence [122] is a quantity that is related to entanglement. Concurrence of a two-qubit density matrix ρ is

$$C(\rho) = \max\{0, \lambda_1 - \lambda_2 - \lambda_3 - \lambda_4\} \tag{3.52}$$

where eigenvalues λ_i are sorted by their size in decreasing order

$$\lambda_i = \mathrm{eig}_i \sqrt{\sqrt{\rho}\tilde{\rho}\sqrt{\rho}} \tag{3.53}$$

and $\tilde{\rho}$ is a spin-flipped density matrix

$$\tilde{\rho} = (\sigma_y \otimes \sigma_y)\, \rho^* \,(\sigma_y \otimes \sigma_y)\,. \tag{3.54}$$

For practical computations, it is convenient to use the alternative formulation [122]

$$\lambda_i = \sqrt{\mathrm{eig}_i(\rho\tilde{\rho})}. \tag{3.55}$$

With the alternative formulation, a single eigenvalues search suffices to calculate C.

The *entanglement of formation* of a state ρ quantifies resources needed to prepare state ρ in terms of maximally entangled Bell states. In other words, its inverse is the number of state's ρ copies needed to distill a single two-qubit maximally entangled state. In the case of a two-qubit state, the concurrence is related to the entanglement of formation with an auxiliary function

$$h = -x \log_2 -(1-x)\log_2(1-x). \tag{3.56}$$

Then, the entanglement of formation is

$$E_f = h\left(\frac{1+\sqrt{1-C^2}}{2}\right). \tag{3.57}$$

So far, we have discussed entanglement in bipartite systems. Entanglement in multipartite systems is a rich and fascinating subject of both theoretical and experimental quantum information science. The generalizations of the presented criterion and measures to multipartite systems as well as a review of other criteria and measures are beyond the scope of this thesis. Instead, we briefly introduce *entanglement witnessing* [123, 124], a method for detecting entanglement.

The entanglement witness method detects a certain type of entanglement. The task is to find a measurement operator W for some entangled state ρ' such that

$$\mathrm{Tr}(\rho_s W) \geq 0 \tag{3.58}$$

for all separable states ρ_s and

$$\mathrm{Tr}(\rho' W) < 0 \tag{3.59}$$

for the desired entangled state ρ'. The Hilbert space is split by a hyper-plane into two sub-spaces according to the sign of witness value $\mathrm{Tr}(\rho W)$, as depicted in Fig. 3.9. One subspace contains all separable states, while the other contains at least the state ρ'. Negative witness value certifies that the measured state was entangled. On the other hand, nonnegative witness values do not necessarily indicate a separable state. This is illustrated in the figure as point ρ'' which would have a positive witness value, but lies outside the set of separable states. We seek W such that it can be realized with few local measurements so it can be conveniently measured in the laboratory. Another goal for witness design is tolerance to noise.

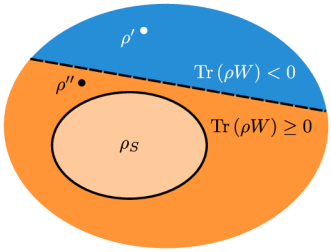

Figure 3.9: Witness operator W separates the Hilbert space, illustrated as a colored ellipse, into two sub-spaces according to the sign of the witness value. The subspace of states that have non-negative witness values is depicted in orange color, while the other subspace is depicted in blue. Nonnegative subspace contains all separable states, indicated with light orange color. Nonnegative witness values can't certify separability because the orange set contains not only separable states, but also entangled states. The border $\mathrm{Tr}(\rho W) = 0$ does not touch the border of separable states subspace and therefore we say that the witness is not optimal.

The typical example is the detection of the Greenberger–Horne–Zeilinger (GHZ) state $|\mathrm{GHZ}\rangle = \frac{1}{\sqrt{2}}(|000\rangle + |111\rangle)$. Then, the witness is

$$W_{\mathrm{GHZ}} = \mathbb{1}/2 - |\mathrm{GHZ}\rangle\langle\mathrm{GHZ}|.$$

For any separable pure state, the expectation value would be zero. With pure state $|\mathrm{GHZ}\rangle$, the expectation value would be -1/2. And with an orthogonal entangled state $|\mathrm{GHZ}^{\perp}\rangle = \frac{1}{\sqrt{2}}(|001\rangle + |110\rangle)$ the witness value would be 1/2 and the state would not be detected as entangled.

3.1.6 Bootstrapping

In the experiment, it is crucial to know the measurement errors. Unfortunately, it is not feasible to analytically describe the propagation of statistical errors in the maximum likelihood reconstruction. The difficulty arises from the complexity of the reconstruction algorithm and its iterative nature. Still, the state or process reconstruction is the main method used throughout this thesis.

In the presented experiments, we resorted to the *bootstrapping* method. Assume we know what type of distribution the data obeys, and we know its moments. We use this

knowledge to randomly generate new datasets (bootstraps). These new samples are then treated the same way as the original data. The variance of the resulting ensemble illustrates the influence of the statistical errors in the data.

Let us be more specific and apply this method to single-photon experiments. In our experiments, we approximate the statistics of two-photon coincidences with Poisson distribution,

$$p(n) = \frac{\langle n \rangle^n \exp(-\langle n \rangle)}{n!}, \tag{3.60}$$

where $p(n)$ is the probability of measuring n coincidences within a given integration time, and $\langle n \rangle$ describes the mean number of coincidences averaged over many integration times. The variance of the Poisson distribution is $\langle n \rangle$.

The cartoon in Fig. 3.10 illustrates the workflow. Assume we performed tomography on an ensemble of $N \times m$ instances of the examined true state ρ_t and measured total m projections to build up seed tomogram $\mathbf{T}_0$. We reconstructed a density matrix ρ_0 from the tomogram. The probability of a successful j-th projection Π_j is

$$p_j = \mathrm{Tr}[\Pi_j \rho_0].$$

In the bootstrapping method, we use corresponding tomogram element $\langle T_{kj} \rangle = p_j N$ as a mean value $\langle n \rangle$ in eq. (3.60) in this way, we randomly generate a new tomogram $\mathbf{T}_k$. The random numbers are generated using Poisson distribution. Each new tomogram is reconstructed and quantities of interest, for example purity or fidelity, are calculated. After many repetitions of this procedure, we evaluate standard deviation on the ensemble of examined quantities, like purity. We explicitly discussed the bootstrapping method on the example of quantum states, but it is also applicable to quantum processes thanks to the channel-state duality.

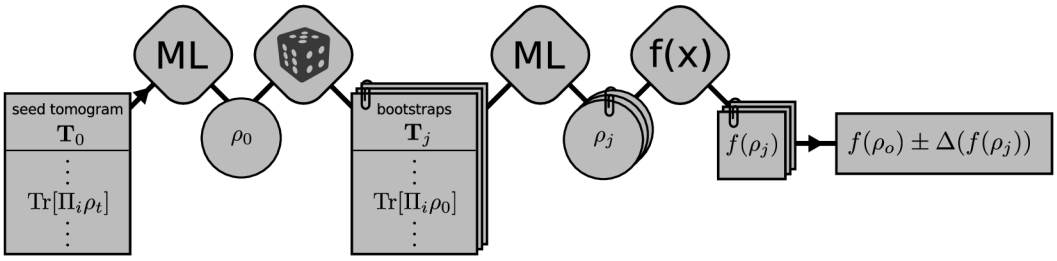

Figure 3.10: Bootstrapping workflow. From the seed tomogram and the knowledge of measurement statistics, the uncertainty of the examined function is calculated. ML - maximum likelihood reconstruction, dice icon - Poissonian pseudo-random number generator, $f(x)$ - function of interest, such as purity. See text for details.

3.2 Experimental implementation

This section is a guide for reproducing our experiments. It starts with a brief discussion of the used single-photon source, further details can be found in the thesis [1]. Then, qubit

encoding, manipulation, and its projective measurements are introduced. The discussion contains a practical guide for preparing any desired pure polarization state as well as projecting a state onto it using wave plates and linear polarizers. We do not discuss every optical element in detail because we believe it was well done earlier [3] in a similar context. The spatial qubit encoding is also discussed as well as a few practical aspects we faced in the experiments. We dedicated an extra space for reviewing the experimental implementation of the controlled-Z gate and hyperencoding because both are the pillars of the presented experiments. The section concludes with a description of experimental imperfections related to our experiments and suggestions on how to mitigate them.

3.2.1 Single-photon source

In the presented experiments, we use the spontaneous parametric down-conversion (SPDC) to generate pairs of indistinguishable photons. In the SPDC process, the energy and momentum of single photons are conserved. In our case, we select degenerate photons, which means that both photons have the same frequency. We use the type-II process, in which both generated photons are orthogonally polarized. The momentum vector of generated photons lies on o surface of a cone, one cone for each photon in pair. We use collinear generation, in which the two cones of generated photons intersect in one ray parallel to the pump photon's momentum vector.

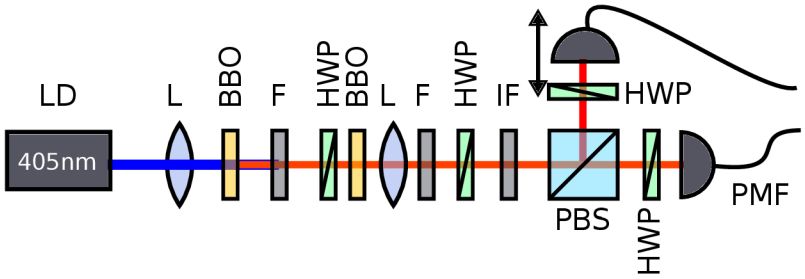

Figure 3.11: Photon pair generator. LD - laser diode, L - lens, BBO - β-barium borate crystal, F - cut-off filter, HWP - half-wave plate, IF - interference filter at 810 nm, PBS - polarizing beam splitter, PMF - polarization-maintaining single-mode optical fiber. Adopted from [129].

The SPDC source is schematically depicted in Fig. 3.11. The laser diode generates 75 mW of vertically-polarized 405-nm light. The lens focuses the pump beam into the beta-barium-borate (BBO) crystal. In the SPDC process, the pump photon turns into 810-nm photons, signal and idler. The signal (idler) photon has vertical polarization (horizontal) and propagates as an extraordinary (ordinary) beam in the crystal. The pump beam propagates as an extraordinary beam in the crystal.

Long-pass spectral filters (F) prevent the leakage of the pump beam into the single-photon signal. The pair of photons can emerge anywhere along the pump beam's extraordinary path in the crystal. Due to its ordinary propagation, the effective idler beam is elongated. This effect is known as a *walk-off*. Polarization dispersion also causes the signal and idler photons to leave the crystal at different times, making them temporally

distinguishable. A half-wave plate and a second BBO crystal serve to compensate for these effects.

The second lens collimates the generated beam. A 3-nm-FWHM line filter narrows the generated spectrum and enhances the indistinguishability of the photons. The signal and the idler photons are then spatially separated on polarizing beam splitter, their polarizations are adjusted with half-wave plates. A variable delay tunes the respective arrival times of the signal and idler photon. The generated photons are coupled into polarization-maintaining single-mode optical fibers (PMF), which guide the photons to our experiments.

The indistinguishability of the generated photons is characterized by the visibility of the Hong-Ou-Mandel dip. Typical the value ranges from 0.95 to 0.97, depending on the current degree of adjustment. We ideally want to generate Fock state $|1\rangle$ in each of the two output modes, signal and idler, avoiding contributions of higher Fock states. The second-order correlation function evaluated at zero delay $g_2(0)$ characterizes how close the generated photons are to the ideal single photons. Theoretically, the value should be zero. We use the Hanbury-Brown - Twiss type of experiment [125] to perform such a measurement. The signal output is guided to a balanced beam splitter and each output port is monitored by a single-photon avalanche diode (SPAD). The idler output is connected directly to another SPAD and serves as a heralding signal. An event on any of the first two monitoring SPADs is accepted only if the heralding detector clicks. The measured $g_2(0) \approx 10^{-2}$ indicates a low probability of undesired multi-photon contributions [129].

3.2.2 Encoding and manipulation of a single qubit

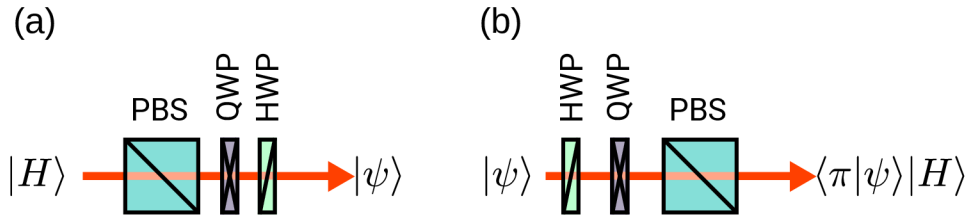

Figure 3.12: Preparation and projection of polarization qubit. PBS - polarizing beam splitter, QWP - quarter-wave plate, HWP - half-wave plate. The red line denotes the path of the photon (from left to right). (a) Preparation of the polarization qubit $|\psi\rangle$. Light is polarized using a PBS and then two unitary operations are applied. (b) Projection of state ψ onto state π. Input state is manipulated by wave-plates and the amplitude of the output state is proportional to projection $\langle\pi|\psi\rangle$.

A qubit could be encoded into various degrees of freedom of a single photon, like temporal modes, orbital angular momentum, or frequency. In this thesis, we encode qubits into spatial or polarization degrees of freedom. Let us start with polarization encoding.

Polarization qubits

The polarization encoding is the traditional choice for its simplicity of single-qubit prepa-

ration and manipulation as well as its robustness in free-space laboratory conditions. The ket formalism directly corresponds to the *Jones vector* description of polarized states, used in classical optics. Classical *Stokes description* corresponds to the quantum *Bloch description* up to a few minor differences in nomenclature. Computational states are encoded into orthogonally polarized states. Conventionally, horizontally polarized state $|H\rangle$ encodes computational zero $|0\rangle$ and vertically polarized state $|V\rangle$ encodes computational one $|1\rangle$.

Although the output from a single-photon source is polarized, our experiments often begin with the definition of polarization reference. We match the source polarization with an initial linear polarization filter that practically defines the polarization basis in the experiment. The polarizer is followed by a sequence of quarter-wave (QWP) and half-wave plate (HWP) to transform a linearly polarized state into an arbitrary state, as illustrated in Fig. 3.12(a). Unitary operator

$$U_{WP}(\Gamma,\alpha) = |\mathrm{LP}(\alpha)\rangle\langle\mathrm{LP}(\alpha)| + e^{-i\Gamma}|\mathrm{LP}(\alpha+\pi/2)\rangle\langle\mathrm{LP}(\alpha+\pi/2)|, \tag{3.61}$$

where

$$|\mathrm{LP}(\alpha)\rangle = \cos(\alpha)|H\rangle + \sin(\alpha)|V\rangle \tag{3.62}$$

describes a wave plate that introduces relative phase delay Γ between $|H\rangle$ and $|V\rangle$ states and which is rotated by angle α about its optical axis. Note that we assume zero angle of incidence. The eigendecomposition (3.61) provides a good insight into its effect on a polarization state. We see that the linear polarization $|\mathrm{LP}(\alpha)\rangle$ and $|\mathrm{LP}(\alpha+\pi/2)\rangle$ are the eigenvectors of a rotated waveplate. Therefore, in Bloch sphere representation, the waveplate rotates the state around axis $(\sin(2\alpha), 0, \cos(2\alpha))$ by angle Γ.

A sequence of QWP and HWP rotated by angles β and α, respectively, prepares a state

$$|\psi(\alpha,\beta)\rangle = U_{WP}(\pi,\alpha)U_{WP}(\pi/2,\beta)|H\rangle. \tag{3.63}$$

To prepare the desired state $|\theta\rangle$, one has to find angles α and β that satisfy a system of equations

$$\begin{aligned}
&\arg[\langle V|\psi(\alpha,\beta)\rangle] - \arg[\langle H|\psi(\alpha,\beta)\rangle] = \arg[\langle V|\theta\rangle] - \arg[\langle H|\theta\rangle] + 2k\pi,\\
&|\langle H|\psi(\alpha,\beta)\rangle| = |\langle H|\theta\rangle|,\\
&|\langle V|\psi(\alpha,\beta)\rangle| = |\langle V|\theta\rangle|,
\end{aligned} \tag{3.64}$$

which equates amplitudes and their relative phase. The following solution satisfies the system (3.64):

$$\beta = -\frac{\arcsin(y)}{2}, \tag{3.65}$$

$$\alpha = \frac{1}{4}\arctan(x/z) + \frac{1}{2}\beta + c(z), \tag{3.66}$$

where $x = \langle\theta|\sigma_x|\theta\rangle$, $y = \langle\theta|\sigma_y|\theta\rangle$, and $z = \langle\theta|\sigma_z|\theta\rangle$ are the Bloch vector components of the prepared state and $c(z) = \pi/4$ if $z < 0$ and 0 otherwise.

Alternatively, the problem could be rewritten and solved as an optimization problem in which we maximize overlap $|\langle\theta|\psi(\alpha,\beta)\rangle|^2$ over α and β. One also has to select the global maximum. We start the optimization from a few initial guesses and select the result with the greatest overlap. The numerical solution is precise just to some degree, but it suffices because the angular precision of waveplate rotation is also limited. Solution (3.65) assumes the exact waveplate retardance π and $\pi/2$. As we will show later in Section 3.2.5, this is not always the case, and we need to calculate with real retardance. Moreover, we sometimes prepare the state from a different input state. Under such circumstances, solution (3.65) does not hold and the system (3.64) has to be solved for the corresponding input state. On the other hand, the optimization-based approach is effortlessly adaptable to these cases.

Waveplates also manipulate single qubits. A single half-wave plate can serve as a phase shifter, $U_{WP}(\pi,0) = \sigma_z$, logical-not gate $U_{WP}(\pi,\pi/4) = \sigma_x$, or Hadamard gate $U_{WP}(\pi,\pi/8) = H$. The relations hold up to global phase factors. The global phases are not relevant for a single qubit and even for states where each qubit is encoded into its own single photon. In the case of multiple qubits encoded in a single photon, the global phase factor could be compensated for. A sequence of QWP-HWP-QWP in a particular rotation configuration serves as a variable phase-shifter

$$U_{QHQ}(\pi/4,\varphi/4,\pi/4) = U_{WP}(\pi/2,\pi/4)U_{WP}(\pi,\varphi/4)U_{WP}(\pi/2,\pi/4) = U_{WP}(\varphi,0).$$

This sequence realizes any single-qubit unitary operation. Given a desired unitary operation U_d, we want to find such angles α,β,γ that $U_{QHQ}(\alpha,\beta,\gamma)$ transforms a qubit the same way as U_d. In Bloch sphere representation, the task is to decompose an arbitrary rotation into a sequence of three rotations of fixed rotation angles and all rotation axes coplanar in the $x-z$ plane. The task is a special case of a more general problem of decomposing a rotation into three rotations with given axes. The problem has been solved analytically [126] for known axes and unknown rotation angles. We can't use the solution from [126] directly, because the equations were originally solved with given rotation axes and unknown rotation axes. To solve our problem, one would have to repeat the steps in [126] and solve the equations again or extract the parameters from the given solution. Both approaches are unfortunately complicated. Instead, we solve this task as an optimization problem. We represent the desired unitary operation as ket-vector $|\chi_d\rangle$ using channel-state duality, see Eq. (3.17). We also represent the sequence operator as ket-vector $|\chi_{QHQ}(\alpha,\beta,\gamma)\rangle$. Then we maximize the overlap

$$|\langle\chi_d|\chi_{QHQ}(\alpha,\beta,\gamma)\rangle|^2 \tag{3.67}$$

over angles α,β, and γ. The advantage of this numerical approach is that it can be easily adapted to any other sequence of waveplates without lengthy analytical calculations.

For completeness, we discuss how we measure a projection probability onto an arbitrary state $|\Pi_d\rangle$. Fig. 3.12(b) shows a sequence of HWP, QWP, and linear polarizing filter, $|H\rangle\langle H|$ which we use to measure projection probabilities. The projection probability of $|\pi_d\rangle$ onto a state defined by angles α and β is

$$|\langle H|U_{WP}(\pi/2,\beta)U_{WP}(\pi,\alpha)|\pi_d\rangle|^2. \tag{3.68}$$

It is equivalent to projection onto state

$$U_{WP}^{\dagger}(\pi,\alpha)U_{WP}^{\dagger}(\pi/2,\beta)|H\rangle = |\pi(\alpha,\beta)\rangle. \tag{3.69}$$

Using identity $U_{WP}^{\dagger}(\Gamma,\alpha) = U_{WP}(\Gamma,\alpha+\pi/2)$, symmetry of half-wave plate $U_{WP}^{\dagger}(\pi,\alpha) = -U_{WP}(\pi,\alpha+\pi/2)$, and substitution $\beta+\pi/2 = \beta'$ we can directly use the analytical solution (3.65) to find α,β' and then substitute back to find the angle $\beta = \beta' - \pi/2$. The output state from such projection implementation is $|H\rangle$ rather than $|\pi_d\rangle$. However, the projection probability is equivalent.

Sometimes experiment involves using a chain of single-qubit unitary operations that directly follows the preparation or directly precedes the projective measurements. Waveplates or their sequences could implement these chains, one sequence per the desired gate. Such an approach is not optimal because each optical component introduces additional imperfections, such as losses, wavefront distortions, chromatic and polarization dispersion, or beam misalignment, not to mention the resource cost. Instead, we optimize the number of components by merging single-qubit gates that directly follow the state preparation into the preparation itself. Similarly, we merge the single-qubit gates that precede the projective measurements into the projector itself. We can also merge single-qubit gates between entangling operations. It practically means finding waveplate angles for transformed desired states or operations. Section 3.2.5 will show how to apply this technique to compensate for some imperfections in the experiment.

The described method can prepare only pure states. We effectively prepare a mixed state by sequential preparation of pure states and integrating the corresponding measurement outcomes, as described in Section 3.3.2.

Path qubits

Let us move our attention to spatial qubit encoding. The path of a photon propagation encodes the qubits in this encoding. Specifically, we use a Mach-Zehnder interferometer (MZI) to define our spatial modes. Computational states $|0\rangle$ and $|1\rangle$ correspond to propagation in the arms of the interferometer denoted by states $|\uparrow\rangle$ and $|\downarrow\rangle$, respectively. Polarization qubits are easily translated into path qubits using a birefringent beam displacing crystal (BD) depicted in Fig. 3.13 (a). The crystal splits an incident beam into two parallel beams of perpendicular polarizations. In our experiments, we used a calcite crystal that introduces 6-mm or 4-mm lateral displacement. The output beams still contain polarization information, but it could be erased with wave plates addressing individual interferometric arms. Another BD completes the MZI by combining both beams again, as depicted in Fig. 3.13 (b). The second BD converts path qubits back to polarization. Thanks to the small lateral shift, this type of interferometer is inherently stable. The typical drift is in order of degrees per hour, and the fast sub-second phase fluctuations are typically around one degree. Example data from 25-cm long MZI in Fig. 3.14 (a) indicate that covering the interferometer with a simple cardboard box improves the phase stability.

In our experiments, the coherence length was short, around 100 μm. Therefore, we had to carefully select a well-matching pair of crystals to form an MZI. The crystals should

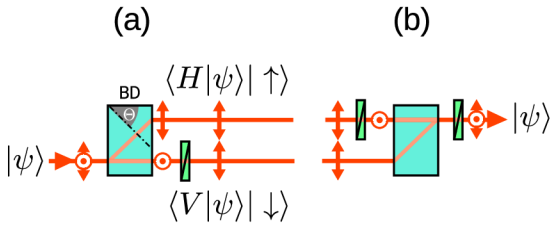

Figure 3.13: Conversion of a polarization qubit into a path qubit (a) and back (b). A vertically polarized component is depicted as an arrow pointing up perpendicularly to the plane of the paper. A horizontally polarized component is depicted as an arrow in the plane of the paper. Photons propagate in a horizontal direction from left to right. Cyan block represents a calcite beam displacer (BD). The angle θ between the direction of incidence and the optical axis of the crystal is 45 degrees. The vertically polarized component is refracted as an extraordinary wave, and therefore spatial offset is introduced. Qubit is encoded into path states $|\uparrow\rangle$ and $|\downarrow\rangle$.

have the same length to match the spatial modes as well as the temporal modes. When there is a mismatch in crystal lengths, one has to choose between good temporal overlap with a limited area of beam overlap and good spatial overlap with lower interferometric visibility. The wrong crystal matching manifests as a 'kidney' interference pattern, which is numerically simulated in Fig. 3.14 (b). The simulation evaluated two interfering Gaussian beams with 1-mm waist, wavelength 810 nm and 0.1 mm lateral displacement evaluated at the beam waist with relative phase shift π. On a free-space detector, the interferometric visibility typically reaches 96% at the best adjustment. We deal with the imperfect spatial overlap by coupling the beam into a single-mode optical fiber which acts as a spatial filter. This typically improves the interferometric visibility over 99%. The mismatch between the crystal lengths also leads to differences in fiber coupling efficiency for each beam. Imperfect interferometric visibility and fast fluctuations result in effective dephasing of the observed quantum states.

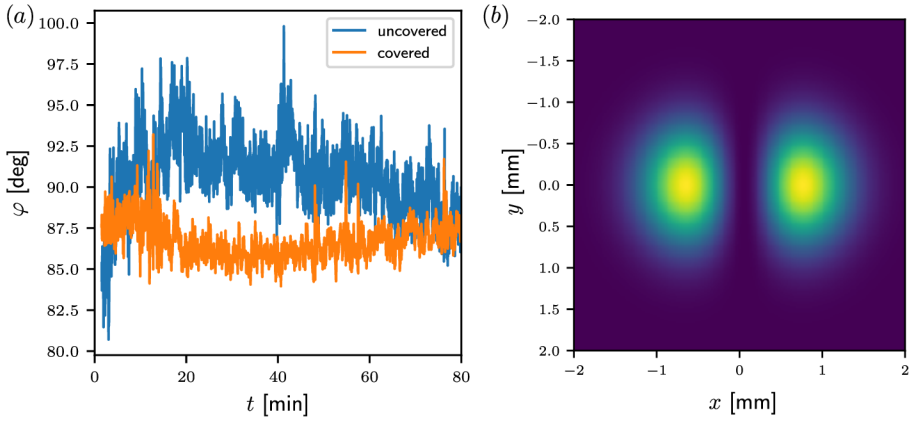

Figure 3.14: (a) Phase stability of a 25-cm long MZI with and without card box cover. (b) Simulated interference pattern when the crystals are imperfectly matched.

The phase of a path qubit is controlled by tilting the second BD. To control the tilt finely, we designed a turn-table with an embedded piezo stack, depicted in Figure 3.15. Over the range of 100 V, it introduces roughly 3π phase shift. Also, variable filtering is straightforwardly realized by attenuating individual arms. On the other hand, general unitary operations are not straightforward. We use this type of encoding to implement *hyperencoding*, explained in Section 3.2.4. The motivation for hyperencoding is the simplifying implementation of quantum gates. Before we explain the hyperencoding, we would like to explain the coupling between two polarization qubits.

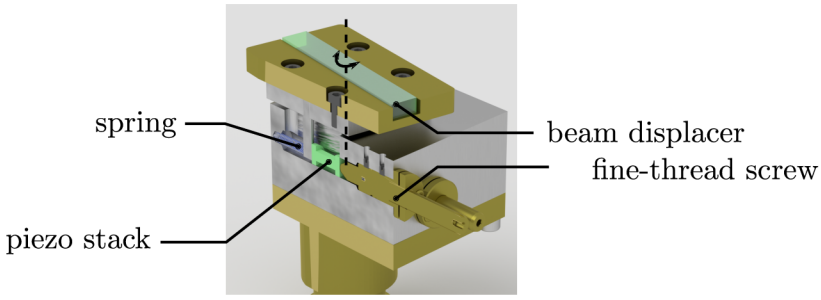

Figure 3.15: Cross-section through custom-made prism turn-table with piezo rotation control.

3.2.3 Qubit-qubit coupling - CZ gate

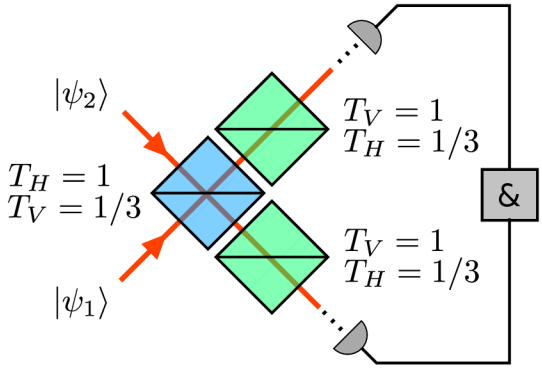

Figure 3.16: A linear optical CZ gate based on partially-polarizing beam splitters (PPBS). Blue - central PPBS, green - balancing PPBS. Only simultaneous detection events are recorded.

The CZ gate is a fundamental two-qubit entangling gate and provides a way for qubit-qubit interactions. We use the linear-optical implementation [45–47, 127, 128] as an important building block for our experiments. This section briefly reviews the working principle of the gate and some of its experimental aspects.

The CZ gate for photonic polarization qubits is depicted in Fig. 3.16. It consists of three partially polarizing beam splitters (PPBS). The central PPBS (blue) transmits a vertically polarized photon with probability 1/3 and reflects it with probability 2/3, while all

horizontally polarized photons are transmitted. Two vertically polarized photons interfere there, and the interference introduces π phase-shift. The other two PPBS elements (green) transmit all vertically polarized photons and only 1/3 of horizontally polarized photons. These elements balance the gate attenuation for horizontal and vertical polarization components. The crucial element for observing the two-photon interference is a coincidence measurement - only simultaneous detection events, so-called *coincidences*, are accepted.

Mathematical description

To mathematically describe the action of the central PPBS, let us use the Eq. (3.24) from Section 3.1.3, which we repeat here for convenience,

$$|\psi_o\rangle = \left[\left(a_o^\dagger a_o^\dagger rt - b_o^\dagger b_o^\dagger (rt)^*\right) + \left(|t|^2 - |r|^2\right) a_o^\dagger b_o^\dagger\right] |\text{vac}\rangle.$$

We do not see any interference effect when at least one of the incident photons is horizontally polarized. The horizontally polarized photon is always transmitted. 66% of vertically polarized photons are reflected and discarded by coincidence measurements. The situation changes in the case of two vertically polarized photons. We insert $t = \sqrt{T_V}$, $r = \sqrt{1 - T_V}$ into the formula to find out that the output state is π-phase shifted. The effect on input qubits could be concisely described as an operator which is diagonal in the computational H/V basis,

$$M_{PPBS0} = \text{diag}[1, \sqrt{1/3}, \sqrt{1/3}, -1/3].$$

The remaining PPBSs only reflect part of horizontally polarized photons out of the experiment and act as polarization-sensitive attenuators. Operator

$$M_{PPBS1,2} = \text{diag}[1/3, \sqrt{1/3}, \sqrt{1/3}, 1]$$

describes the effect of both PPBS on qubits. The operator product is also diagonal in computational basis and reads

$$M_{CZ} = \text{diag}[1/3, 1/3, 1/3, -1/3]. \tag{3.70}$$

The amplitude attenuation 1/3 results in the overall success probability of the gate 1/9. In the remaining 8/9 of cases, we either discard one or both photons or do not detect coincidence. When we neglect the success probability, the operation can be treated as unitary.

Because the central PPBS has an unbalanced splitting ratio, we can not observe the Hong-Ou-Mandel dip with full visibility, as described in Section 3.1.3. Instead, we utilize interference to reveal the phase shift. For example, input state $|+\rangle|1\rangle$ transforms into $|-\rangle|1\rangle$. To see Hong-Ou-Mandel dip with maximal visibility, we project the output state onto state $|+\rangle|1\rangle$. The phase shift manifests when the optical modes are matched. Consequently, the number of detected coincidences drops.

Imperfections

The two most influential experimental imperfections are imprecise splitting ratios and

partial distinguishability of the photons. We now turn our attention to these imperfections because they influence all experiments presented in this thesis.

The parasitic reflection of horizontally polarized photons on the central PPBS, $0 < T_H < 1/2$, results in partial destructive interference of two horizontally polarized photons. It also mixes incident photons of orthogonal polarization, introducing new off-diagonal terms to the operator. The operator of the central PPBS reads

$$\begin{aligned} M'_{PPBS0} &= \mathrm{diag}[2T_{H0}-1, \sqrt{T_{H0}T_{V0}}, \sqrt{T_{H0}T_{V0}}, 2T_{V0}-1] \\ &+\sqrt{(1-T_{H0})(1-T_{V0})}(|01\rangle\langle 10| + |10\rangle\langle 01|). \end{aligned} \tag{3.71}$$

Imperfect splitting ratios of the balancing PPBS elements only affect the attenuation,

$$M'_{PPBS1,2} = \mathrm{diag}[\sqrt{T_{H1}T_{H2}}, \sqrt{T_{H1}T_{V2}}, \sqrt{T_{V1}T_{H2}}, \sqrt{T_{V1}T_{V2}}]. \tag{3.72}$$

The final operator is the product $M'_{PPBS0} \cdot M'_{PPBS1,2}$.

For the description of partial distinguishability, we use operator-sum formalism or channel-state duality. Because the balancing PPBSs are not affected by partial distinguishability, we will focus on the central PPBS. Let q be the probability of two photons being distinguishable. Then the PPBS transforms a state in the following way

$$\begin{aligned} &\rho \to qM'_{PPBS0}\rho M'^{\dagger}_{PPBS0} + \\ &(1-q)(M'_{PPBS0TT}\rho M'^{\dagger}_{PPBS0TT} + M'_{PPBS0RR}\rho M'^{\dagger}_{PPBS0RR}), \end{aligned} \tag{3.73}$$

where operator

$$M'_{PPBS0TT} = \mathrm{diag}[T_{H0}, \sqrt{T_{H0}T_{V0}}, \sqrt{T_{H0}T_{V0}}, T_{V0}] \tag{3.74}$$

describes double transmission on the beam splitter and operator

$$\begin{aligned} M'_{PPBS0RR} &= \mathrm{diag}[1-T_{H0}, 0, 0, 1-T_{V0}] + \\ &\sqrt{(1-T_{H0})(1-T_{V0})}(|01\rangle\langle 10| + |10\rangle\langle 01|) \end{aligned} \tag{3.75}$$

describes double reflection. The partial distinguishability leads to a loss of inter-qubit coherence. As we suggested in Section 3.1.3, distinguishability is characterized by the visibility of the Hong-Ou-Mandel dip. Let us now show how the parameter q influences the Hong-Ou-Mandel dip's visibility. For simplicity, we insert perfect transmission coefficients into the beam splitter operators in Eq. (3.71, 3.74, 3.75, 3.72) and use Eq. (3.73) to calculate a new state. The visibility is

$$V = \frac{f(0) - f(q)}{f(0)}, \tag{3.76}$$

where $f(q)$ is the expectation value

$$f(q) = \langle +1|\rho_{out}(q)|+1\rangle.$$

After some algebra, we come to $V = q$. Of course, the correspondence does not hold exactly in the presence of other experimental imperfections. Nevertheless, it is a good way to estimate the q parameter.

The process matrix of a central PPBS is

$$\chi'_{PPBS0} = q\chi'_{PPBS0} + (1-q)(\chi'_{PPBS0RR} + \chi'_{PPBS0TT}), \tag{3.77}$$

where the constituting process matrices could be computed with Eq. (3.19) and the operators defined by Eq. (3.71, 3.74, 3.75). The application of the operator in Eq. (3.72) completes the Choi matrix.

Now we illustrate the process matrix influenced by various imperfections. The CZ gate is the fundamental building block in our experiments, and the introduced features will emerge later in the presented experiments. First, we set $T_{H1} = 0.36$ and $T_{V1} = 0.95$ and plotted the real and imaginary parts of the process matrix in Fig. 3.17 (a) and (b). To emphasize the deviation of the imperfect matrix χ_1 from the ideal theoretical matrix χ_0, we plot the relative deviation $\epsilon_{i,j} = \frac{\chi_{1,i,j} - \chi_{0,i,j}}{\chi_{0,i,j}}$ in Fig. 3.17 (c) for each compared matrix element. This type of error does not reduce coherence. We demonstrate it by plotting coherence parameter $C_{ij} = \frac{|\chi_{0,i,j}|}{\sqrt{|\chi_{0,i,i}\chi_{0,j,j}|}}$ for each nonzero matrix element in panel (d).

The imperfect splitting ratio of horizontal polarization at the central PPBS introduces extra nonzero elements in the process matrix, clearly visible in Fig. 3.17 (e) and (f) for choice $T_{H0} = 0.95$. On the other hand, setting imperfect $T_{V0} = 0.36$ only attenuates the element $\chi_{15,15}$, see Fig. 3.17 (k).

Finally, partial distinguishability, $q = 0.95$, results in decoherence. Fig. 3.17 (p) shows the reduction of the coherence parameter.

Let us remark that the post-selection and filtering might effectively amplify the gates imperfection. We illustrate this effect on an example of state $|+\rangle|+\rangle$ entering the CNOT gate, implemented with an imperfect CZ gate and Hadamard operations. The corresponding circuit diagram is depicted in Fig. 3.18 (a). We then post-select the first qubit in state $|-_\theta\rangle = \left(|0\rangle - |1\rangle \exp^{i\theta}\right)/\sqrt{2}$ and the remaining second qubit is the final output state ρ_{out}. Parameter θ controls the post-selection probability. By numerical simulation we show that with decreasing overlap $|\langle -_\theta|+\rangle|^2$ the influence of parasitic reflectance $R_H = \sqrt{1-T_H}$ is magnified. We tested values $T_H = 0.999$ and $T_H = 0.99$ and varied the post-selection overlap from 10^{-2} to 1. Fig. 3.18 compares, by means of fidelity, the output state influenced by this imperfection with the corresponding ideal output state. With near-unity post-selection probability, such imperfection barely decreases the fidelity to 0.99. At post-selection probability 10^{-2}, the fidelity is significantly reduced. The reason is that post-selection suppresses the unperturbed part of the state, while the perturbation survives the filtering and becomes significant. We encountered a similar phenomenon in the presented experiments, for example, in symmetrization experiments with the Fredkin gate that we describe in Chapter 6.

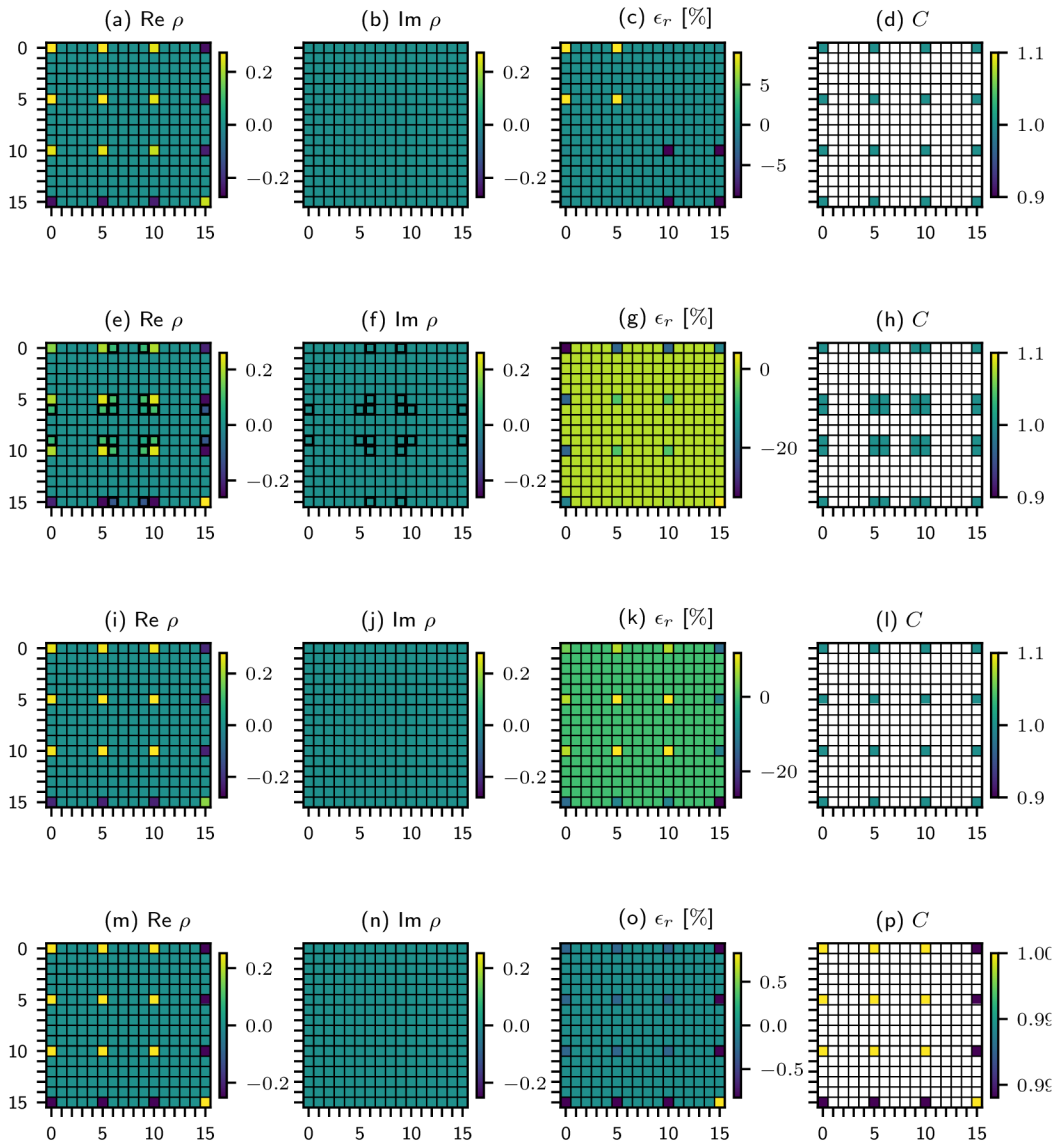

Figure 3.17: Influence of the selected imperfections on the CZ process matrix. (a-d) Imperfect splitting ratios of PPBS1, imperfect splitting ratio for horizontal (e-h) and vertical (i-l) polarization of the central PPBS0, and partial distinguishability of the photons (m-p). We plot the real (column a-m) and imaginary (column b-n) parts of the process matrix. The relative deviation size from ideal process is in column (c-o). Column (d-p) contains coherence factors. Matrices are plotted in computational basis and their labels are represented as decimal numbers. (a-d) States $|0\rangle_1$ and $|1\rangle_1$ on the first qubit are attenuated differently, leading to unequal amplitudes in the Choi matrix. (e-h) The imperfection introduces parasitic elements that are highlighted with black borders. It also causes imbalance of elements in the Choi matrix. (i-l) The imperfection lowers the element $\langle 1111|\chi|1111\rangle$. (m-p) The sizes of the off-diagonal matrix elements in the bottom row and in the rightmost column are lowered. The coherence factors quantify the relative reduction. In other words, the gate introduced decoherence for input states $|11\rangle$.

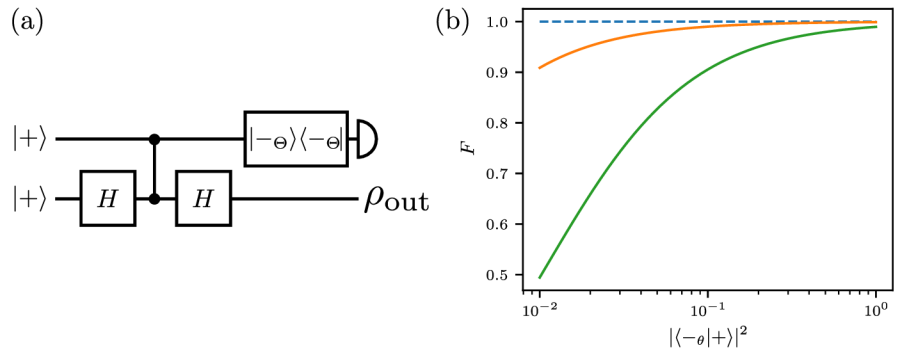

Figure 3.18: Effective amplification of imperfections in post-selected scenario. (a) Circuit diagram. (b) Fidelity of the output state processed by imperfect CZ gate with respect to the ideal output state. The horizontal axis represents the overlap between the input control qubit and the filter state. The blue dashed curve is the reference in the case without any imperfections. The orange curve represents the case with $T_H = 0.999$, and the green curve represents the case with $T_H = 0.99$.

Practical aspects

Here we discuss how to match modes in free-space implementation and perform coincidence detection, a crucial aspect in experimental practice.

Photons launched from the single-mode optical fibers into free space have a very well defined spatial mode. Fiber-coupling the output photons into the single-mode optical fibers before the detection serves as a spatial filter. In addition to beam shape, one also has to carefully align the beams' position and direction in the experiment. We use a strong auxiliary laser beam to perform the alignments efficiently. Fig. 3.19 depicts the alignment procedure in two steps, (a) and (b). Let us label the ports of the central PPBS and corresponding spatial modes with roman numerals I-IV. In step (a), we launch the laser beam from a single-mode optical fiber into free space. The beam enters the beam splitter at port I and leaves the PPBS through ports III and IV. We use collimators to couple the resulting beams into single-mode optical fibers. Mode I is thereby matched to modes III and IV. We reverse the beam direction in step (b), launching the laser beam into mode IV. The beam then splits at the PPBS and leaves it through ports I and II. Now we add and align a fiber collimator into mode II. After the adjustment, both input modes I and II should be coupled to modes III and IV. At the start of each experiment run, we adjust the fiber couplers and adjacent mirrors to ensure the highest coupling efficiency.

The goal of temporal mode-matching is to equalize the photon propagation time from the nonlinear crystal in the single-photon source to the central beam splitter. We aim to equalize the free-space optical path lengths in the experiments coarsely. The equalized free-space paths ensure that both beams, signal and idler, have similar beam size on the central PPBS as well as on the fiber-coupling lens. It improves spatial mode matching. The remaining difference in the optical path lengths could be compensated by choosing suitable combinations of input fiber lengths. Fine adjustments are realized by scanning the length of a variable delay line for one photon. The polarization modes in our experiments are matched when needed. We can control the polarization because we already encode

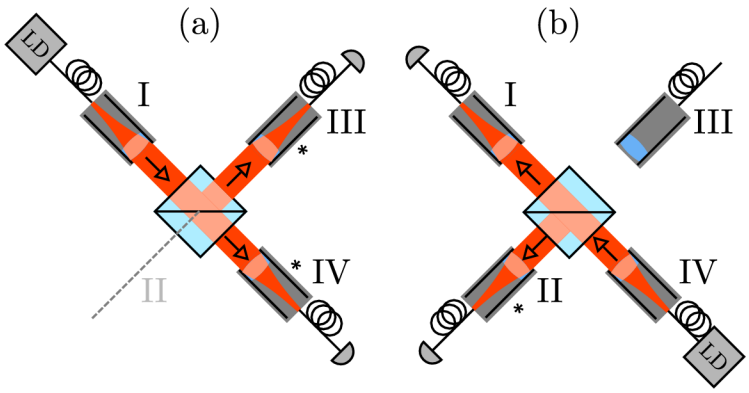

Figure 3.19: How to match spatial modes at a beam splitter. Arrows indicate the direction of beam propagation, asterisks show which fiber couplers are aligned in each step, (a) and (b). Roman numerals I-IV label ports of the PPBS and the corresponding spatial modes. LD is a fiber-coupled laser diode. Grey half-circles represent fiber-coupled photodiodes, used for alignment. For each fiber collimator, there is an auxiliary mirror used for beam-steering. For simplicity, these mirrors are not depicted.

the qubits into it. Spectral mode matching is intrinsic to the degenerate SPDC photon generation in the photon source. We can further improve it with a spectrally narrow (few nm) band-pass interference filter. Adding a 2-nm wide filter increased the visibility of the Hong-Ou-Mandel dip from 93.8% to 98.7%, but also reduced the coincidence count rate to 5% of the original value [129]. The visibility is slightly higher than we observed in our free-space experiments because, at the time, the single-photon source was freshly built and adjusted, and the Hong-Ou-Mandel dip was measured using fiber optics experimental setup that provides better spatial mode matching than free-space experiments.

The other crucial element of the gate is coincidence detection. We use an avalanche-photo diode in Geiger mode (SPAD) as a single-photon detector in our experiments. Incident photon induces an output voltage pulse with duration in the order of tens nanoseconds. To evaluate coincidences between two detectors, one has to define a short duration, *coincidence window*, which is the largest allowed time delay between two pulses that would count as a coincidence. There are two most common approaches to evaluating coincidences - using a time-to-digital converter or coincidence hardware.

Time-to-digital converter (TDC) saves a digital timestamp upon each voltage rising edge from each input channel. The recorded timestamps from two detectors are processed by computer, and those with time differences within the coincidence window are counted as coincidences.

We took a more traditional approach and used coincidence electronics in our experiments. A pulse discriminator produces a steep 2.5-ns-long voltage pulse upon a rising edge of the input pulse from SPAD. Disriminator's pulse length defines the coincidence window. Such output pulses are copied in the fan-out units, basically voltage-buffers, and the output signals are fed into pulse counters and logical AND gate. An electronic pulse counter also

counts the output of the AND gate. Compared to the modern TDC approach, the length of the cables from each detector to the coincidence unit should be equal. Electronic delay lines compensate for unequal cable lengths. Also, we cannot change the coincidence window after the measurement. However, this traditional approach is much more efficient in terms of storage and computational power requirement. Unlike the TDC approach, we do not have to store a digital number for each detection event, and we do not have to process them. A typical experiment with TDC requires the processing of gigabytes of data, depending on count-rate and integration time. Instead, three digital numbers are saved for one reading, each detector's number of single events, and their coincidences.

3.2.4 Extending the Hilbert space

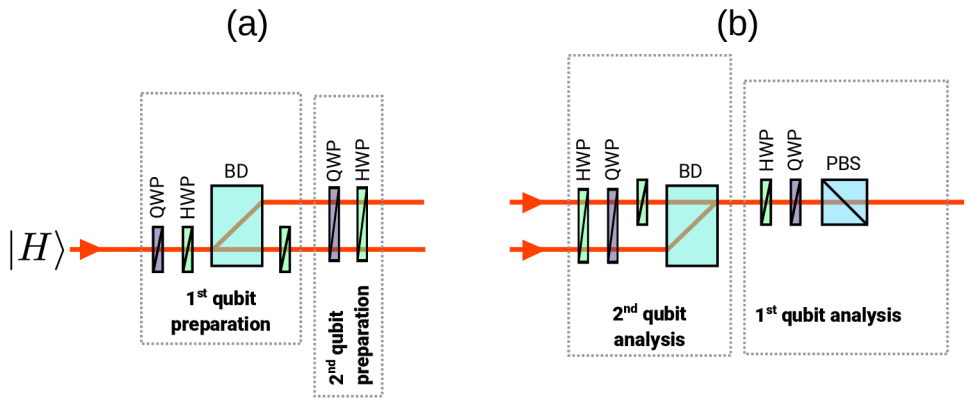

Figure 3.20: Preparation (a) and analysis (b) of qubits encoded into spatial and polarization degrees of freedom of a single photon.

The key to our experiments is to use the CZ gate as a core operating in a larger Hilbert space, which we obtained using *hypereconding*. A photon has multiple degrees of freedom. When we use them to carry *more than one qubit*, it is called hyperencoding. We use this technique for its ability to simplify the construction of our quantum gates without down-scaling the success probability [65, 130]. The price to pay is that the required classical resources scale exponentially with the number of qubits. Moreover, once qubits are hyperencoded, there are difficult to use separately. For example, it is challenging to measure one qubit while not destroying the other. Albeit the difficulty, there have been proposals and experiments showing conversions between multiple individual qubits and hyper-encoded qubits [131–133]. For these reasons, hyperencoding is generally not suitable for universal quantum computation. Despite its shortcomings, this technique is powerful because it allows realizations of proof-of-principle experiments, although the proper scalable experimental approach would be significantly more technologically and experimentally challenging.

Our experiment relying on hyper-encoded quantum gates should be rather perceived as *physical simulations* [64] of actual quantum gates. The hyper-encoding could also be a tool to manipulate quantum bits by extending the Hilbert space with auxiliary modes,

manipulating them, and shrinking the Hilbert space back to its original size. In this case, we are dealing with actual probabilistic gates, not their simulation.

In the thesis specifically, we often encode two qubits into a single photon's path and polarization. We start with a description of state preparation and analysis. A two-qubit state $|\psi_1\rangle|\psi_2\rangle = (\alpha|0\rangle+\beta|1\rangle)\otimes(\gamma|0\rangle+\delta|1\rangle)$ is encoded into initially horizontally polarized photon in two stages, depicted in Fig. 3.20 (a). First, a pair of waveplates set the polarization state $|\psi_1\rangle$ of a single photon. Then it is mapped to spatial degree of freedom using a beam-displacing crystal. So far, the prepared state is entangled, $\alpha|\uparrow H\rangle + \beta|\downarrow V\rangle$. A half-wave plate rotated to $\pi/4$ addresses the bottom spatial mode and rotates the polarization there to disentangle the polarization and spatial degrees of freedom. Finally, both beams pass through a pair of waveplates that set the polarization state $|\psi_2\rangle$ in both arms. To project hyperencoded qubit onto state $|\pi_1\rangle|\pi_2\rangle$, we use the same components in reversed order, see Fig. 3.20 (b). A pair of waveplates sets the first part of the projection $|\pi_2\rangle$. Another $\pi/4$-rotated half-wave plate addresses the top spatial mode and ensures that both spatial modes later recombine. A beam-displacing crystal acts as a polarization filter. Component $|\downarrow H\rangle$ recombines with $|\uparrow V\rangle$ component into a single beam and effectively converts the spatial qubit back to polarization. A pair of waveplates and a linear polarizer performs projection onto state $|\pi_1\rangle$, as we described in Section 3.1.1.

One might notice that inserting waveplates that address individual spatial modes results in a unitary operation controlled by spatial qubit. For example, a single half-wave plate rotated to $\pi/4$ that acts only on the bottom beam acts as a controlled-NOT gate between the hyperencoded qubits. The advantage is that these gates are deterministic. Let us note that any unitary operation on a hyperencoded qubit carried by a single photon could be deterministic [63].

In Chapter 5, we use hyperencoding to manipulate the quantum state to turn a two-qubit linear optical controlled-Z gate into a tunable controlled-phase gate. Finally, the hyperencoding is used to implement the SWAP gate, which allowed us to construct a quantum Fredkin gate, both gates are discussed in Chapter 6

Matrix description

Matrix notation is a convenient way how to enter quantum-mechanical calculations into a computer. Let us provide a few notes on matrix notation related to path-polarization qubits because it is not common to provide it in literature explicitly. We will work in computation basis with the mapping:

$$|00\rangle = |\uparrow H\rangle, |01\rangle = |\uparrow V\rangle, |10\rangle = |\downarrow H\rangle, |11\rangle = |\downarrow V\rangle.$$

The following matrix describes a beam-displacer mapping a single polarization qubit to two-qubit space

$$BD_+ = \begin{pmatrix} 1 & 0 \\ 0 & 0 \\ 0 & 0 \\ 0 & 1 \end{pmatrix}. \tag{3.78}$$

A beam-displacer that projects two hyperencoded qubits back to single-qubit space has the form

$$BD_{-} = \begin{pmatrix} 0 & 0 & 1 & 0 \\ 0 & 1 & 0 & 0 \end{pmatrix}. \tag{3.79}$$

Note that the two matrices are not Hermite conjugates even they describe the same component in different roles. The structure originates from the definition of basis vectors and the fact that our beam-displacers shift the horizontally polarized beams.

Block matrix

$$U_C(U_1, U_2) = \begin{pmatrix} (U_1) & (0) \\ (0) & (U_2) \end{pmatrix} \tag{3.80}$$

describes an action introduced by two waveplates inserted into individual spatial modes, with U_1 and U_2 being the waveplates' unitary operators. It represents a unitary operation acting on a polarization qubit that is controlled by a path qubit.

The following product describes the minimal setup with two beam displacers and a $\pi/4$-rotated wave plate between them

$$BD_{-}U_C(\sigma_x, \sigma_x)BD_{+} = \sigma_x.$$

We see that a minimal setup with incorporated hyperencoding introduces effective σ_x operation, which has to be often considered in actual experiments.

An interferometric phase shift is described by Kronecker product of phase shift matrix (see Table 3.1) and identity operator $V(\varphi) \otimes \mathbb{1}$. Operation M that affects the polarization of both spatial modes is described as $\mathbb{1} \otimes M$.

A key element in our experiments is a two-photon interference on a PPBS. Assume two crossed MZIs, depicted in Fig. 3.21, each with a single photon carrying two qubits, with overlapping nondisplaced spatial modes at the central PPBS. A sparse 16x16 matrix M_{PPBS} describes the effect of the PPBS. The matrix elements are listed in Table 3.3.

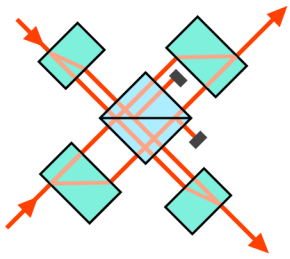

Figure 3.21: Crossed MZIs sharing a PPBS. Only photons propagating through the nondisplaced paths interfere at the central PPBS. We depicted the undetected reflections from PPBS with dark beam stops.

Let us now generalize the matrix description of the beam-displacer to n input spatial modes. The computational ket is labeled by index $k = 2i + j$, where i spans from 0 to $n - 1$ and $j = 0, 1$ labels the polarization mode. The situation and the order of the mode labels are illustrated in Fig. 3.22. The operator of a beam displacer that adds a path into

i,j	$M_{PPBS,i,j}$	i,j	$M_{PPBS,i,j}$	i,j	$M_{PPBS,i,j}$
0,0	t_H^2	1,1	$t_H t_V$	2,2	t_H^2
3,3	$t_H t_V$	4,4	$t_H t_V$	5,5	t_V^2
6,6	$t_H t_V$	7,7	t_V^2	8,8	t_H^2
9,9	$t_H t_V$	10,10	$t_H^2 - r_H^2$	11,11	$t_H t_V$
11,14	$-r_H r_V$	12,12	$t_H t_V$	13,13	t_V^2
14,14	$t_H t_V$	14,11	$-r_H r_V$	15,15	$t_V^2 - r_V^2$

Table 3.3: Matrix elements of a PPBS inside two crossed Mach-Zehnder interferometers where only bottom beams overlap at the PPBS. Other elements are zero. Elements are indexed from and including zero. Matrix is given in a computational basis, and coincidence detection is assumed.

our scheme is described as

$$BD_+ = \sum_{k=0}^{2n-1} |\mathrm{b}(k + 2(k \bmod 2))\rangle\langle \mathrm{b}k|, \tag{3.81}$$

and its shape is $2(n+1) \times 2n$. Likewise, the $(2(n-1) \times 2n)$-matrix

$$BD_- = \sum_{k=1}^{2n-2} |\mathrm{b}(k - 2 + 2(k \bmod 2))\rangle\langle \mathrm{b}k|, \tag{3.82}$$

describes the beam-displacer discarding one optical path.

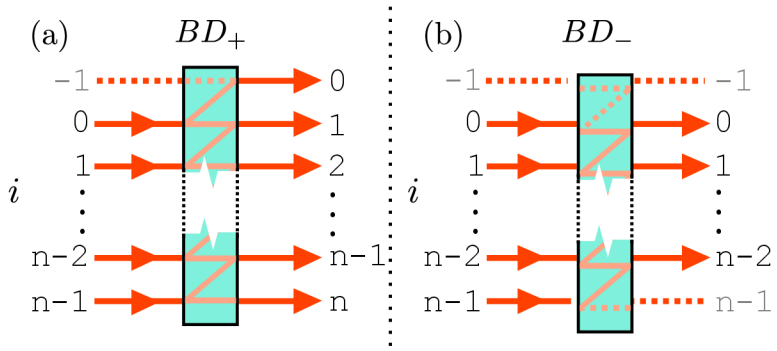

Figure 3.22: Beam-displacer that is (a) adding a path and (b) discarding a path. All valid (non-empty, used, and detected) paths are denoted with red solid lines and arrows and their mode labels, i, are given by black integers. Unused or discarded paths are drawn as dotted lines without arrows and marked with grey mode labels.

The Kronecker product

$$|\mathrm{b}i\rangle\langle \mathrm{b}i| \otimes U_{WP} \tag{3.83}$$

describes the waveplate acting on polarization in an i-th spatial mode.

Practical aspects

Here we extend the discussion of inherently stable MZI from Section 3.2.2. We often need to insert a wave-plate into a single arm of the MZI while leaving the other arm unaffected. 6-mm physical spacing of beams prevents using standard waveplates. Instead, we use *ring waveplates*. Figure 3.23 (a) shows how one beam passes through the central clearance hole while the other passes through the waveplate medium. A ring waveplate introduces a temporal mode mismatch between the two paths in MZI. We compensate for the mismatch by an additional ring waveplate placed in the other arm. The compensation is important due to our short coherence length. It would be a mistake to assume that a half-wave plate rotated to zero degrees does not change the polarization. It actually introduces a π-phase shift for a vertically polarized component. We have to take it into account. Our experiments with hyperencoded qubits typically require some unitary compensation operations. The manufacturing process for the ring-waveplate is also worth a short note. The manufacturer, TOPTEC Turnov, started with a thick quartz waveplate and drilled a central hole in it. They glued another piece of the waveplate material into the hole and grounded and polished the waveplate to the desired thickness, around 0.25 mm. The waveplate is intentionally thin to reduce lateral beam shifts in the interferometer. Then the glue was dissolved, and the central piece was removed. The final step was the application of an anti-reflective (AR) coating and assembly into housing.

Alternatively, we can use a self-compensated ring waveplate, depicted in Figure 3.23 (b). There is an embedded glass inside the ring. Its thickness was carefully selected to introduce temporal delay similar to delay caused by waveplate medium. The self-compensating waveplate was manufactured from the thick stock waveplate. The manufacturer drilled the central part and glued it in the AR-coated glass.

Custom-made and carefully calibrated liquid-crystal elements might become a favorable alternative to ring waveplates. An ordinary liquid crystal display is composed of several individually controlled cells filled with liquid crystals. Removing all auxiliary layers, like polarizers and reflective foils, leaves only the liquid crystal cell and transparent electrodes. Concatenating three of such cells and calibrating the control voltages results in a device capable of manipulating polarization with precision comparable to waveplates [134]. The study used a single twisted nematic liquid crystal cell. The challenge is to find a commercial liquid crystal display whose segments would fit the paths of a multi-path MZI. A customized multi-segment liquid crystal device would solve this problem and provide a compact way to control the polarization of individual paths in a multi-path interferometer.

3.2.5 Systematic errors compensation

This section describes how to detect and compensate for mismatched polarization handedness and unwanted fixed local unitary operations in quantum gates or quantum state preparation. Then we will discuss the reconstruction artifacts arising from imperfect knowledge of waveplate retardation and how to mitigate them.

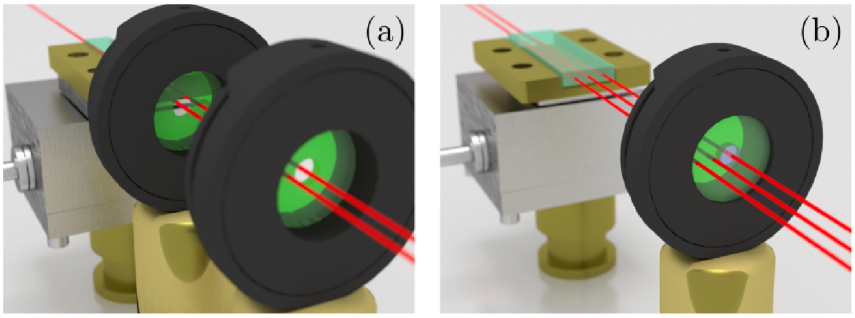

Figure 3.23: (a) Two ring waveplates, each addressing one arm in MZI. (b) Self-compensated waveplate in a multi-path interferometer. The right-most beam passes through a glass disc while the other beams pass through waveplates medium. Similarly, the center could be a waveplate, and the ring could be made of glass.

Polarization phase direction matching

A standard way to find the angular position of the waveplate axis with respect to the dial on its mechanical mount is to rotate the waveplate between two crossed linear polarizers. In the resulting angle-to-intensity signal, we identify the minimum. This measurement can't distinguish between the fast and slow axis. In the case of a half-wave plate, this is most often not an issue. In the case of a quarter-wave plate, the problems will appear when we use it in the tomography of quantum states or processes. We will describe the problem and its manifestations before we introduce a practical way to match the optical axes.

We assume the scenario described in Section 3.2.2. As a result of wrong discrimination between the fast and slow axis of a quarter-wave plate, we introduce $\pi/2$ angular error. In quantum state preparation, it will result in states with an opposite phase compared to the desired ones. In tomographic projections, we use phase-flipped projections, which leads to systematic phase-flip error in reconstruction. If we wrongly discriminate between the slow and fast axis in both the preparation and projection, the discrepancy will disappear because the phase direction is consistent.

The same problem manifests in the single-qubit process tomography as apparent low purity of the reconstructed process. If the axes are wrongly assumed in both the preparation and analysis stage, the problem again disappears. It is tempting to think that matching the phase direction at each qubit is sufficient. After all, the qubit-wise-matched phase direction works well for any quantum process of a *nonentangling* multi-qubit gate. The problem manifests with *entangling* gates. Mixing of two sub-spaces with different phase conventions results in a purity drop of the reconstructed process.

The solution is to match the phase direction for all qubits. First, we prepare a linearly polarized state $|0\rangle$ and then set up an HWP-QWP pair and a linear polarizer to realize a projector to state $|\circlearrowleft\rangle = (|0\rangle + i|1\rangle)/\sqrt{2}$. The intensity at the detector after the polarizer should be 50% of the maximum. At this point, it is not relevant which QWP's axis is fast and we do not need to know it because the definition of left- and right-handiness is rather arbitrary. It is however important to keep the definition consistent. The real

position of fast and slow axes of the QWP defines the handiness and the following steps will ensure consistency. In the next step, we place any other quarter-wave rotated to $\pi/4$ to transform the linearly-polarized state into a circular one. If the resulting projection is bright, we keep the calibration angle. If the projection is dark, we clearly have wrongly distinguished between fast and slow axes, and we add $\pi/2$ to the calibration angle. The process is repeated for every quarter-wave plate in the experiment.

The problem could also be addressed *after* the experiment by phase-flipping assumed probe and projection states in the reconstruction process. We used this approach in the earlier experiments. It is however challenging as the number of possible phase-flip combinations grows fast with the number of qubits. Moreover, the post-experiment correction of this error is applicable only to probe and projection states. If there is, for example, any waveplate-based unitary in between two entangling gates, it is difficult to fix the problem correctly.

Although the phase-direction matching is trivial, we don't recommend neglecting it as it can cause difficulties that are hard to identify, among other possible sources of imperfections.

Compensation for fixed local unitary operations

Let us start with a single pure qubit state preparation. We want to prepare a state $|\psi\rangle$ and the reconstructed density matrix is ρ_{exp}. The higher fidelity $\langle\psi|\rho_{exp}|\psi\rangle$ we achieve, the better. If there is an unwanted fixed unitary operation $U_{err} \neq \mathbb{1}$, the fidelity will be generally reduced. To find the corrective unitary operation, we want to maximize

$$f(\Theta,\Phi_1,\Phi_2) = \langle\psi|U_{1q}(\Theta,\Phi_1,\Phi_2)\rho_{exp}U_{1q}^{\dagger}(\Theta,\Phi_1,\Phi_2)|\psi\rangle \tag{3.84}$$

over parameters Θ,Φ_1,Φ_2 with U_{1q} defined in Eq. (3.6). Let us assume now a pure state $\rho_{\text{exp}} = |\xi\rangle\langle\xi|$. Let $\vec{\xi}$ and $\vec{\psi}$ be the corresponding Bloch vectors of the prepared and desired states, respectively. The correction operation just rotates $\vec{\xi}$ to match $\vec{\psi}$. Rotation about axis $\vec{r} = \frac{\vec{\psi}\times\vec{\xi}}{||\vec{\psi}\times\vec{\xi}||}$ with rotation angle $\epsilon' = \arccos(\vec{\psi}\cdot\vec{\xi})$ realizes the correction. Let $|r\rangle$ be a ket representation of Bloch vector $\vec{r}$ and $|r_\perp\rangle$ be the ket-representation of a vector $-\vec{r}$. The unitary operator $U_{corr} = |r\rangle\langle r|\exp(-i\epsilon/2)+|r_\perp\rangle\langle r_\perp|\exp(i\epsilon/2)$ represents such a rotation. Note that the solution is not unique. Any operator of form $|\psi\rangle\langle\xi| + \exp(i\gamma)|\psi_\perp\rangle\langle\xi_\perp|$ with arbitrary real γ performs the required transformation. Let us suppose that the unwanted fixed unitary operation has form $|\xi\rangle\langle\psi| + \exp(i\gamma')|\xi_\perp\rangle\langle\psi_\perp|$. Then 'correcting' it with operation $|\psi\rangle\langle\xi|+\exp(i\gamma)|\psi_\perp\rangle\langle\xi_\perp|$ would result in the unitary operation $|\psi\rangle\langle\psi|+\exp[i(\gamma+\gamma')]|\psi_\perp\rangle\langle\psi_\perp|$ which is, in the Bloch representation, rotation about axis $\vec{\psi}$ with rotation angle $(\gamma+\gamma')$ and generally not the identity operation. To fully compensate for the unwanted and unknown fixed operation, we would need to estimate γ' first, for example, with the help of quantum state tomography. In the case of mixed experimental state ρ_{exp}, we use instead of $|\xi\rangle$ the eigenstate of ρ_{exp} that has the maximal eigenvalue.

Instead of setting the waveplates to attempt the preparation of state $|\psi\rangle$ we set the waveplates in the preparation stage to prepare $U_{1q}(\tilde{\Theta},\tilde{\Phi}_1,\tilde{\Phi}_2)|\psi\rangle$. The search for the cor-

rect waveplate settings was discussed earlier in Section 3.2.2. Finally, we check whether this correction attempt increased the fidelity. We could equivalently apply the corrective operation in the detection part. Instead of projecting to a state $|\pi\rangle$, we project to state $U_{1q}^{\dagger}(\tilde{\Theta}, \tilde{\Phi}_1, \tilde{\Phi}_2)|\pi\rangle$.

Straightforward extension to n-qubit state preparation allows us to compensate factorable (local) unitary operations. Instead of optimizing over three parameters, we optimize over $3n$ parameters and apply each triplet to a local preparation or projection. Note that we can not compensate for any nonlocal (entangling) operation using this method.

It is tempting to assume that the method also serves to detect unwanted unitaries. As we have seen, it is not generally true. If the prepared state is by chance close to an eigenstate of U_{err}, we would not observe any significant reduction of fidelity. We might falsely assume that the operation is identity. To detect the unitary correctly, we have to use more probe state or even better, quantum process tomography. Let us now discuss how to compensate for systematic errors in a quantum process.

Again, let us start with the single-qubit process. We want to implement a pure process χ, equivalent to a density matrix of a 2-qubit state, and we reconstructed matrix χ_{exp}. The goal is to maximize the overlap

$$F = \mathrm{Tr}(U(\Theta_1, \Theta_2, \Phi_{11}, \Phi_{12}, \Phi_{21}, \Phi_{22})\chi_{exp}U^{\dagger}(\dots)\chi)$$

over parameters $\Theta_1, \Theta_2, \Phi_{11}, \Phi_{12}, \Phi_{21}$, and Φ_{22}. The corrective operation is a Kronecker product of single-qubit unitary operations

$$U(\dots) = U_{1q}(\tilde{\Theta}_1, \tilde{\Phi}_{11}, \tilde{\Phi}_{12}) \otimes U_{1q}(\tilde{\Theta}_2, \tilde{\Phi}_{21}, \tilde{\Phi}_{22}).$$

In the case of a pure deterministic single-qubit process, it is redundant to optimize over the first three parameters. They can be set to zero. We thus often optimize over three parameters like in the case of state preparation, but now our optimization accounts for multiple input probe states. In n-qubit processes, the local corrective operation is a Kronecker product of $2n$ single-qubit unitary operators, specified by $2\times3\times n$ parameters. The first half describes the correction of input states entering the quantum process, while the other half describes the correction of output from the process. Sometimes it is possible to omit input correction and correct only the output, but it should be judged individually. If so, the corrective operation is generally no longer an inverse of the present unwanted operations. The optimal corrective operations could be taken into account in state preparation and projection the same way as we described before.

Systematic errors in state reconstruction

The requirement for the maximum likelihood quantum state reconstruction, or generally any reconstruction method, is the knowledge of performed measurements. In the experiment, we know the projectors only approximately. The real retardances of the used waveplates might slightly differ from their nominal value for the given wavelength. This causes a discrepancy between the theoretical projectors assumed in the reconstruction process

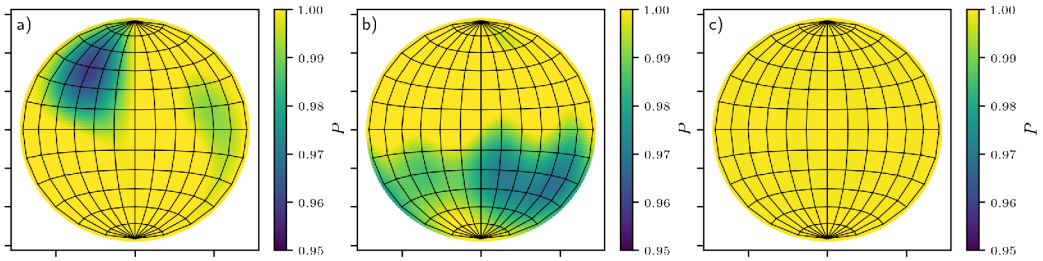

Figure 3.24: State-dependent purity drop artifact. Purity is represented with color. Input states are represented as points on the Bloch sphere in Hammer projection. a) Uncorrected waveplate imperfection ($\delta\Gamma_1 = \delta\Gamma_2 = -3$ deg), ideal projections are assumed in reconstruction. The typical purity drop area appears. b) True projectors are known and taken into account in reconstruction, but the renormalization of projectors is not performed. c) True projectors and known and taken into account in reconstruction along with proper renormalization.

and the reality. The discrepancy results in the reconstruction artifact, as we will show by the following numerical simulation.

We assume the situation from Section 3.2.2, Fig. 3.12 (b). A *pure* input state $|\psi\rangle$ is analyzed by a sequence of half-waveplate (HWP), quarter waveplate (QWP), and a linear polarizer. We set the true retardance of HWP and QWP to $\pi + \delta\Gamma_1'$ and $\pi/2 + \delta\Gamma_2'$, respectively. We project the state $|\psi\rangle$ onto six eigenstates of Pauli operators using the waveplates. We pretend not to know the true retardances and assume $\delta\Gamma_1 = \delta\Gamma_2 = 0$ when computing angular settings for waveplates to perform the projections. In the maximum likelihood reconstruction, we also assume precise projections onto eigenstates of Pauli operators. The whole procedure is repeated with $|\psi\rangle$ scanning over the Bloch sphere. In Figure 3.24, we plot the purity of the reconstructed state. We see that in the north-western area of the Bloch sphere, the reconstruction artifacts manifest as a decrease of purity. The minimal observed purity $\min_\psi P$ quantifies the quality of reconstruction. The lower $\min_\psi P$, the worse the artifact is. With perfect knowledge of $\delta\Gamma_i'$, the artifact vanishes.

In Section 3.1.4, we silently assumed that the used projectors $|\pi_i\rangle\langle\pi_i|$ add up to a multiple of identity operator. In this case, the assumption does not hold, and we have to renormalize the projector sum $H = \sum_i |\pi_i\rangle\langle\pi_i|$ [112]. Without the renormalization, the artifact remains, albeit the knowledge of the true retardances, as the simulated data in Fig. 3.24 (b) illustrate.

We introduce a renormalized sum

$$H' = \frac{\sum_i |\pi_i\rangle\langle\pi_i|}{\sum_i \langle\pi_i|\rho|\pi_i\rangle} \tag{3.85}$$

and use it to renormalize the reconstruction operators

$$K' = (H')^{-1/2} K (H')^{-1/2}, \rho' = (H')^{1/2} \rho (H')^{1/2} \tag{3.86}$$

during the iteration process (3.36) to perform the reconstruction correctly [112]. Fig. 3.24 (c) shows that with the proper renormalization and knowledge of retardances, the artifact vanishes.

Knowing the retardance, we can use the method from Section 3.2.2 to find waveplate angles α and β to realize the desired projection correctly. Now we insert into Eq. (3.69,3.61) the true retardances.

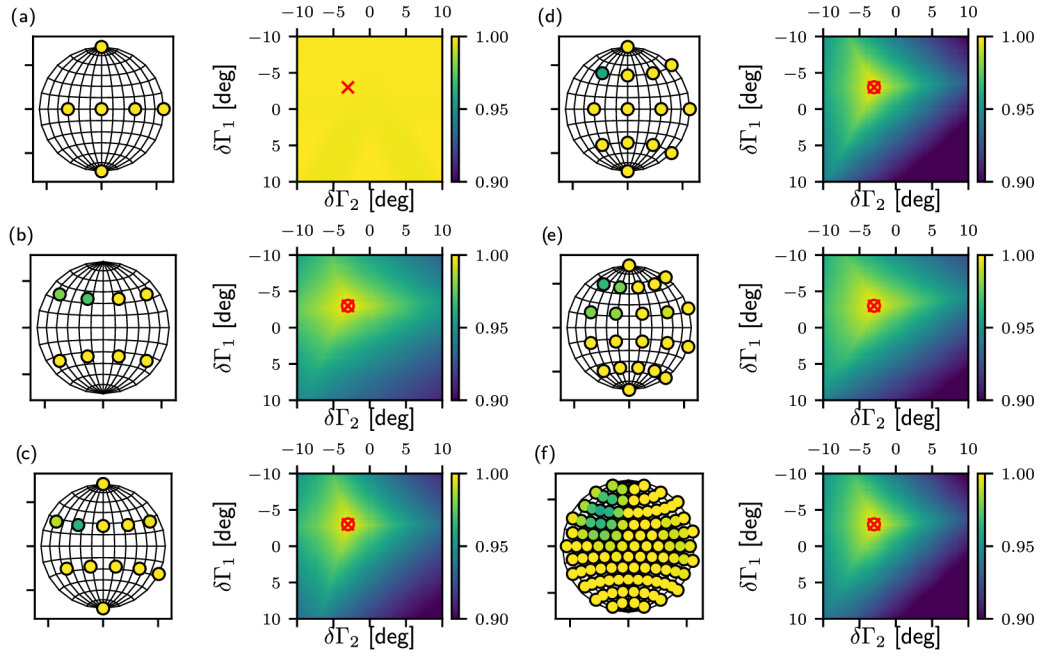

Figure 3.25: Search for true retardances. Probe states are depicted as points on the Bloch sphere and the purity of respective reconstruction without correction is color-coded. The minimal observed purity is plotted as a color map for the assumed retardance correction $\delta\Gamma_1$ and $\delta\Gamma_2$. We did the numerical simulation for 6 (a), 8 (b), 12 (c), 14 (d), 22 (e), and 108 (f) probe states. The red $\times$ shows the true values $\delta\Gamma_1' = -3$ deg and $\delta\Gamma_2' = -3$ deg, red circle shows the optimal value found by numerical optimization.

The question is *how* to know the true retardances of the used waveplates. One could measure the retardances independently in a trusted apparatus using the same wavelength as in the experiment, for example, using quantum process tomography. How do we estimate the retardance *without* perfect reference states and projectors? Brańczyk et al. [135] suggested including the unknown imperfection as a parameter in the reconstruction process. We consider an alternative way.

We use a set of probe states to sample the reconstruction-induced purity drop, and then we vary the assumed retardances to minimize the reconstruction artifact. The optimal retardances are used in the final reconstruction. The sampling has to be dense enough to spot the artifact. We require that function $\min_\psi P(\delta\Gamma_1, \delta\Gamma_2)$ has a single well-identified maximum. We tested the approach with 6, 8, 12, 14, 22, and 108 probe states quasi-uniformly distributed over the Bloch sphere and we plot the results in Fig. 3.25 (a-f). Starting from 8 probe states, the function $\min_\psi P(\delta\Gamma_1, \delta\Gamma_2)$ has a single well-localized maximum. Adding more probes does not significantly change the function, although it is possible that with

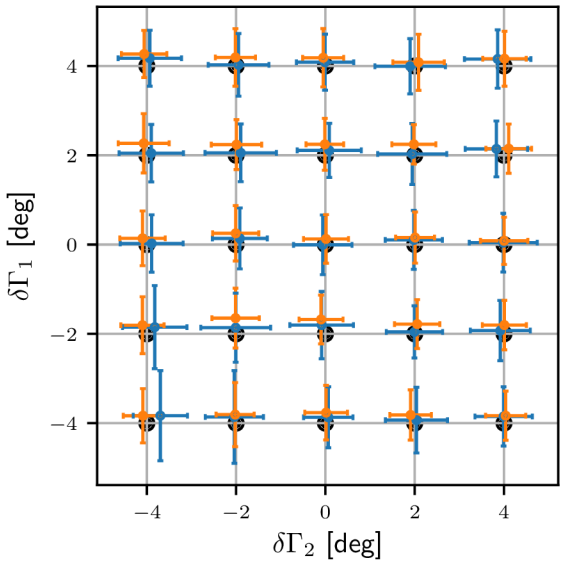

Figure 3.26: Reliability of waveplate retardance estimation. Simulated true retardance deviations $\delta\Gamma_i'$ are depicted as black dots. For each pair $(\delta\Gamma_1', \delta\Gamma_2')$, we repeat the experiment 100 times. We use normalized intensity and assume normally distributed intensity noise with $\sigma = 10^{-2}$. The mean values of the estimates are plotted as dots with 1-std error bars. The blue color represents the case 12 probe states, while the orange color represents the case with 22 probe states.

more information, the variance of the estimated parameters reduces.

To test the reliability of the method, we performed more numerical simulations. In each of them, we tried the search for multiple true pairs $(\delta\Gamma_1', \delta\Gamma_2')$ in the presence of noise and compared the results with nominal values. The results in Fig. 3.26 show that the true retardances are revealed reliably and repeatably.

Systematic errors in state preparation

With calibrated waveplates in quantum state tomography, we can also improve the precision of quantum state preparation. Wrongly assumed retardance of the waveplate in the preparation stage would result in discrepancies between the expected and reconstructed state. The discrepancy is depicted in Fig. 3.27. We quantify the quality of preparation as a mean fidelity of observed probe states. There is a pair of waveplate angles (α_i, β_i) used to prepare each probe state $|\psi_i\rangle$. For each probe, we use the waveplate settings (α_i, β_i) in Eq. (3.69, 3.63) together with assumed retardances to calculate the expected preparation and we compare it to the observed one. Then we maximize the mean overlap between the expected and observed states by varying the assumed retardances. Finally, we use our estimate of the true retardances for the correct calculation of waveplate angles to prepare any desired state $|\psi\rangle$.

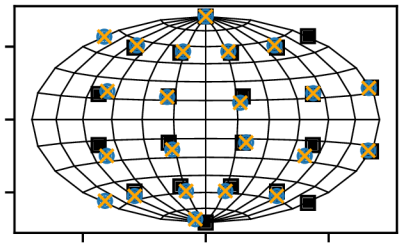

Figure 3.27: Discrepancies in state preparation. All states are plotted on the Bloch sphere in Hammer projection. Black squares represent originally desired states. Blue dots represent the state reconstructions. Orange crosses are the expected preparations with estimated true retardances. The true values in the simulation were $\delta\Gamma_1' = 5$ deg, $\delta\Gamma_2' = -5$ deg. The initial mean infidelity was $1.94 \cdot 10^{-3}$ and the optimal mean infidelity $0.14 \cdot 10^{-3}$.

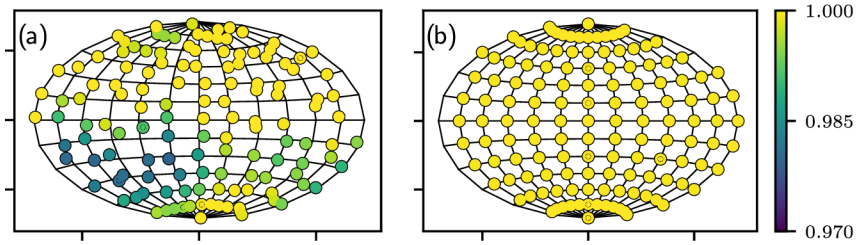

Figure 3.28: Comparison of state preparation and reconstructions before (a) and after (b) systematic errors correction. Reconstructed states are plotted as points on Bloch sphere in Hammer projection. Their purity is color-coded.

We conclude our simulations by simulating single-qubit self-calibration. The input state is prepared with half- and quarter-wave plates, having deviations $\delta\Gamma_1'$ and $\delta\Gamma_2'$, respectively. Another pair of half- and quarter-wave plates with parameters $\delta\Gamma_3'$ and $\delta\Gamma_4'$ is used to set the tomographic projections. The desired set of probe states samples the latitude and longitude of the Bloch sphere uniformly. We simulate the tomograms and plot the reconstructions as points on the Bloch sphere in Fig. 3.28 (a). The purity of the reconstruction is coded into color. We first find $\delta\Gamma_3'$ and $\delta\Gamma_4'$ by optimizing $\min_\psi P$ and then correct the reconstruction projectors. With corrected reconstructions, we find $\delta\Gamma_1'$ and $\delta\Gamma_2'$ by maximizing the mean fidelity between observed and expected states. In the last step, we correct the waveplate settings for both preparation and projection and repeat the experiment. The outcome from the repeated experiment is plotted in Fig. 3.28 (b). Both state preparation and reconstructions are significantly better.

We tested the method experimentally using a single beam of strong laser light and PIN photodiode as a detector. First, as a reference, we assumed perfect waveplates and prepared and reconstructed many probe states. Their reconstructions are plotted in Fig. 3.29 (a) as points on Bloch sphere. Due to reconstruction artifact and the wrong assumption on

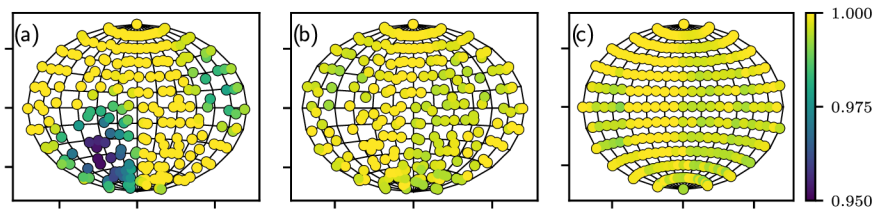

Figure 3.29: Experimental test of self-calibrated tomography. Comparison of state preparation and reconstructions before (a) any corrections, (b) with corrected reconstruction, and (c) after both reconstruction and preparation corrections. Reconstructed states are plotted as points on Bloch sphere in Hammer projection. Their purity is color-coded.

waveplate retardances, the reconstruction purity drops to 0.95 and clearly there are discrepancies in state preparation. We used the probes to find a correction to the retardance and took it into account in the reconstruction. Fig. 3.29 (b) illustrates that the reconstruction artifact is mitigated. Unfortunately, we missed one meridian in the experiment due to a typo in the control script. Nevertheless, we used the reconstructions to estimate the correction to the preparation waveplates' retardance and took them into account in the new measurement. We also calculated a new angular setting for analysis waveplates to get the realized projections closer to the originally assumed projectors. With these new settings, we do not have to perform renormalization. The results in Fig. 3.29 (c) indicate a successful reduction of systematic errors both in preparation and reconstructions.

The question of whether the presented method improves the quality of implemented quantum logic gates remains open. Unfortunately, we explored the self-correction method after the main experiments were done.

3.3 Data processing recipes

In science, data processing is a routine task. Our research was not different. Although I spent at least half of the experimental effort on data analysis, we usually did not discuss it in publications. This section at least discusses the nontrivial data processing tasks as we used them to realize the presented experiments. I hope that it will be helpful to anyone who will face similar data processing tasks as I did.

3.3.1 Tomogram indexing system

Tomogram of a n-qubit state contains K^n entries, where K is the number of projections. During the data analysis, one typically needs to browse through entries or select subtomograms. Instead of introducing additional labels to each entry, we utilize the line numbers (readings order) as an indexing system. We will illustrate this on n-qubit state tomography with projections on six eigenstates (3.27) of Pauli operators. We assume that projections are measured in this order: $|0\rangle; |1\rangle; |+\rangle; |-\rangle; |\circlearrowleft\rangle; |\circlearrowright\rangle$. We label these states with

integer numbers from 0 to 5. During the tomography, we measure every combination of these $K = 6$ projections, in total 6^n projections. A tuple $\{k_i\}$ could label each projection. Number k_i is an integer ranging from 0 to 5. We can represent the tuple with an integer

$$I = \sum_{i=0}^{n-1} 6^i k_i. \tag{3.87}$$

We typically order the measurement with ascending I and call it *standard order*. Line-index is also a label of projection. To identify the projection from the line number I, we have to represent I as a base-6 number. An i-th digit directly labels the local projection k_i. To select arbitrary projection labeled by tuple a $\{k_i\}$ we only calculate the line number I.

Sometimes, we have a different number of projections for every qubit. For example, when we have access to orthogonal projections in a single run at some qubits. Let K_i be the number of projections on the i-th qubit. Then the relation between labels k_i and the line index is

$$I = \sum_{i=0}^{n-1} k_i L_i, \tag{3.88}$$

with $L_i = \prod_{j=0}^{i-1} K_j$ for $n-1 \geq i \geq 1$ and $L_0 = L_n = 1$. Decomposition of I into labels k_i only requires integer division, represented by symbol //, and modulo calculation,

$$k_i = (I \mathrm{mod} L_{i+1}) // L_i. \tag{3.89}$$

It is slightly more practical to calculate k_i from $i = n-1$ to 0. In the first step, let $J = I$. Then iterate with index i from $i = n-1$ to $i = 0$ and in each round calculate $k_i = J // L_i$ and perform decrement $J \to J - k_i L_i$. Factors L_i should be calculated prior to the iteration as they do not depend on I.

In some cases, we need to acquire a tomogram in a different order than ascending I, for example, to speed up the measurement [136]. Then we can use original line numbers as labels, acquire the tomogram in any order and then sort the tomogram by labels back into the standard order.

Let us illustrate the indexing system on an example of a 2-qubit 6-state tomogram and partial trace task. We want to reconstruct the second part of the qubit, tracing the first out. Therefore, we select a sub-tomogram that has all projections of the first qubit $|0\rangle$, $k_0 = 0$, and add it to a sub-tomogram with $k_0 = 1$. The tomogram index and labels are for illustration provided in Table 3.4. To select the first sub-tomogram, we use lines $I' = 6k_1$ and to select the second, we use lines $I'' = 6k_1 + 1$, k_1 iterating from 0 to 5. The first tomogram consists of lines 0, 6, 12, 18, 24, and 30, while the second tomogram consists of lines 1, 7, 13, 19, 25, and 31. The sum of these tomograms is a tomogram of a partially traced state.

The main advantage in comparison to sequential search for a matching key is the performance and simplicity. We do not have to search the file or the array for the matching label. Instead, we directly pick the right line. In our experiments, we use this method to select state tomograms or truth tables from quantum process tomograms, perform a partial trace on data, or effectively reconstruct a mixed state.

I	$\{k_i\}$	$\|\pi\rangle$	I	$\{k_i\}$	$\|\pi\rangle$	I	$\{k_i\}$	$\|\pi\rangle$
0	00	HH	12	20	DH	24	40	RH
1	01	HV	13	21	DV	25	41	RV
2	02	HD	14	22	DD	26	42	RD
3	03	HA	15	23	DA	27	43	RA
4	04	HR	16	24	DR	28	44	RR
5	05	HL	17	25	DL	29	45	RL
6	10	VH	18	30	AH	30	50	LH
7	11	VV	19	31	AV	31	51	LV
8	12	VD	20	32	AD	32	52	LD
9	13	VA	21	33	AA	33	53	LA
10	14	VR	22	34	AL	34	54	LR
11	15	VL	23	35	AR	35	55	LL

Table 3.4: Example of 2-qubit 6-state tomogram ordering. I is the index, k_i is its i-th digit in base-6 representation, and $|\pi\rangle$ denotes the projection.

3.3.2 Mixed state preparation by temporal multiplexing

Sometimes the experiments require the preparation of mixed states. In our experimental setup with input polarizers, it could not be done directly. Let us start with a single polarization qubit. Conventionally, mixed polarization means that the polarization state changes rapidly and randomly in time or detection area. The degree of polarization relates to the probability distribution of orthogonal polarization. Commercially available depolarizes changes the polarization pseudo-randomly in the beam area or modulate the polarization state much faster than integration time. We will discuss a partially polarized state described by a density matrix. A density matrix ρ could be written as a statistical mixture of its two orthogonal eigenkets $\rho = \lambda_1|\lambda_1\rangle\langle\lambda_1| + \lambda_2|\lambda_2\rangle\langle\lambda_2|$. We can think of it as a stream of photons coming randomly in those two orthogonal polarizations with probabilities λ_1 and λ_2. Any measurement on the state would provide the same result if we split the original integration time T into two parts, $\lambda_1 T$ and $\lambda_2 T$, in which we prepare input states $|\lambda_1\rangle$ and $|\lambda_2\rangle$ respectively. It could be understood as sorting the input photons in time by their polarization, as we illustrate in Fig. 3.30.

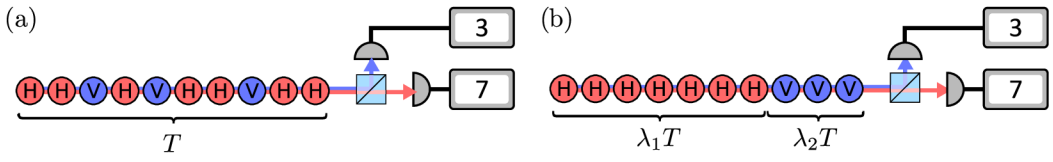

Figure 3.30: (a) Truly partially polarized state in H-V measurement. Photons are horizontally and vertically polarized with probabilities λ_1 and λ_2, respectively. (b) Emulation of mixed state by sequential preparation and integrating results. The detected counts in these two cases do not differ.

The preparation of a multi-qubit partially mixed state is just an extension of the described approach. The sum $\sum_i \lambda_i|\lambda_i\rangle\langle\lambda_i|$ decomposes the desired density matrix into its eigenstates. We split the integration time T into intervals $T\lambda_i$ in which we prepare pure

state $|\lambda_i\rangle$ a perform any desired measurements. Such preparation is only feasible if we can prepare the eigenstates. For example, the states $|\lambda_i\rangle$ in multi-qubit scenarios could be entangled and beyond our preparation capabilities.

We use the described approach to prepare the mixed states in our experiments effectively. With a time-integrating detector, such as a counter of electronic pulses, one needs to know the desired λ_i before the measurement to set the proper integration time. It is however possible to mix any combination of λ_i *after* the experiment. The first way is to use a time-to-digital converter (TDC) to register the detection events and measure each $|\lambda_i\rangle$ for a fixed integration time T. To get count rates in defined intervals, one only counts the number of time-tags between time 0 and $\lambda_i T$ for every preparation $|\lambda_i\rangle$. Sum of the counts is equivalent to measurement on the mixed state.

The second way requires a counter and approximation. All states $|\lambda_i\rangle$ are measured with the same integration time T. We approximate the mean count rate of i-th prepared state $|\lambda_i\rangle$ by its measured value $\bar{C}_i \approx C_i$. A weighted sum $C = \sum_i C_i \lambda_i$ represents counts equivalent to measurement on the mixed state. The used approximation will result in different uncertainties compared to correct the TDC-based approach.

To prepare a maximally mixed state, we can choose $|\lambda_1\rangle$ arbitrarily and $|\lambda_2\rangle$ to be orthogonal. Because we can't guarantee perfect orthogonality of prepared state in the experiment, we often compose the maximally mixed state from three pairs of states that form a three mutually unbiased basis. In the experiment, we use all eigenstates of Pauli operators.

3.3.3 Partial trace over arbitrary qubits

Here we provide a simple numerical method on how to calculate arbitrary partial trace of a n-qubit density matrix. For a n-qubit density matrix, let a n-bit number m specify which qubits should be traced out. If the j-th bit in the binary representation of m is 1, then the corresponding j-th qubit will be traced out. For example, binary number 0b101 would mean trace over the first and third qubit.

Let us introduce an auxiliary function $M(i, m)$, which operates on the n-bit mask number m and $(n - |m|_h)$-bit index number i, where $|m|_h$ is the number of ones in bit-representation of m, known as *Hamming weight*. The function assigns the bits from i into a new n-bit number into positions, where the bits of m are ones, keeping the original order and setting the remaining bits to zeroes, for example

$$M(0\text{b}101, 0\text{b}1011) = 0\text{b}\underline{1}0\underline{01}.$$

With function M, the following sum describes a matrix element of a partial sum outcome

$$\mathrm{Tr}^m(\rho)_{ij} = \sum_{k=0}^{2^{|m|_h}-1} \rho_{I(i,k,m)J(j,k,m)}, \tag{3.90}$$

where

$$I(i, k, m) = M(i, \neg m) + M(k, m), \tag{3.91}$$

$$J(j, k, m) = M(j, \neg m) + M(k, m). \tag{3.92}$$

with $\neg m$ being a bit-wise complement of m. Sum index k iterates through all $2^{|m|_h}$ traced-out matrix elements, the term $M(k, m)$ describes the variable part of the index that we iterate through, while the term $M(i, \neg m)$ is the constant component of the index and corresponds to the qubits that are not traced over. Listing 3.3 shows an example of how to implement this method in Python.

Listing 3.2: Partial trace

```
#Auxiliary function M
def expandnum(number, mask, bits):
  s = 0
  k = 0
  for j in range(bits):
    mbit = (mask >> j) & 0b1
    vbit = (number >> k) & 0b1
    s += ((vbit*mbit) << j)
    k += int(mbit)
  return s

def TraceOverQubits(M,li):
  mask = 0
  negmask = 0
  for i, k in enumerate(li[::-1]):
    mask += int(k)*(2**i)
    negmask += int(not(k))*(2**i)
  bits = len(li) #number of qubits in M
  nbits = sum(li) #number of traced-out qubits
  ndim = 2**(bits-nbits) #dimension of result matrix
  sumdim = 2**nbits #how many elements we sum
  MS = np.zeros((ndim, ndim), dtype=M.dtype)
  for i in range(ndim):
    i0 = expandnum(i, negmask, bits)
    for j in range(ndim):
      j0 = expandnum(j, negmask, bits)
      for k in range(sumdim):
        k0 = expandnum(k, mask, bits)
        MS[i,j] = MS[i,j] + M[i0+k0,j0+k0]
  return MS
```

3.3.4 Partial transposition over arbitrary qubits

Here we show how to practically perform general partial transpose of a n-qubit density matrix. Let us introduce transposition number m, which specifies parts to be transposed. The j-th part is transposed if the corresponding j-th bit of number m is 1. The transposed matrix is constructed by relabeling row and column indices,

$$\rho_{ij}^{T_m} = \rho_{IJ},$$

where i and j are the row index and column index, respectively. Both indices span from 0 to $2^n - 1$. The relation

$$I = i - \Delta_{ij,m}; J = j + \Delta_{ij,m}$$

describes the index mapping. Factor Δ is specified with transposition mask m,

$$\Delta_{ij,m} = (i\&m) - (j\&m),$$

where symbol & represents bit-wise logical AND operation. Indices of row and column could be represented as binary numbers. In the partial transposition, we swap some bits of indices j and i. Bits to be swapped are specified by a mask m. Adding factor Δ to j and subtracting it from i effectively performs the swap. Alternatively, masked XOR-based bit swapping might be used.

An example of Python implementation is provided in Listings 3.3.

Listing 3.3: Partial transposition. M is an array of binary values corresponding to mask m.

```
def PartialTranspose(M, li):
  dim = M.shape[0]
  mask = 0
  for i, k in enumerate(li[::-1]):
    mask += k*(2**i)
  MT = np.zeros_like(M)
  for i in range(dim):
    di = i & mask
    for j in range(dim):
      dj = j & mask
      deltaij = di - dj
      MT[i - deltaij, j + deltaij] = M[i,j]
  return MT
```

Chapter 4

Four-qubit controlled-Z gate

As mentioned in Chapter 2, the number of qubits that can be simultaneously coherently controlled in an experiment is growing. It opens new opportunities and challenges. Any operation of multiple qubits can be decomposed into a sequence fundamental two-qubit or three-qubit gates and local single-qubit gates [B1]. The fundamental two- and three-qubit linear optical quantum logic gates have been successfully constructed in the past. However, the experimental realization of such a decomposition is challenging in the context of linear optical quantum computing. Having more quantum logic gates would require generating and detecting more photons simultaneously. This means exponentially scaling down the probability of successful gate action, not to mention the experimental difficulties. Dedicated multi-qubit gates could provide us the experimental feasibility.

The experiments in this chapter and also in Chapters 5 and 6 show how to construct three- and four-qubit quantum gates without using more than two photons. Instead of using more photons, we exploit path and polarization degrees of freedom of two photons to construct the gates. The presented quantum gates mean an important step beyond the previous implementations of two- [43–47, 66, 137] and three-qubit [2, 65, 138] linear optical quantum gates. The experiments aim to build and characterize the few-qubit gates and, with their help, investigate various quantum information schemes involving the few-qubit operations. We hope that some of our findings, acquired with linear quantum optics, could be transferable to other platforms.

The methods and results described in this chapter specifically have been published as [A1] and [A2]. The presented four-qubit generalized controlled-Z gate (C^3Z gate) logic gate has the same success probability as a single CZ gate [45, 46, 127]. The success probability of the C^3Z gate is higher than its equivalent decomposition into two-qubit entangling gates.

The constructed quantum logic circuit combines several two-qubit quantum controlled-rotation gates, single-qubit gates, and a C^3Z gate. The C^3Z gate flips the sign of the state only if all four qubits are in the computational basis state $|1\rangle$, as depicted in Fig. 4.1, and is described by unitary operation

$$U_{C^3Z} = \mathbb{1}_{16} - 2|1111\rangle\langle 1111|. \tag{4.1}$$

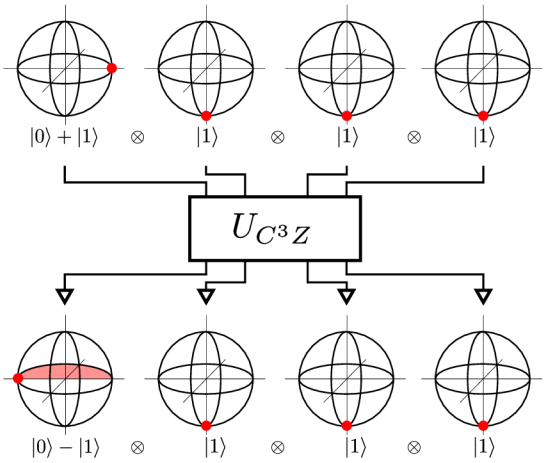

Figure 4.1: A visualization of C^3Z gate action. Three control qubits in state $|1\rangle$ cause the CZ gate to introduce a π-phase shift to the target qubit.

Operator $\mathbb{1}_{16}$ denotes the identity operator on Hilbert space of four qubits. In our implementation, qubits 1 and 2 are hyperencoded into the polarization and path of the signal photon, respectively, while qubits 3 and 4 are similarly encoded into polarization and path of the idler photon. The two-qubit controlled-rotation gates applied to polarization and path qubits supported by the same photon can be implemented deterministically, while the core four-qubit C^3Z gate is probabilistic, with a theoretical success probability of $\frac{1}{9}$. The implemented quantum logic circuit is illustrated in Fig. 4.2.

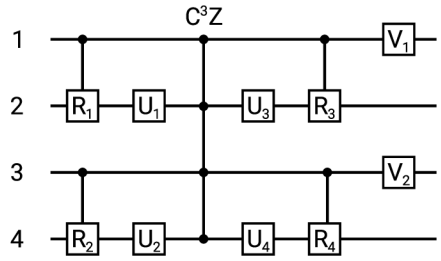

Figure 4.2: Scheme of the implemented quantum logic circuit. R - controlled half-wave plate operations, U - arbitrary single-qubit operations, V - single-qubit phase shift.

The four-qubit quantum logic circuit is a complex device, and its complete experimental characterization would require the determination of $2^{16} - 1 = 65535$ parameters. Here we employ Hofmann fidelity bounds [2, 22, 66] and Monte Carlo sampling techniques [24, 25] to efficiently characterize the performance of the quantum logic circuit. Our scheme provides a suitable platform for testing and illustrating the usefulness of these

methods, which can also serve for efficient evaluation of other kinds of multi-qubit quantum gates. We find that the fidelity F_{C^3Z} of the four-qubit C^3Z gate lies in the interval $0.872(6) \leq F_{C^3Z} \leq 0.928(4)$ and the Monte Carlo sampling provides an explicit fidelity estimate $F_{C^3Z} = 0.912 \pm 0.011$. We show that our device can generate a four-qubit GHZ-type entangled state whose fidelity with the ideal state and purity exceed 90%. Moreover, using suitable entanglement witnesses, we verify that the generated state exhibits genuine four-partite entanglement.

4.1 Experimental setup

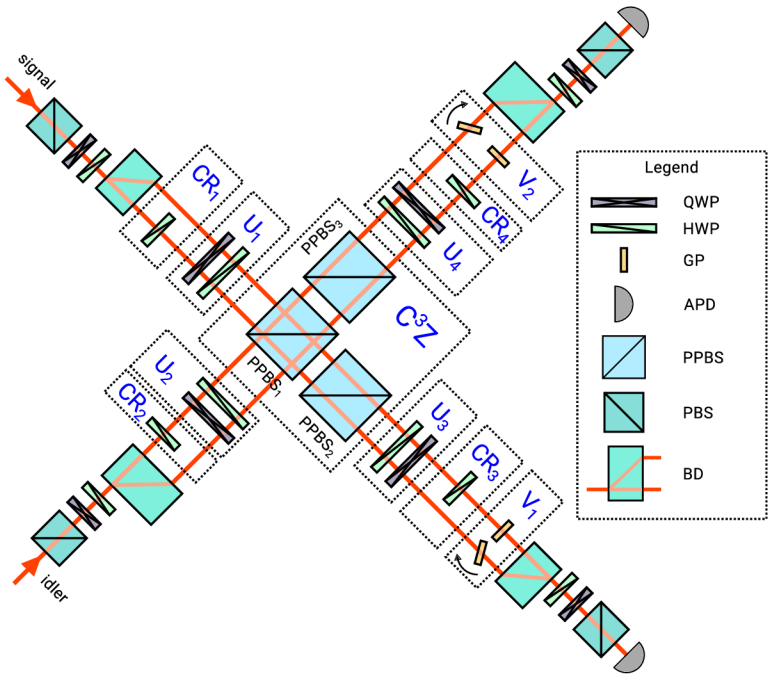

Figure 4.3: Experimental setup. The central four-qubit C^3Z gate is implemented by two-photon interference on a partially polarizing beam splitter $PPBS_1$ followed by two additional PPBSs, which serve as partial polarization filters. Notice that only the left and lower beams overlap and interfere on $PPBS_1$. Single-qubit unitary gates U_j are implemented by a sequence of a rotated half-wave plate HWP and quarter-wave plate QWP, which address both paths in a Mach-Zehnder interferometer formed by two calcite beam displacers BD. The two-qubit controlled rotation gates CR_j are realized by a rotated HWP, which is inserted only in one arm of the interferometer. Single-qubit phase gates V_k are achieved by tilting a glass plate GP inserted in one of the interferometer arms. The output states of photons are analyzed and detected with the help of wave plates, polarizing beam splitters PBS, and avalanche photodiodes APD.

In the experiment, we use an SPDC-based generator of photon pairs, which we described in Section 3.2.1. The quantum gate experimental setup is depicted in Fig. 4.3, and it consists of two crossed Mach-Zehnder interferometers (MZI) formed by calcite beam

displacers [2, 65]. The first MZI has a lateral separation of 4 mm, and the other has a separation of 6 mm.

Each photon from the pair carries two qubits encoded into its polarization and path degrees of freedom. The horizontal and vertical polarizations of the photon represent the computational states $|0\rangle$ and $|1\rangle$ of the polarization qubit, respectively. Similarly, propagation in the displaced and straight arm of a Mach-Zehnder interferometer represents computational states $|0\rangle$ and $|1\rangle$ of the path qubit.

The preparation of the hyperencoded qubits is described in Section 3.2.4, as well as its analysis and the realization of controlled gates operating on the hyperencoded qubits. The preparation of hyperencoded qubits involves disentangling the path-polarization entanglement using a controlled-waveplate operation ($CR_{1,2}$) set to implement CNOT gate. A half-wave plate addressing a single path implements such a gate, as we discussed earlier. Sometimes we need to apply another CNOT gate on the hyperencoded qubits. We use the freedom to set the controlled waveplate operation to embed the required controlled-waveplate operation into state preparation. The single-qubit unitary operations $U_{1,2}$ are also embedded into preparation to save resources. Similarly, gates $U_{3,4}$ and $R_{3,4}$ are embedded into state projection.

The C^3Z gate consists of three partially polarizing beam splitters (PPBS). The central $PPBS_1$ has the nominal transmittances $T_V = 1/3$, $T_H = 1$, and the other PPBSs have transmittances $T_V = 1$ and $T_H = 1/3$. The gate uses the same principle as its two-qubit variant [45–47], a conditional phase shift induced by a two-photon interference. The state of all qubits controls the phase shift because the two photons only interfere if they spatially overlap at $PPBS_1$ and have vertical polarization. Note that only nondisplaced paths overlap at the central PPBS. The displaced paths do not overlap at the PPBS due to the different lateral separation of the interferometric paths. Section 3.2.4 contains the explicit matrix form of the operator describing the action of the central PPBS on the two encoded qubits. $PPBS_2$ and $PPBS_3$ provide additional filtering to achieve uniform success probability 1/9 of gate operation for all input states.

Glass plates introduce interferometric phase shifts $V_{1,2}$. After the projection stage, a fiber collimator couples the photons into optical fibers, which guide them to the single-photon detectors, avalanche photodiodes in Geiger modes. The detector signals are processed electronically to realize measurement in coincidence basis, which we discussed in Sections 3.1.3 and 3.2.3.

4.2 Experimental characterization

As illustrated in Fig. 4.4, the four-qubit C^3Z gate, a central part of our linear optical quantum logic circuit, is equivalent to a four-qubit Toffoli gate up to local single-qubit Hadamard transforms on the target qubit. For each of the four choices of the target qubit, we have measured the truth table of the resulting Toffoli gate, which illustrates its performance in computational basis. The Hadamard transforms on the target qubit were implemented with the use of wave plates, which can be equivalently seen as probing the four-qubit

CZ gate with a product state consisting of three control qubits prepared in computational basis states $|0\rangle$, $|1\rangle$, and one target qubit prepared in the superposition basis state $|\pm\rangle = \frac{1}{\sqrt{2}}(|0\rangle \pm |1\rangle)$. At the output of the four-qubit C^3Z gate, the three control qubits are measured in the computational basis while the target qubit is measured in the superposition basis. The experimentally determined truth tables are shown in Fig. 4.4. The truth tables of all four Toffoli gates clearly show the expected bit flip of the target qubit conditional on all control qubits being prepared in the computational basis state $|1\rangle$.

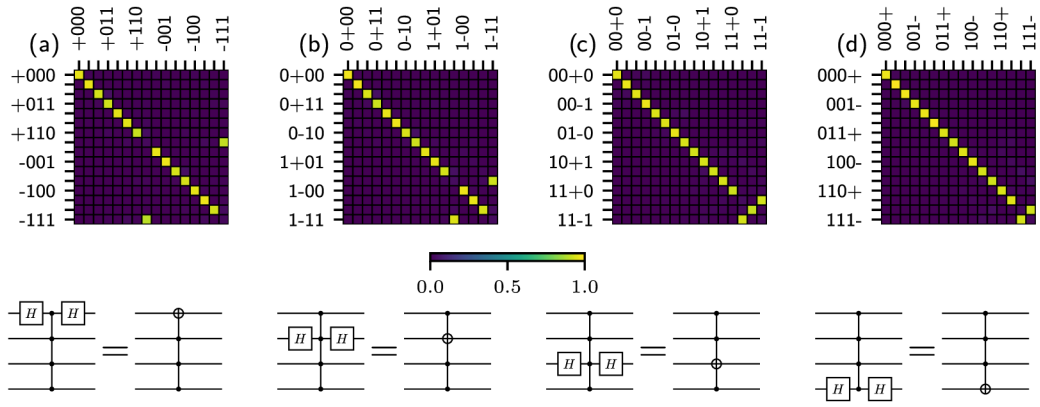

Figure 4.4: Experimentally determined truth tables of the four-qubit quantum Toffoli gates. The quantum logic circuits in each case indicate which qubit is the target qubit, and they also illustrate that each Toffoli gate is equivalent to a suitable combination of the C^3Z gate and two single-qubit Hadamard gates. The color bar is applicable for all subplots.

We now specify in more detail the quantities plotted in Fig. 4.4. Let $|\psi_j^m\rangle$ $(j = 0, \cdots, 15)$ denote the jth input four-qubit state when m-th qubit is the target qubit. The corresponding output state is given by $\rho_j^m = \mathcal{E}(|\psi_j^m\rangle\langle\psi_j^m|)$ where $\mathcal{E}$ is the four-qubit quantum operation actually implemented by our setup. Note that, due to various experimental imperfections, $\mathcal{E}$ can be a general trace-decreasing completely positive map. The output density matrices ρ_j^m are not normalized, and $p_j^m = \mathrm{Tr}(\rho_j^m)$ is the probability of success of the gate for a given input state $|\psi_j^m\rangle$. The truth tables depicted in Fig. 4.4 contain plots of the matrices f_{jk}^m of normalized overlaps of the actual output state ρ_j^m with the ideal output states $|\phi_k^m\rangle = U_{C^3Z}|\psi_k^m\rangle$ produced by the perfect gate,

$$f_{jk}^m = \frac{\langle\phi_k^m|\rho_j^m|\phi_k^m\rangle}{p_j^m}. \tag{4.2}$$

In particular, f_{jj}^m represents the output-state fidelity for input $|\psi_j^m\rangle$.

In the experiment, we measure the number of two-photon coincidences C_{jk}^m for all combinations of input state $|\psi_j^m\rangle$ and output projection onto $|\phi_k^m\rangle$. The measurement time is the same for all settings and set to 10 s. The normalized overlaps (4.2) are then estimated

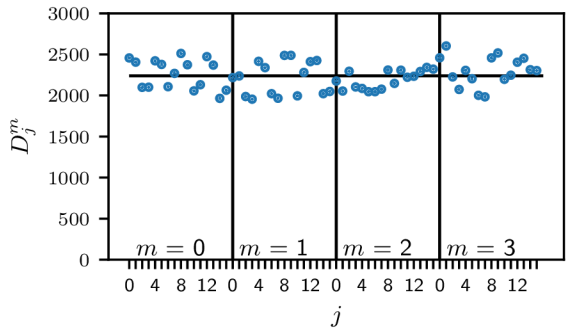

Figure 4.5: The total number of detected two-photon coincidences D_j^m is plotted for the 64 input states $|\psi_j^m\rangle$, which were utilized in the determination of the truth tables of the four-qubit Toffoli gates in Fig. 4.4.

from the experimental data according to [66]

$$f_{jk}^m = \frac{C_{jk}^m}{\sum_{l=0}^{15} C_{jl}^m}. \tag{4.3}$$

The success probabilities p_j^m should be constant and independent on the input state for perfect albeit probabilistic implementation of a unitary gate. To assess the behavior of p_j^m for our implementation, we plot in Fig. 4.5 the total number of detected two-photon coincidences $D_j^m = \sum_{l=0}^{15} C_{jl}^m$ for each of the 64 considered input states $|\psi_j^m\rangle$. The variations of D_j^m visible in the figure are partly caused by the Poissonian fluctuations of the number of emitted photon pairs. To compare the observed behavior of D_j^m with Poissonian statistics, we use the data plotted in Fig. 4.5 to estimate the variance V_D of D_j^m and compare it with the variance of a Poissonian distribution with the same mean number of coincidences $\bar{D}$. We obtain $\bar{D} = 2240$ and $V_D = 30338$. This corresponds to relative fluctuations of D_j^m of 8% while the corresponding relative Poissonian fluctuations would be about 2% (one relative standard deviation). This indicates that due to the various technical imperfections our implementation of the C^3Z gate introduces slight dependence of p_j^m on the input state.

The data contained in the truth tables plotted in Fig. 4.4 can be used to derive a lower bound and upper bound on the quantum process fidelity [139, 140] of the four-qubit C^3Z gate,

$$F_{C^3Z} = \frac{\mathrm{Tr}(\chi\chi_{C^3Z})}{\mathrm{Tr}(\chi)\mathrm{Tr}(\chi_{C^3Z})}. \tag{4.4}$$

Here χ and χ_{C^3Z} denote the Choi matrices [113, 114] of the implemented and the ideal C^3Z gate, respectively. The Choi matrix is calculated using Eq. (3.19). It holds that $\chi_{C^3Z} = |\chi_{C^3Z}\rangle\langle\chi_{C^3Z}|$, where

$$|\chi_{C^3Z}\rangle = \sum_{j=0}^{15} |\mathrm{b}j\rangle \otimes U_{C^3Z}|\mathrm{b}j\rangle \tag{4.5}$$

is a maximally entangled state of 8 qubits. For each choice of the target qubit m in Fig. 4.4, we define a weighted average state fidelity F_m as

$$F_m = \frac{\sum_{j=0}^{15} p_j^m f_{jj}^m}{\sum_{k=0}^{15} p_k^m}. \tag{4.6}$$

The four average state fidelities F_m determined from the truth tables of the four-qubit Toffoli gates and plotted in Fig. 4.4 yield the following generalized Hofmann lower and upper bounds [22, 66] on the fidelity of the C^3Z gate,

$$F_1 + F_2 + F_3 + F_4 - 3 \leq F_{C^3Z} \leq \min_m F_m. \tag{4.7}$$

The experimentally determined average state fidelities read $F_1 = 0.943(1)$, $F_2 = 0.952(1)$, $F_3 = 0.944(1)$, and $F_4 = 0.955(1)$, which documents the good performance of the gate. The statistical uncertainties of the fidelity estimates were obtained by error propagation, assuming Poissonian statistics of the measured coincidence counts. If we insert these data into Eq. (4.7), we get $0.794(2) \leq F_{C^3Z} \leq 0.943(1)$. An experimentally appealing property of these fidelity bounds is that they can be determined by measuring fidelities of multiqubit output product states obtained from input product states. Therefore, neither preparation of entangled states nor measurements in an entangled basis are required. However, the resulting lower bound on F_{C^3Z} is rather loose.

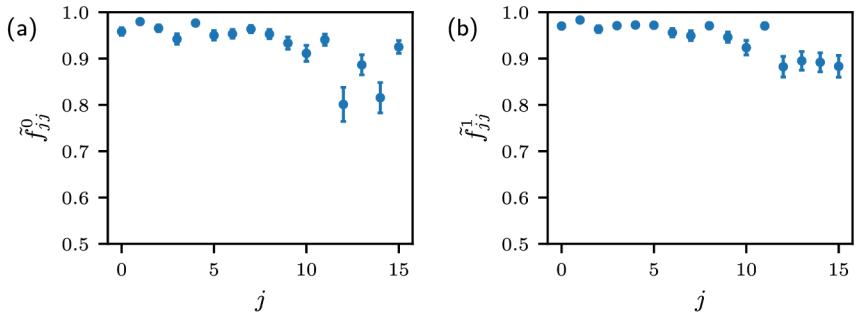

Figure 4.6: Experimental output state fidelities $\tilde{f}_{jj}^m$ for input states forming two mutually unbiased bases. Each input state is a product state with two qubits prepared in the computational basis states and the other two qubits prepared in the superposition states $|\pm\rangle$. In panel (a), the qubits 1 and 2 were prepared in the superposition $|\pm\rangle$, while in panel (b) the qubits 3 and 4 were prepared in superposition.

To obtain a better and tighter lower bound on F_{C^3Z}, we have experimentally determined the original Hofmann fidelity bound [22], which is given by average state fidelities $\tilde{F}_1$ and $\tilde{F}_2$ for two mutually unbiased bases. In particular, it holds that

$$\tilde{F}_1 + \tilde{F}_2 - 1 \leq F_{C^3Z} \leq \min(\tilde{F}_1, \tilde{F}_2). \tag{4.8}$$

In our experiment, we construct the two mutually unbiased basis by preparing the polarization and path qubits of one photon in the computational basis states $|0\rangle$, $|1\rangle$ and the

polarization and path qubits of the other photon in superposition basis states $|\pm\rangle$. The average state fidelities $\tilde{F}_m$ are defined similarly as F_m. However, the determination of the corresponding output state fidelities $\tilde{f}_{jj}^m$ now requires measurements in entangled basis, because C^3Z gate maps some of the input states onto entangled output states. For instance,

$$U_{C^3Z}|1\rangle|1\rangle|+\rangle|+\rangle = \frac{1}{\sqrt{2}}|1\rangle|1\rangle(|0\rangle|+\rangle + |1\rangle|-\rangle). \tag{4.9}$$

Fortunately, the output state fidelities $\tilde{f}_{jj}^m$ can be directly measured with our quantum logic circuit, because we can set the two controlled-rotation gates CR_3 and CR_4 in Fig. 4.3 to CNOT gates and perform measurements in the basis of maximally entangled Bell states. The experimentally determined output state fidelities $\tilde{f}_{jj}^m$ are plotted in Fig. 4.6 and the resulting average state fidelities read $\tilde{F}_1 = 0.944(4)$ and $\tilde{F}_2 = 0.928(4)$. Consequently, we obtain the following bounds on the fidelity of the C^3Z gate,

$$0.872(6) \leq F_{C^3Z} \leq 0.928(4) \tag{4.10}$$

With a rather small number of measurements, we have thus successfully confirmed the high-quality performance of our multiqubit quantum logic circuit and we have constrained the fidelity of the four-qubit quantum controlled-Z gate into a narrow interval.

4.3 Preparation of four-qubit entangled state

We next investigate the ability of the C^3Z gate to generate genuine multipartite entangled states from input product states. Specifically, we consider the input state $|+\rangle^{\otimes 4}$, which is transformed by the C^3Z gate into an entangled state that belongs to the family of four-qubit GHZ states,

$$|\Psi_{4+}\rangle = U_{C^3Z}\left(|+\rangle^{\otimes 4}\right) = |+\rangle^{\otimes 4} - \frac{1}{2}|1\rangle^{\otimes 4}. \tag{4.11}$$

We have performed a tomographically overcomplete set of measurements on the generated four-qubit state and we have reconstructed its density matrix ρ'_+ from the experimental data using the maximum likelihood estimation procedure [112, 115], see Section 3.1.4 for a detailed description. The resulting density matrix is plotted in Fig. 4.7. We can characterize the generated entangled state by its purity P_+ and fidelity $F_+ = \langle\Psi_{4+}|\rho'_+|\Psi_{4+}\rangle$. Using the experimentally determined ρ'_+ we obtain $F'_+ = 0.927(2)$ and $P_+ = 0.931(2)$, which demonstrates the high quality of the generated state. We applied local phase shifts on the reconstructed state to maximize the fidelity to $F_+ = 0.942(2)$. The phase shifts could be in principle also applied experimentally by embedding them in analysis, as we described in Section 3.2.5. From now we will work with the phase-corrected density matrix ρ_+.

To certify that the experimentally prepared four-qubit state exhibits genuine multipartite entanglement, we utilize a suitable entanglement witness [123, 141, 142]. We recall that a multipartite quantum state exhibits a genuine multipartite entanglement if it cannot be written as a mixture of biseparable states. Consider first a maximally entangled

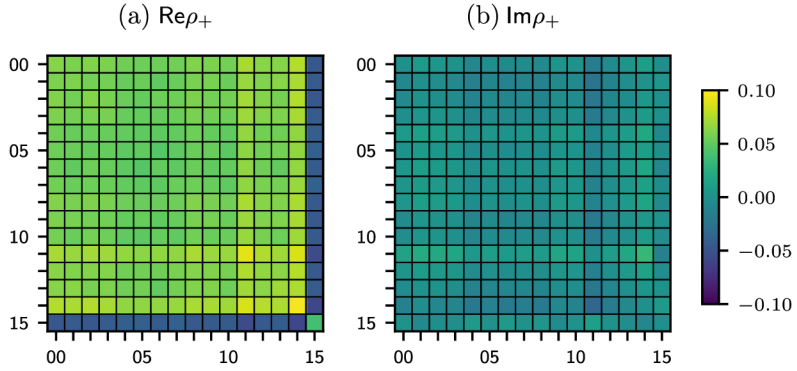

Figure 4.7: Real (a) and imaginary (b) part of the density matrix ρ_+ of an entangled four-qubit state which was generated by the quantum C^3Z gate from a product state $|++++\rangle$. The color bar is shared.

GHZ state

$$|\mathrm{GHZ}_\phi\rangle = \frac{1}{\sqrt{2}}(|\phi\rangle^{\otimes 4} - |\phi_\perp\rangle^{\otimes 4}), \tag{4.12}$$

where $|\phi\rangle = \cos\phi|0\rangle + \sin\phi|1\rangle$ and $|\phi_\perp\rangle = \sin\phi|0\rangle - \cos\phi|1\rangle$ denote two orthogonal single-qubit states. An optimal projector entanglement witness [124, 143] for the state (4.12) is given by

$$W_{\mathrm{GHZ}} = \frac{1}{2}\mathbb{1}_{16} - |\mathrm{GHZ}_\phi\rangle\langle\mathrm{GHZ}_\phi|. \tag{4.13}$$

A genuine four-partite entanglement of a state ρ is certified when $\mathrm{Tr}(W_{\mathrm{GHZ}}\rho) < 0$, i.e., when the fidelity of the state with the maximally entangled GHZ state (4.12) exceeds $\frac{1}{2}$. The overlap

$$\left|\langle\mathrm{GHZ}_\phi|\Psi_{4+}\rangle\right|^2 = \frac{1}{8}\left[2\sin(2\phi) + \cos(2\phi)\right]^2 \tag{4.14}$$

is maximized for $\phi = \frac{1}{2}\arctan(2) \approx 0.554$, and at this point $\langle\Psi_{4+}|W_{\mathrm{GHZ}}|\Psi_{4+}\rangle = -1/8$. This shows that the standard GHZ witness (4.13) is capable of detecting multipartite entanglement of the four-qubit state $|\Psi_{4+}\rangle$. For the experimentally determined state ρ_+, we find that the witness is minimized at $\phi_{\mathrm{exp}} = 0.585$, in excellent agreement with theoretical expectations. At this optimal point, we get $\langle W_{\mathrm{GHZ}}\rangle = -0.112(2)$ which confirms that the experimentally generated state exhibits genuine multipartite entanglement.

To complete our analysis, we also present two alternative constructions of witnesses which can detect multipartite entanglement of the state $|\Psi_{4+}\rangle$. Our first construction is based on the observation that the four-qubit state $|\Psi_{4+}\rangle$ can be transformed onto the canonical GHZ state $|\mathrm{GHZ}_0\rangle = \frac{1}{\sqrt{2}}(|0000\rangle - |1111\rangle)$ by local single-qubit operations. In particular, we have

$$g^{\otimes 4}|\Psi_{4+}\rangle = \frac{1}{4\sqrt{2}}|\mathrm{GHZ}_0\rangle, \tag{4.15}$$

where

$$g = \frac{1}{2^{1/4}}|0\rangle\langle 0| + |1\rangle\langle -| \tag{4.16}$$

	W_{GHZ}	W_{filter}	W_{proj}
$\langle W\rangle$	$-0.112(2)$	$-0.0146(3)$	$-0.067(2)$
$\mathcal{S}$	53	49	44
$p_{\max}$	$\frac{2}{9}\approx 0.222$	$\frac{1}{(2^{1/4}+1)^4-2}\approx 0.048$	$\frac{2}{15}\approx 0.133$

Table 4.1: Properties of the three entanglement witnesses used to detect genuine multipartite entanglement of the four-qubit state $|\Psi_{4+}\rangle$. For each witness, the table displays its experimental mean value $\langle W\rangle$, the significance of the entanglement test $\mathcal{S}$, and the maximum tolerable fraction of white noise $p_{\max}$. For details, see text.

denotes a single-qubit quantum filter. Since local single-qubit quantum filters map biseparable states onto biseparable states, a filtered state $\tilde{\rho} = G\rho G^\dagger/\mathrm{Tr}(G\rho G^\dagger)$, where $G = g^{\otimes 4}$, exhibits genuine multipartite entanglement only if the original state ρ also exhibits genuine multipartite entanglement. Starting from the optimal witness (4.13) for the canonical GHZ state $|\mathrm{GHZ}_0\rangle$, and considering its application to the filtered state $\tilde{\rho}$, we arrive at the following witness for the original state ρ,

$$W_{\mathrm{filter}} = \frac{1}{2}G^\dagger G - G^\dagger|\mathrm{GHZ}_0\rangle\langle\mathrm{GHZ}_0|G. \tag{4.17}$$

For the experimentally generated four-qubit state ρ_+ we get $\langle W_{\mathrm{filter}}\rangle = -0.0146(3)$, while for the ideal pure state (4.11) one has $\langle\Psi_{4+}|W_G|\Psi_{4+}\rangle = \frac{1}{64}\approx -0.0156$.

In our second approach, we utilize a projector witness of the form

$$W_{\mathrm{proj}} = \alpha\mathbb{1}_{16} - |\Psi_{4+}\rangle\langle\Psi_{4+}|. \tag{4.18}$$

To optimize the witness (4.18), the coefficient α should be equal to the maximum overlap of the state $|\Psi_{4+}\rangle$ with a biseparable state. Since the set of biseparable states is convex and the state $|\Psi_{4+}\rangle$ is invariant with respect to permutations of qubits, it suffices to maximize the overlap with pure biseparable states $|\sigma\rangle_1|\omega\rangle_{234}$ and $|\Sigma\rangle_{12}|\Omega\rangle_{34}$. Here the subscripts label the four qubits, so for instance $|\sigma\rangle_1$ is a single-qubit state and $|\Sigma\rangle_{12}$ is a two-qubit state. We parameterize these two states explicitly,

$$|\sigma\rangle = a_0|0\rangle + a_1|1\rangle, \qquad |\Sigma\rangle = b_{00}|00\rangle + b_{01}|01\rangle + b_{10}|10\rangle + b_{11}|11\rangle, \tag{4.19}$$

with the normalization conditions $|a_0|^2 + |a_1|^2 = 1$ and $\sum_{j,k=0}^{1}|b_{jk}|^2 = 1$. It holds that

$$\begin{aligned}&\max_{\sigma,\omega}(|{}_1\langle\sigma|_{234}\langle\omega|\Psi_{4+}\rangle|^2) = \max_\sigma\langle\Psi_{4+}|(|\sigma\rangle\langle\sigma|_1\otimes\mathbb{1}_8)|\Psi_{4+}\rangle]\\ &= \max_{a_0,a_1}\left[\frac{1}{2}+\frac{3}{8}(a_0a_1^* + a_0^*a_1)\right] = \frac{7}{8}.\end{aligned} \tag{4.20}$$

Since $|\Psi_{4+}\rangle$ is entangled, it suffices to optimize over parameters of one subsystem only. The other part is after the projection pure and its projection probability can always be maximized to 1.

The maximization of $|{}_{12}\langle\Sigma|_{34}\langle\Omega|\Psi_{4+}\rangle|^2$ can be performed in a similar manner. We find that the optimal state $|\Sigma\rangle_{12}$ reads

$$|\Sigma_{\mathrm{opt}}\rangle = x(|00\rangle + |01\rangle + |10\rangle) + \sqrt{1-3x^2}|11\rangle \tag{4.21}$$

and the maximization of the overlap amounts to the maximization of the function

$$f(x) = \frac{1}{4}\left(1 + 3x\sqrt{1-3x^2} + 6x^2\right). \tag{4.22}$$

The maximum is achieved at $x = \sqrt{\frac{1}{6} + \frac{1}{3\sqrt{7}}}$ and we arrive at

$$\max_{\Sigma,\Omega} |_{12}\langle\Sigma|_{34}\langle\Omega|\Psi_{4+}\rangle|^2 = \frac{1}{8}(4+\sqrt{7}) \approx 0.8307. \tag{4.23}$$

We thus find that $\alpha = \frac{7}{8}$ and the optimal projector witness for the state $|\Psi_{4+}\rangle$ reads $W_{\text{proj}} = \frac{7}{8}I - |\Psi_{4+}\rangle\langle\Psi_{4+}|$. For the experimentally reconstructed state we obtain $\langle W_{\text{proj}}\rangle = -0.067(2)$.

A comparison of the three above discussed entanglement witnesses is provided in Tab. 4.1. Besides the mean values of the three witnesses, the table also shows the significance of the entanglement test [144] defined as $\mathcal{S} = -\langle W\rangle/\Delta W$, where ΔW is the standard deviation quantifying statistical uncertainty of $\langle W\rangle$. Moreover, the table also displays the maximum tolerable fraction of the white noise $p_{\max}$ for which the witness still detects entanglement of a mixed state

$$(1-p)|\Psi_{4+}\rangle\langle\Psi_{4+}| + \frac{p}{16}\mathbb{1}_{16}.$$

We can see that W_{GHZ} is the optimal witness as it achieves the highest significance $\mathcal{S}$ and also it can tolerate more white noise than the other two witnesses.

4.4 Monte-Carlo sampling of quantum gate fidelity

The four-qubit quantum C^3Z gate represents an interesting nontrivial device for testing techniques devised for efficient characterization of multiqubit quantum operations [2, 17, 18, 23–26, 145, 146]. The Hofmann bound [22] utilized in the previous part can be considered as an example of an efficient partial characterization technique, but it should be noted that the number of measurement settings required for the determination of the Hofmann bounds still scales exponentially with the number of qubits N. This exponential bottleneck can be avoided by the Monte Carlo sampling of quantum gate fidelity [2, 24–26]. The main feature of this technique is that the number of measurement settings depends on the required uncertainty of the fidelity estimate but not on the dimension of the Hilbert space.

Here we apply the Monte Carlo sampling to determine the fidelity of the four-qubit quantum C^3Z gate given by Eq. (4.4). The first step is to express the quantum process matrix χ_{C^3Z} of the ideal C^3Z gate as a linear combination of 8-fold tensor products of single-qubit Pauli operators $\sigma_1 = \sigma_x$, $\sigma_2 = \sigma_y$, $\sigma_3 = \sigma_z$, and $\sigma_0 = \mathbb{1}_2$. The expansion is

$$\chi_{C^3Z} = \sum_{j=0}^{4^8-1} a_j \Sigma_j, \tag{4.24}$$

where a_j are real constants, and

$$\Sigma_j = \sigma_{j_7} \otimes \cdots \otimes \sigma_{j_0} \tag{4.25}$$

is the 8-fold Kronecker product of Pauli operators. The relation between the integer j and the labels j_k is

$$j = \sum_{k=0}^{7} 4^k j_k.$$

In other words, j_k is the k-th digit of the base-4 representation of j. Coefficients a_j are determined as $a_j = \frac{1}{2^8}\mathrm{Tr}(\chi_{C3Z}\Sigma_j)$. We find that the expansion contains altogether 1936 nonzero coefficients a_j.

Since in our experiment we sequentially probe the quantum gate by various input states, we rewrite the expansion (4.24) as a linear combination of projectors onto pure product states. For this purpose, we express each of the three Pauli matrices $\sigma_{1,2,3}$ as a difference of projectors onto their $+1$ and -1 eigenstates, and similarly, we explicitly write $\sigma_0 = |0\rangle\langle 0| + |1\rangle\langle 1|$. After some algebra, we arrive at the expansion

$$\chi_{C^3Z} = \sum_{k=0}^{N_+-1} b_k^+ \Pi_k^+ - \sum_{k=0}^{N_--1} b_k^- \Pi_k^-, \tag{4.26}$$

where b_k^+ and b_k^- are positive coefficients,

$$\Pi_k^\pm = \pi_{k_7}^\pm \otimes \cdots \otimes \pi_{k_0}^\pm, \tag{4.27}$$

and operators $\pi_{k_n}^+$ and $\pi_{k_n}^-$ are projectors onto eigenstates of σ_{k_n}. The total number of terms in the expansion (4.26) reads $N_+ = 22416$ and $N_- = 22400$.

As a final preparatory step, we introduce two probability distributions

$$p_k^+ = \frac{b_k^+}{B_+}, \qquad p_k^- = \frac{b_k^-}{B_-}, \tag{4.28}$$

where

$$B_+ = \sum_{k=0}^{N_+-1} b_k^+, \qquad B_- = \sum_{k=0}^{N_--1} b_k^-. \tag{4.29}$$

The Monte Carlo sampling proceeds as follows. We randomly generate a list of M_+ labels c_m in the range $[0, N_+ - 1]$ drawn from the distribution p_k^+, and we also generate a list of M_- labels d_m in the range $[0, N_- - 1]$ drawn from the distribution p_k^-. Next, we experimentally determine the mean values of the randomly chosen projectors $\Pi_{c_m}^+$ and $\Pi_{d_m}^-$,

$$\langle \Pi_{c_m}^+ \rangle = \mathrm{Tr}(\chi \Pi_{c_m}^+), \qquad \langle \Pi_{d_m}^+ \rangle = \mathrm{Tr}(\chi \Pi_{d_m}^-). \tag{4.30}$$

Practically, each of these terms can be measured by preparing a suitable four-qubit input product state and by performing a projection onto a suitable four-qubit product state at

the output. The count of detected coincidences is $np_s\mathrm{Tr}(\chi\Pi^{\pm}_{c_m})$, where n is the total number of photon pairs used in the particular measurement (a product of generation rate and integration time) and p_s is the success probability of the gate. To determine $\mathrm{Tr}(\chi\Pi^{\pm}_{c_m})$ we normalize the measured counts with the normalization factor $S/16$, where S is the sum of all counts in the reference computational basis truth table. Factor $S/16$ estimates the value $\langle np_s\rangle$.

The gate fidelity is then estimated according to the formula

$$F_{\mathrm{MC}} = \frac{1}{\mathrm{Tr}[\chi]\mathrm{Tr}[\chi_{\mathrm{C^3Z}}]}\left(\frac{B_+}{M_+}\sum_{m=0}^{M_+-1}\langle\Pi^+_{c_m}\rangle - \frac{B_-}{M_-}\sum_{m=0}^{M_--1}\langle\Pi^-_{d_m}\rangle\right), \tag{4.31}$$

where $\mathrm{Tr}[\chi_{\mathrm{C^3Z}}] = \mathrm{Tr}[\chi] = 16$.

To assess the systematic error of gate fidelity estimation due to the finite number of samples M_+ and M_-, we assume perfect gate implementation, $\chi = \chi_{\mathrm{C^3Z}}$, and neglect the statistical uncertainty of $\langle\Pi^+_{c_m}\rangle$ and $\langle\Pi^-_{d_m}\rangle$. The systematic error of fidelity estimation due to a finite number of samples can then be expressed as

$$\langle(\Delta F_{\mathrm{MC}})^2\rangle = \frac{1}{16^4}\left(\frac{B_+^2}{M_+}V_+ + \frac{B_-^2}{M_-}V_-\right), \tag{4.32}$$

where

$$V_+ = \sum_{k=0}^{N_+-1} p_k^+\left[\mathrm{Tr}(\chi_{\mathrm{C^3Z}}\Pi_k^+)\right]^2 - \left[\sum_{k=0}^{N_+-1} p_k^+\mathrm{Tr}(\chi_{\mathrm{C^3Z}}\Pi_k^+)\right]^2, \tag{4.33}$$

and V_- is defined similarly. For a fixed total number of samples $M_T = M_+ + M_-$, we can minimize the systematic error (4.32) by optimizing the number of samples M_+ and M_-. This yields

$$M_\pm = M_T\frac{B_\pm\sqrt{V_\pm}}{B_+\sqrt{V_+} + B_-\sqrt{V_-}}. \tag{4.34}$$

On inserting these optimal values back into Eq. (4.32) we obtain

$$\langle(\Delta F)^2\rangle_{\min} = \frac{1}{16^4}\frac{1}{M_T}\left(B_+\sqrt{V_+} + B_-\sqrt{V_-}\right)^2. \tag{4.35}$$

Numerically, we get

$$M_+ \approx 0.891M_T, \qquad M_- \approx 0.089M_T, \tag{4.36}$$

and

$$\langle(\Delta F_{\mathrm{MC}})^2\rangle_{\min} \approx \frac{2.496}{M_T}. \tag{4.37}$$

This indicates that the optimal sampling strategy is strongly unbalanced, with almost 90% of samples used to estimate the positive terms in the expansion (4.26) and only about 10% of samples is allocated to estimate the negative terms in that expansion. Formula (4.37) provides an explicit quantification of the systematic error of the Monte Carlo sampling procedure. To reduce the sampling error below 1% (as quantified by one standard deviation

$\sqrt{\langle(\Delta F_{\mathrm{MC}})^2\rangle}$), at least 2.5×10^4 samples are required, which is comparable with the total number of terms N_+ and N_- in the expansion (4.26).

We have experimentally probed the performance of the Monte Carlo sampling procedure for our linear optical four-qubit quantum gate. We have generated the random list of $M_T = 1100$ measurement settings, measured the number of coincidences for a fixed time interval for all these settings, and we have also performed the measurements in the computational basis required for normalization. We have determined the mean values (4.30) from these data and obtained an estimate of the gate fidelity F_{MC}. We have repeated this procedure 15 times, and the resulting fidelity estimates are plotted in Fig. 4.8. We characterize the ensemble of fidelity estimates by its mean $\bar{F}_{\mathrm{MC}} = 0.912$ and standard deviation $\Delta F_{\mathrm{MC}} = 0.042$. This is consistent with the systematic error 0.048 predicted by formula (4.37) and the statistical error 0.011 due to Poissonian statistics of the coincidence events. The mean fidelity $\bar{F}_{\mathrm{MC}}$ is in excellent agreement with the lower (0.872) and upper (0.928) Hofmann bounds (4.10). The uncertainty of $\bar{F}_{MC}$ can be estimated as $\Delta F_{\mathrm{MC}}/\sqrt{K-1} \approx 0.011$, where $K = 15$ is the number of repetitions of the Monte Carlo sampling procedure.

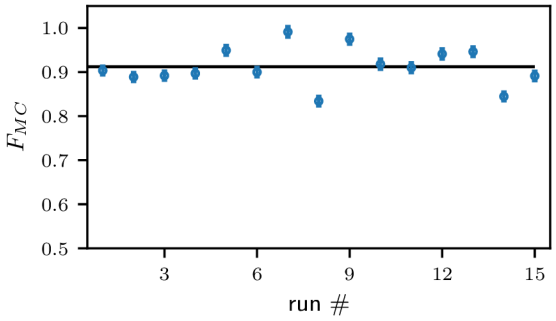

Figure 4.8: Monte Carlo estimates F_{MC} of fidelity of the experimentally implemented C^3Z gate. Each estimate was obtained from $M_T = 1100$ samples and the whole sampling procedure was independently repeated 15 times to obtain an ensemble of fidelities. The error bars indicate statistical errors due to a finite number of two-photon coincidence counts.

We used the 16 500 measured projections to reconstruct the implemented quantum process using the maximum likelihood estimation procedure. The set of the used measurements is tomographically incomplete and it is not guaranteed that the reconstruction converges to a true process matrix. Multiple processes could maximize the likelihood of observing the measured tomogram. In that case, starting the reconstruction from various initial operators should yield different results. However, sometimes even tomographically incomplete measurement could lead to a correct reconstruction, provided we choose the suitable measurements for the investigated process. We tested the reconstruction convergence by reconstructing the process matrix repeatedly with a randomly varying initial operator. In total, we tried 20 random initial operators. For each pair of the resulting process matrices, we calculated the respective fidelity F_r. The mean infidelity $1 - \bar{F}_r$ be-

tween the reconstructions was $5 \cdot 10^{-5}$. It means that regardless of the initial operator, the reconstruction always converges to the same process. Albeit the measurements were not generally tomographically complete, the data characterize the specific realized quantum process well. This is probably the consequence of relatively high process purity and a good prior assumption about the measured quantum process that led to selecting measurements for the Monte Carlo sampling method. The mean fidelity of the reconstructed process matrices to the ideal C^3Z process matrix was $F_{C^3Z} = 0.914$. This fidelity lies within the previously estimated bounds.

4.5 Decoherence-resilient CZ gate

As an application, we use the C^3Z gate to implement a controlled-Z gate acting on two logical qubits which is resilient to *collective dephasing*. Each logical qubit is carried by two physical qubits. We experimentally confirm the faithful implementation of the two-qubit entangling operation insensitive to collective decoherence.

The dephasing operation $\mathcal{D}_q$ acting on a single-qubit density matrix ρ is a completely positive map,

$$\mathcal{D}_q(\rho) = q\rho + (1-q)\sigma_z\rho\sigma_z, \tag{4.38}$$

The dephasing $\mathcal{D}_q$ succinctly describes the effect of random phase fluctuations. Any transformation

$$\rho \to \int_{-\pi}^{\pi} V(\varphi)\rho V^\dagger(\varphi)p(\varphi)\mathrm{d}\varphi, \tag{4.39}$$

where $p(\varphi)$ is a symmetric probability density, $p(-\varphi) = p(\varphi)$, and $V(\varphi) = |0\rangle\langle 0| + e^{i\varphi}|1\rangle\langle 1|$ can be represented by map $\mathcal{D}_q$ with $q = \frac{1}{2} + \int_0^\pi p(\varphi)\cos(\varphi)\mathrm{d}\varphi$. In some quantum systems, the dephasing can be caused, for example, by fluctuating classical fields or by interaction with the environment which introduces correlations between computational basis states of the system qubit and the environment,

$$|0\rangle|E_{\mathrm{in}}\rangle \to |0\rangle|E_0\rangle, \quad |1\rangle|E_{\mathrm{in}}\rangle \to |1\rangle|E_1\rangle. \tag{4.40}$$

In the latter case $q = \frac{1}{2}(1 + |\langle E_0|E_1\rangle|)$.

Consider the situation when the dephasing introduces the same random phase shifts to both qubits. Mathematically, the operation acting on the two-qubit state is a mixture of unitary operations $V(\varphi) \otimes V(\varphi)$. A two-dimensional decoherence-free-subspace spanned by the product states $|0_L\rangle = |0\rangle|1\rangle$ and $|1_L\rangle = |1\rangle|0\rangle$ is unaffected by such collective dephasing because

$$V(\varphi) \otimes V(\varphi)(\alpha|0\rangle|1\rangle + \beta|1\rangle|0\rangle) = e^{i\varphi}(\alpha|0\rangle|1\rangle + \beta|1\rangle|0\rangle). \tag{4.41}$$

Therefore the logical qubit state $\alpha|0_L\rangle + \beta|1_L\rangle$ is protected and the overall phase shift $e^{i\varphi}$ becomes physically irrelevant.

Let us label the physical qubits with capital letters, with the first logical qubit encoded in physical qubits A and C, and the second logical qubit encoded in physical qubits B

and D. The controlled-Z gate can be implemented by applying a two-qubit gate $U_{\mathrm{CZ}} = \exp(i\pi|11\rangle\langle 11|)$ to the first physical qubit of each logical qubit [147], see Fig. 4.9 (a). Here, we consider an alternative approach based on a quantum gate acting on all four physical qubits, see Fig. 4.9 (b),

$$W = e^{i\pi|1_L 1_L\rangle\langle 1_L 1_L|} = e^{i\pi|1010\rangle\langle 1010|}. \tag{4.42}$$

Up to local σ_x operations, this transformation is equivalent to the implemented C^3Z gate. In publication [A2] we theoretically illustrate that for certain kinds of errors and imperfections, it may be advantageous to utilize such four-qubit gates, provided they are available, instead of two-qubit gates, when implementing operations on encoded logical qubits.

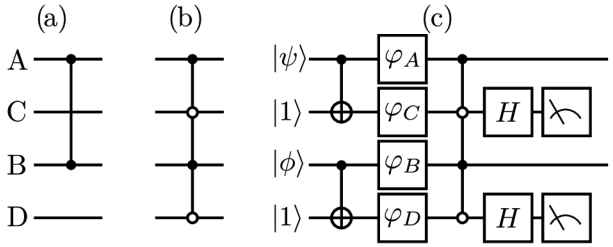

Figure 4.9: a) two-qubit CZ gate acting between qubits AB acts as a CZ between logical qubits AC, BD, b) four-qubit W gate, c) experimentally implemented quantum logic circuit.

We now proceed to the experimental test of implementation of the CZ gate on logical qubits via a four-qubit gate W acting on physical qubits. At the input, the qubits A and B encode the quantum information and are prepared in pure states $|\psi\rangle_A$ and $|\phi\rangle_B$, respectively. Two additional ancilla qubits C and D are prepared in state $|1\rangle$. Two quantum CNOT gates, implemented with controlled-rotation gates CR_1 and CR_2, depicted in Fig. 4.3, serve for encoding the information into logical qubits supported by pair of physical qubits. For instance, $(\alpha|0\rangle_A + \beta|1\rangle_A)|1\rangle_C \rightarrow \alpha|01\rangle_{AC} + \beta|10\rangle_{AC}$. Dephasing is imposed by single-qubit phase shift gates acting on each qubit. Collective dephasing occurs when the phase shifts applied to A and C (or B and D) are always identical, as indicated in the figure. Entangling CZ gate on logical qubits is implemented via a four-qubit gate W on the physical qubits. Subsequently, we decode the logical qubits back to single physical qubits by performing measurements in the superposition basis $|\pm\rangle = \frac{1}{\sqrt{2}}(|0\rangle \pm |1\rangle)$ on qubits C and D. This quantum erasing directly maps the state of a logical qubit onto a physical qubit if the measurement result reads $|+\rangle$. In case of result $|-\rangle$ a compensating phase flip operation σ_z has to be applied to the physical qubit, which can be deterministically accomplished by a feedforward operation [148–153].

In our tests, the qubits A and C are hyperencoded to signal photon and qubits B and D are hyperencoded to the idler photon. The single-qubit phase shifts can be implemented via suitable combinations of waveplates. To make our experimental implementation more efficient, we combine together the random phase shifts with state preparation or measurement basis selection, which reduces the number of required wave plates in the experimental setup.

We characterize the generated two-qubit and four-qubit quantum states tomographically starting by checking the action of the four-qubit W gate on input logical qubits prepared in superposition states. In this case, the four-qubit unitary operation W should produce a maximally entangled state of the two logical qubits. At the level of physical qubits, the inputs correspond to products of Bell states $|\Psi^{\pm}\rangle = \frac{1}{\sqrt{2}}(|01\rangle \pm |10\rangle)$, see Table 4.2. As an example, consider the input state $|\Psi_{\text{in}}\rangle = |\Psi^{+}\rangle|\Psi^{+}\rangle$. The corresponding output state of the four physical qubits reads

$$|\Psi_{\text{out}}\rangle = \frac{1}{2}(|0101\rangle + |1001\rangle + |0110\rangle - |1010\rangle). \tag{4.43}$$

We plot the density matrix of the output state reconstructed from the experimental data in Fig. 4.10 together with the theoretical density matrix of the ideal output pure state $|\Psi_{\text{out}}\rangle\langle\Psi_{\text{out}}|$. A clear agreement between the theory and experiment can be seen. We characterize the quality of the output four-qubit states ρ by their purity and fidelity to the ideal output state $|\Psi_{\text{out}}\rangle$. The data are listed in Table 4.2 and we can see that fidelity typically exceeding 90% is achieved. The fidelity can be further improved if we compensate for residual single-qubit phase shifts, see column F_{opt} in Table 4.2. The statistical errors indicated in the table were estimated from the measured two-photon coincidence counts assuming their Poissonian statistics and using the bootstrapping method (see Section 3.1.6) with 1000 samples.

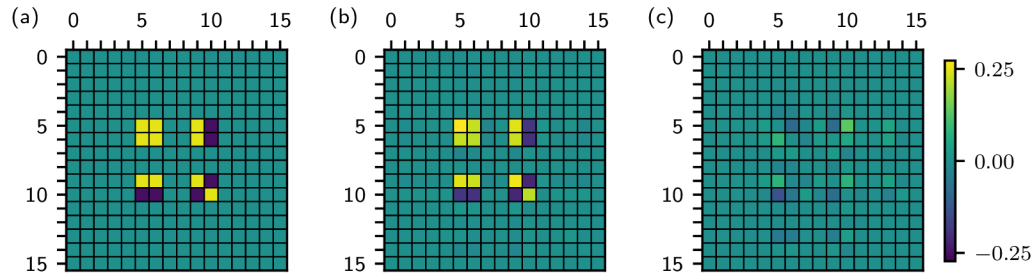

Figure 4.10: Theoretical and experimental density matrix of a four-qubit state produced from input state $|\Psi^{+}\rangle|\Psi^{+}\rangle$ by the linear optical quantum gate W. The real part of the theoretical density matrix is shown in panel (a), its imaginary part is zero. Panels (b) and (c) contain the real and imaginary parts of the experimentally reconstructed density matrix, respectively. All the nonzero density matrix elements of ρ_{th} have absolute value 0.25 and the maximum difference between matrix elements of ρ_{th} and ρ_{exp} reads $\max_{jk} \Delta\rho_{jk} = 0.149$. The color bar is shared by all matrix plots.

After checking the performance of our quantum logic circuit we proceed with the main experimental test of the dephasing resilience, depicted in Fig. 4.9. We choose to test the gate for input superposition state $|+_L\rangle|+_L\rangle$ since this state is most sensitive to dephasing. We consider full dephasing, $q = 1/2$, which is modeled as a balanced mixture of identity operation and phase flip σ_z. Collective dephasing means that the phase shifts on two qubits (A and C, or B and D) are identical, $\phi_A = \phi_C$ and $\phi_B = \phi_D$, respectively. We consider the

$\lvert\Psi_{\text{in}}\rangle$	F	F_{opt}	$\mathcal{P}$
$\lvert+_L\rangle\lvert+_L\rangle = \lvert\Psi^+\rangle_{AC}\lvert\Psi^+\rangle_{BD}$	0.890(5)	0.936(5)	0.918(9)
$\lvert+_L\rangle\lvert-_L\rangle = \lvert\Psi^+\rangle_{AC}\lvert\Psi^-\rangle_{BD}$	0.937(4)	0.942(4)	0.930(7)
$\lvert-_L\rangle\lvert+_L\rangle = \lvert\Psi^-\rangle_{AC}\lvert\Psi^+\rangle_{BD}$	0.924(4)	0.934(4)	0.923(8)
$\lvert-_L\rangle\lvert-_L\rangle = \lvert\Psi^-\rangle_{AC}\lvert\Psi^-\rangle_{BD}$	0.932(4)	0.938(4)	0.928(8)

Table 4.2: Parameters of four-qubit output states generated from input superposition states by the linear optical circuit that implements the four-qubit entangling gate W. The table shows fidelity F of the experimental state with the ideal theoretical state, purity of the output state $\mathcal{P}$ and fidelity F_{opt} optimized by using compensating single-qubit phase shifts that were determined from the tomographically reconstructed four-qubit density matrices. Numbers in parentheses represent one standard deviation.

dephasing of one pair of physical qubits, and also the independent dephasing of both pairs of physical qubits. For instance, in the case of collective dephasing on both pairs of qubits, the experimentally recorded two-photon coincidences combine data corresponding to four different phase shifts: $\phi_A = 0$ and $\phi_B = 0$, $\phi_A = \pi$ and $\phi_B = 0$, $\phi_A = 0$ and $\phi_B = \pi$, $\phi_A = \pi$ and $\phi_B = \pi$. In all cases, $\phi_A = \phi_C$ and $\phi_B = \phi_D$ holds.

We used the time multiplexing described in Section 3.3.2 to obtain a tomogram corresponding to a state influenced by dephasing. As an example, consider measuring tomogram element $\langle++++|\rho|++++\rangle$ for a state ρ affected with collective dephasing on qubits A and C. First, we measure $\langle++++|\rho|++++\rangle$ for an integration time $\tau/2$, counting the coincidences into tomogram element T_{518}. Then, we set waveplates in the experiment to measure projection $\langle-+-+|\rho|-+-+\rangle$ and resume the coincidence the remaining integration time, $\tau/2$, incrementing the tomogram element T_{518}. Note that we used the equivalence between transforming a measured state ρ and transforming a measurement operator Π, $\mathrm{Tr}[\Pi(U\rho U^\dagger)] = \mathrm{Tr}[(U^\dagger \Pi U)\rho)]$. The choice of transform determines which qubits suffer from dephasing. In this case, it is the qubit A and C simultaneously. The tomogram element is equivalent to measuring the projection of a balanced statistical mixture of initial and phase-flipped states with integration time τ. Repeating these steps for all tomogram elements would construct the tomogram. In this way, we obtain the tomograms corresponding to the states influenced by the investigated cases of dephasing. Notice that such measurement would involve measuring the same projection multiple times. In practice, we measure a four-qubit tomogram of an initial state, then suitably combine the lines into a new tomogram, equivalent to the previously described steps. This compromise to the experiment economy introduces artificial correlation to data. Fortunately, with large numbers of measured coincidences, these artifacts are getting negligible.

In the four-qubit state tomography, we also measured the output qubits C and D in the superposition basis $|\pm\rangle$. For each of the four combinations of measurement outputs, we select the corresponding sub-tomogram and reconstruct it to obtain the two-qubit density matrix of the output state of qubits A and B. Up to single-qubit phase flips, we should obtain a pure maximally entangled two-qubit state $U_{\text{CZ}}|+\rangle|+\rangle$ provided the protection against dephasing is functional.

The results are summarized in Table 4.3, where we display fidelities and entanglement

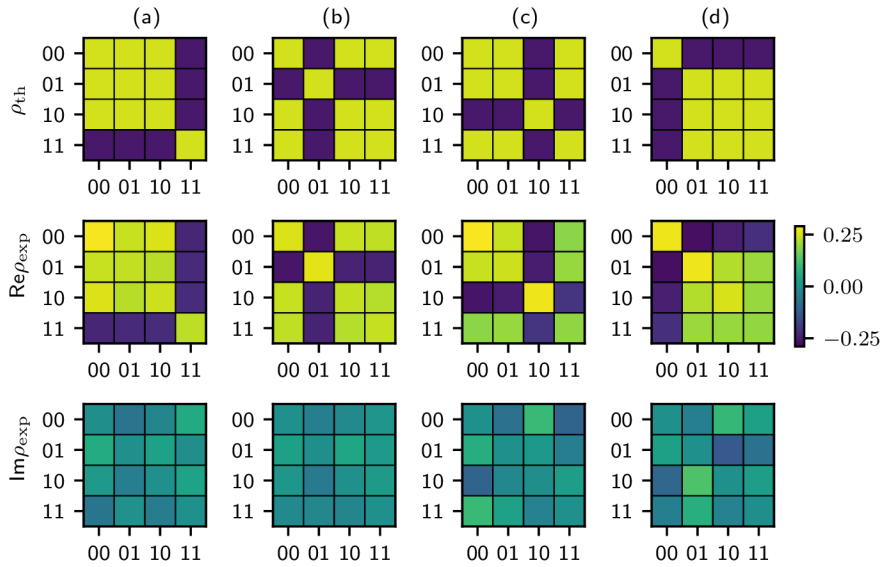

Figure 4.11: Theoretical (top row) and experimental (middle and bottom row) density matrices of output two-qubit states of A and B for decoherence-resilient implementation of the U_{CZ} gate under full collective dephasing. Imaginary parts of all plotted theoretical density matrices vanish. The results are shown for superposition input state $|+_L\rangle|+_L\rangle = |\Psi^+\rangle|\Psi^+\rangle$ and four different measurement results on qubits C and D: $++$ (a), $+-$ (b), $-+$ (c), $--$ (d).

of formation of the output two-qubit state of A and B for the three different combinations of dephasing and four different measurement outcomes on qubits C and D. In all cases, we achieve high fidelities and preserved entanglement, which confirms the protection from dephasing and also illustrates that a feedforward could be used to recover the correct output state of qubits A and B for any combination of measurement outcomes on qubits C and D. In Fig. 4.11 we plot the output density matrices of two-qubit states of A and B obtained for independent collective dephasing on both pairs of qubits. This figure further confirms the closeness between the theoretical expectations and experimental results and it also depicts the single-qubit phase flips imposed by measurements on qubits C and D.

$\|\text{CD}\rangle$	F_{AB}^{A}	F_{AB}^{B}	F_{AB}^{AB}	E_{AB}^{A}	E_{AB}^{B}	E_{AB}^{AB}
$\|++\rangle$	0.920(9)	0.930(9)	0.947(5)	0.87(2)	0.92(2)	0.90(1)
$\|+-\rangle$	0.961(6)	0.962(5)	0.960(4)	0.91(1)	0.92(2)	0.91(1)
$\|-+\rangle$	0.888(8)	0.912(7)	0.918(6)	0.84(2)	0.86(2)	0.87(2)
$\|--\rangle$	0.911(7)	0.918(7)	0.921(5)	0.88(2)	0.88(2)	0.89(1)

Table 4.3: Experimental fidelities and entanglement of formation of output states of qubits A and B for input state $|+\rangle|+\rangle$ and full collective dephasing acting on pairs of qubits A and C (F_{AB}^{A}, E_{AB}^{A}), B and D (F_{AB}^{B}, E_{AB}^{B}), or both A and C, and B and D (F_{AB}^{AB}, E_{AB}^{AB}). The entanglement of formation and fidelities are shown for four different outcomes of measurements on output qubits C and D.

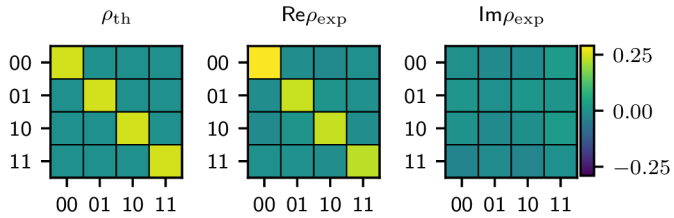

Figure 4.12: Influence of individual dephasing on qubits A and B. Input state was $|+_L\rangle|+_L\rangle$ and measurement result on qubits C and D was ++. The output state is affected by decoherence and becomes very close to the maximally mixed state.

$\|\mathrm{CD}\rangle$	F_{AB}^{A}	F_{AB}^{B}	F_{AB}^{AB}	E_{AB}^{A}	E_{AB}^{B}	E_{AB}^{AB}
$\|++\rangle$	0.44(1)	0.47(1)	0.25(1)	0.005(5)	0.07(2)	0
$\|+-\rangle$	0.48(1)	0.50(1)	0.27(1)	0.010(7)	0.07(1)	0
$\|-+\rangle$	0.46(1)	0.46(1)	0.25(1)	0.001(4)	0.05(1)	0
$\|--\rangle$	0.46(1)	0.48(1)	0.26(1)	0.001(4)	0.06(1)	0

Table 4.4: The same as Table 4.3, but the dephasing acts only on single qubits A and B, while qubits C and D remain intact.

We have also performed reference measurements where the dephasing was always applied only to one of the two physical qubits encoding a logical qubit. Specifically, phases $\phi_C = \phi_D = 0$ were set throughout the whole measurement, while ϕ_A and ϕ_B were set to 0 or π as required to apply dephasing to a given qubit. In this case, the encoding is of no use and the output state suffers from a loss of coherence. In Table 4.4, we provide similar data as in Table 4.3 but now for dephasing acting on qubits A and B only. We can see that the entanglement practically vanishes and the fidelities drop significantly due to decoherence. Theoretically, entanglement is completely erased by such dephasing, $E = 0$, and we expect fidelity $\frac{1}{2}$ for decoherence on a single qubit and $\frac{1}{4}$ for decoherence on both qubits. Our experimental results are in good agreement with these theoretical predictions. In Fig. 4.12, we give an example of the output density matrix of qubits A and B when they both suffered from complete dephasing. The decoherence washes out all off-diagonal elements of the density matrix, and the state becomes very close to the maximally mixed state.

4.6 Discussion

In summary, we have experimentally demonstrated and characterized a four-qubit optical quantum logic circuit whose core is formed by a four-qubit C^3Z gate. The scheme exploits the encoding of two qubits into polarization and path degrees of single photons and involves two crossed inherently stable interferometers. We have verified the high-fidelity performance of the central four-qubit C^3Z gate and we have demonstrated that it can generate genuine multipartite entanglement. The experiment illustrates that Monte Carlo

sampling and Hofmann fidelity bounds are useful methods of characterization of complex multi-qubit quantum devices. The applicability of these methods is rather universal, and they can be used to efficiently characterize quantum logic gates and circuits implemented on various physical systems. As an example of application, we have used the C^3Z gate to construct a quantum CZ gate operating on two logical qubits, each supported by two physical qubits. We have shown that the presented encoding of logical qubits is resilient to collective dephasing.

Chapter 5

Three-qubit controlled-phase gate

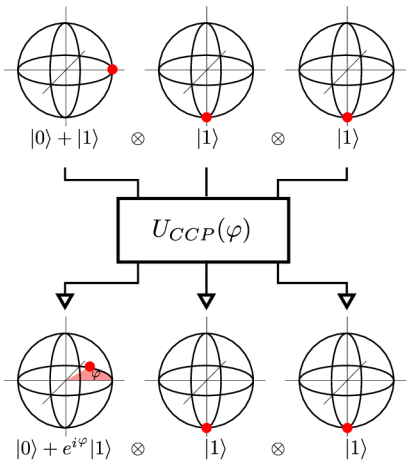

Figure 5.1: The action of the three-qubit phase gate. Phase shift, here Φ, could be arbitrarily selected. The phase shift is illustrated as a red arc.

This chapter is based on publication [A5]. The three-qubit controlled-phase gate

$$U_{CCP}(\varphi) = \exp(i\varphi|111\rangle\langle 111|) \tag{5.1}$$

introduces a variable phase shift φ between $|0\rangle$ and $|1\rangle$ components of a target qubit provided that the control qubits are in state $|1\rangle$, as illustrated in Fig. 5.1. Similarly to the CZ gate, each qubit can act as the control as well as the target. In this chapter, we use the previously introduced C^3Z gate to implement the controlled-phase gate which we use to demonstrate a protocol for protecting a qubit from decoherence.

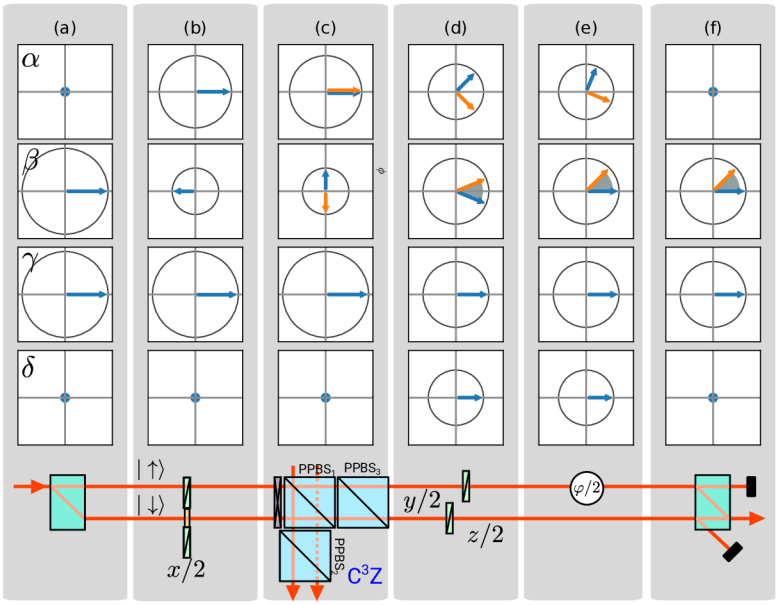

Figure 5.2: Implemented CCP gate and an example of its action. See Fig. 5.3 for the full experimental setup and the legend. As an example, we plot the evolution of input state $|+\rangle$. Plotted arrows represent complex amplitudes α, β, γ, δ corresponding to top-horizontal, top-vertical, bottom-horizontal, and bottom-vertical components. Orange arrows illustrate the case in which the C^3Z gate introduces a π-phase shift. Grey arcs in the plots represent the introduced conditional phase φ.

5.1 Gate principle and characterization

The U_{CCP} gate is implemented as a combination of a fixed four-qubit gate and several fixed and tunable two-qubit and single-qubit gates, see the bottom part of Fig. 5.2. We explain the action of the gate using an example with input states $|+\rangle\otimes|1\rangle\otimes|1\rangle$ and $|+\rangle\otimes|0\rangle\otimes|0\rangle$. Let us call the first qubit the target. (a) The first beam displacer extends the Hilbert space by adding a path degree of freedom. The resulting target qudit is $\alpha|\uparrow H\rangle+\beta|\uparrow V\rangle+\gamma|\downarrow H\rangle+\delta|\downarrow V\rangle$ and its complex amplitudes are plotted as arrows in the complex plane in Fig. 5.2. (b) A ring waveplate couples polarization modes in the upper arm and successive (c) quarter-wave plate shifts the phase of a vertically-polarized component in both optical paths. The coupling between two photons is introduced by C^3Z gate (c), which we discussed in the previous chapter. The phase is conditionally π-phase shifted, depending on the state of control qubits. In our example, we distinguish between input control qubits in state $|00\rangle$ and $|11\rangle$ and we plot the complex amplitudes in blue and orange color accordingly. (d) The remaining two half-wave plates acting individuality on each arm couple the polarization components again. Finally, we compensate the unwanted fixed phase-shift (e) between the two paths by tilting the second beam displacer (f), which also discards auxiliary modes and merges the remaining modes into a single beam.

To achieve the conditional phase shift φ, the waveplate angles $x/2$, $y/2$, and $z/2$ have

to satisfy the following conditions

$$|\tan x| = \sqrt{\cot(|\varphi|/2)}, \qquad y = x, \tag{5.2}$$

and

$$\cos z = \sqrt{\cos^4 x + \sin^4 x}. \tag{5.3}$$

The gate success probability depends on the value of the phase shift φ,

$$p_{CCP} = \frac{1}{9(1 + |\sin\varphi|)}. \tag{5.4}$$

The total success probability of the gate is thus minimal for $\varphi = \pi/2$. Factor 1/9 originates in the central C^3Z gate and the rest of the expression comes from the fact that we discard the auxiliary modes.

For the experimental test of the quantum decoherence control by dark states of the environment, described in the following section, we also added a unitary gate V acting on a signal polarization qubit and an effective controlled-phase shift operation

$$U_{\mathrm{CP}}(\varphi) = \exp(i\varphi|11\rangle\langle 11|), \tag{5.5}$$

acting on the signal qubits. Both these operations are implemented by waveplate sequences. The complete experimental setup is depicted in Fig. 5.3.

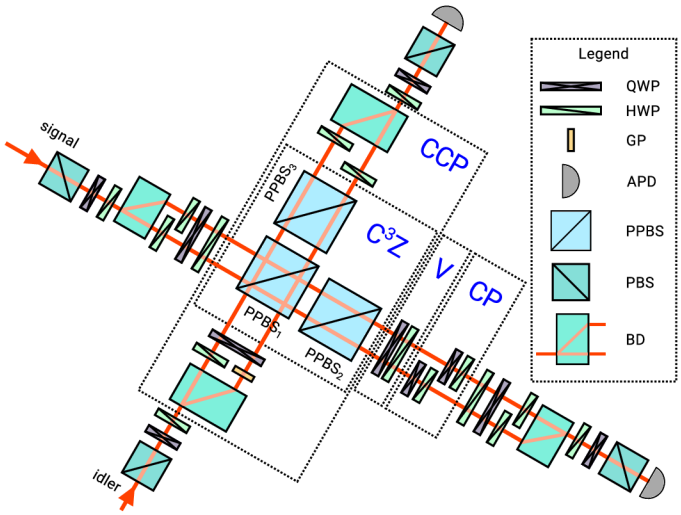

Figure 5.3: Scheme of the experiment. The signal photon carries two qubits encoded in its path and polarization. The remaining qubit is encoded into the polarization of the idler photon. The CCP gate is discussed in detail in the text. Additional gate V acts on the signal polarization qubit and is implemented by a pair of waveplates. The controlled-phase gate (CP) is implemented by placing a pair of waveplates into each path of the signal photon.

We have performed full quantum process tomography of the CCP gate for eight different values of φ. During the tomography, operations V and U_{CP} were set to perform the

identity operation. In Figure 5.4, we show the full reconstructed quantum process matrix of the CCP gate for $\varphi = \pi/2$. A briefer characterization of the gate is provided by its fidelity and purity, which are plotted in Figure 5.5 for all the tested coupling strengths φ. The results indicate the good and stable performance of the gate for the whole range of φ. To estimate the uncertainty of the tomographically obtained quantities, we employed the bootstrapping method described in Section 3.1.6. The number of bootstraps was 1000, and the mean count-rate for bootstraps generation was $400/(1 + |\sin\varphi|)$ Hz. The choice of count-rate for bootstrapping is based on the experimentally observed count rate.

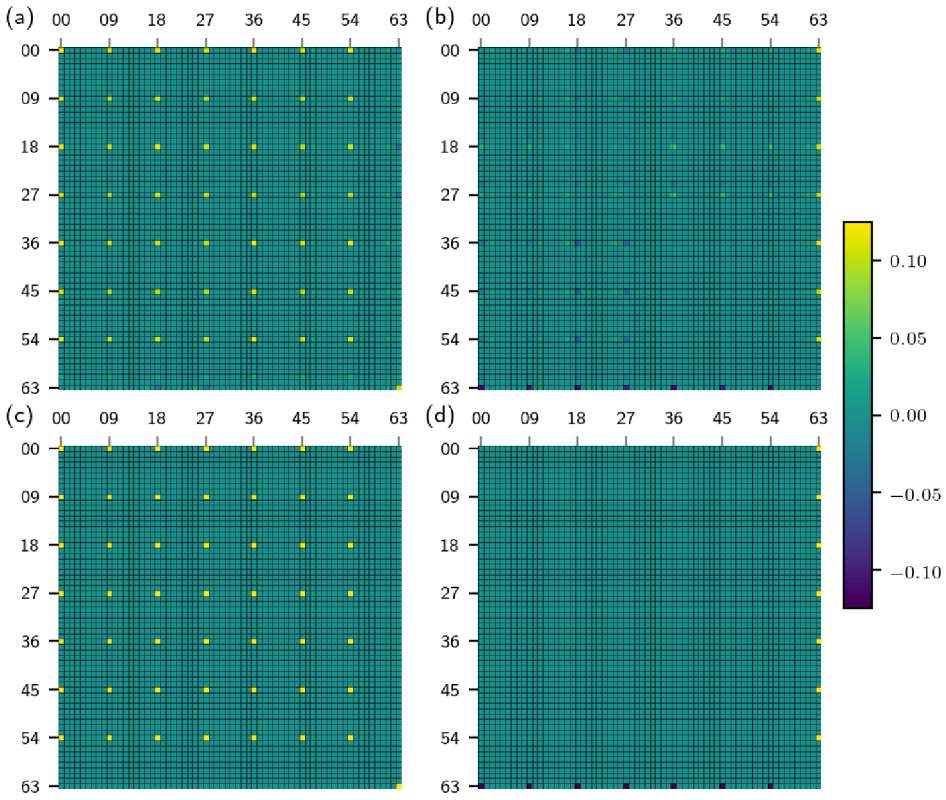

Figure 5.4: Quantum process of the controlled-controlled-phase gate for $\varphi = \pi/2$. Shown are the real (a,c) and imaginary (b,d) parts of the quantum process matrix χ. Experimental results plotted in panels (a,b) can be compared with the ideal process matrix of the gate (c,d). The color bar is shared by all matrix plots.

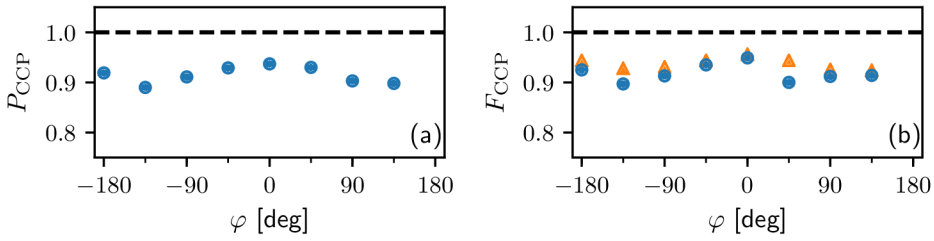

Figure 5.5: Experimentally determined purity $\mathcal{P}_{\mathrm{CCP}}$ (a) and fidelity F_{CCP} (b) of the implemented controlled-controlled-phase gate. Orange triangles show the maximal fidelity that we would obtain after optimal local unitary phase shifts of the output qubits. Error bars denote three standard deviations and are smaller than the size of the symbols.

5.2 Decoherence suppression by dark-states of the environment

Decoherence is traditionally described as entangling two quantum parties - *system* and *environment*. The system is accessible and can be controlled in contrast to the inaccessible environment. Inaccessible information about the environment manifests as decoherence of the system part. The CCP gate provides a way to couple qubits with tunable coupling strength, given by φ. With the gate, we simulate the decoherence and tune its severity. Here we utilize our experimental setup to test the decoherence suppression protocol, which prepares the environment in a *dark state* indirectly by prior decoherence-interaction with an auxiliary state.

If the interaction with the effective environment has a suitable form, and the effective environment is small enough, then one can attempt to switch off this interaction by preparing the environment in a suitable *dark state*, which decouples it from the system qubits that we want to protect. Although the environment is assumed to be directly inaccessible, it can be influenced *indirectly* via measurements on the system qubits after their interaction with the environment. One thus utilizes the remote state preparation protocol [154] that benefits from quantum correlations between the system and the environment that were established uniquely by their interaction responsible for the decoherence. Such protocol has been theoretically proposed in Ref. [155], where it was illustrated on the proof-of-principle example of a single system qubit coupled to an environment represented by a single quantum harmonic oscillator.

Here, when we refer to the environment, we have in mind a small well-defined quantum system [156, 157] and not a general environment for open quantum systems such as thermal bath. In our test, both the system and the environment are represented by a single qubit. We encode qubits into path and polarization degrees of freedom of single photons and implement the required three-qubit quantum logic circuit with linear optics. We comprehensively characterize the decoherence suppression protocol by quantum state and quantum process tomography.

5.2.1 Decoherence suppression protocol

Let us begin with a theoretical description of the protocol. We consider a simple yet practically important and ubiquitous coupling of an initially uncorrelated system (S) and an environmental (E) qubits via unitary controlled phase shift operation $U_{CP}(\varphi)$ (5.5), with $0 \leq \varphi \leq \pi$ specifying the coupling strength. This system-environment coupling reduces the coherence between the two computational basis states of the system qubit. Specifically, $\rho_{S,01} \rightarrow q\rho_{S,01}$, where $\rho_{S,01} = \langle 0|\rho_S|1\rangle$, $q = p_{0,E} + e^{i\varphi}p_{1,E}$, and $p_{j,E} = \langle j|\rho_E|j\rangle$ is the probability that the environmental qubit is in state $|j\rangle_E$. Here ρ_S and ρ_E denote initial density matrices of the system and environmental qubit. It holds that $|q| < 1$ unless $\varphi = 0$, $p_{0,E} = 1$, or $p_{1,E} = 1$.

The interaction between the system and the environment can be switched off provided that the environmental qubit, which is not directly accessible, can be prepared in state $|0\rangle_E$. This can be achieved by the following protocol. Before the system qubit is used for information encoding, it is prepared in a pure superposition state $|+\rangle_S = \frac{1}{\sqrt{2}}(|0\rangle + |1\rangle)_S$, and after interaction with the environment, it is projected onto state

$$|\varphi_\perp\rangle_S = \frac{1}{\sqrt{2}}\left(|0\rangle - e^{i\varphi}|1\rangle\right)_S. \tag{5.6}$$

It is easy to verify that ${}_S\langle\varphi_\perp|U_{CP}(\varphi)|+\rangle_S|1\rangle_E = 0$ hence successful projection of the system qubit onto state $|\varphi_\perp\rangle_S$ heralds preparation of the environment in a dark state $|0\rangle_E$.

The success probability of the protocol reads

$$P_S = p_{0,E}|\langle\varphi_\perp|+\rangle|^2 = p_{0,E}\sin^2\frac{\varphi}{2}. \tag{5.7}$$

Therefore, unless the environmental qubit is initially in a pure state $|1\rangle_E$, we can always conditionally switch the decoherence off before the system qubit is used for some application. Notably, the success probability P_S increases with increasing interaction strength up to a maximum at $\varphi = \pi$ and vanishes in the limit $\varphi \rightarrow 0$. In this limit, the environment affects the system qubit only very weakly and thus the output states of the system qubit corresponding to the environmental states $|0\rangle_E$ and $|1\rangle_E$ become almost indistinguishable. By contrast, for $\varphi = \pi$ those two states become orthogonal.

If the system qubit is not projected on the desired state $|\varphi_\perp\rangle_S$ but on its orthogonal counterpart $|\varphi\rangle_S = \frac{1}{\sqrt{2}}(|0\rangle + e^{i\varphi}|1\rangle)_S$, we may attempt to repeat the remote state preparation procedure until it succeeds. This assumes that the system qubit can be repeatedly refreshed and prepared in state $|+\rangle_S$. The success probability after up to N repetitions of the protocol is given by $P_{S,N} = p_{0,E}\left[1 - \cos^{2N}(\varphi/2)\right]$. This probability can be further increased if the environment could thermalize to its initial state after each unsuccessful attempt. In such a case, the overall probability of success after up to N repetitions reads $P_{S,N} = 1-(1-P_S)^N$, where P_S is the single-shot success probability given by equation (5.7). Asymptotically, we can thus reach deterministic preparation of the dark state $|0\rangle_E$ unless the environment is initially in state $|1\rangle_E$. We note that in contrast to decoherence suppression via weak measurements and quantum measurement reversal [90, 158, 159] which

relies on an application of suitable quantum filters to the measured qubit, our goal here is to perform an *indirect* projective measurement on the environmental qubit, not a weak measurement. Also, the target of our protocol is the environment and not the decohered system qubit that just serves as a proxy to indirectly control the environment.

So far we have assumed that the coupling strength φ is known. This allows us to decouple the environment from the system in a single shot. However, in practice, φ may be unknown or may even fluctuate in time. In such a case one can conservatively choose to project the output state of the signal qubit onto state $|+\rangle_{\mathrm{S}}$. Although this generally does not exactly prepare the environmental qubit in state $|0\rangle_{\mathrm{E}}$, it reduces the probability $p_{1,E}$ with respect to $p_{0,\mathrm{E}}$. If we define the population ratio $R_{\mathrm{E}} = p_{1,\mathrm{E}}/p_{0,\mathrm{E}}$, then after a single implementation of the protocol with projection onto $|+\rangle$ we obtain

$$R'_{\mathrm{E}} = R_{\mathrm{E}} \cos^2 \frac{\varphi}{2}. \tag{5.8}$$

Hence we obtain reduction by a factor of $\cos^2(\varphi/2)$, which is smaller than 1 for all $0 < \varphi < 2\pi$. If the protocol can be repeated, then after N successful iterations, we obtain an exponentially strong reduction of the undesired state $|1\rangle_{\mathrm{E}}$ by factor $\left(\cos^2 \frac{\varphi}{2}\right)^N$. The qubit S can be therefore asymptotically perfectly protected even without prior knowledge of the coupling strength φ. Note that this protocol is not limited to the interaction (5.5). An analogical procedure can be applied for any unitary coupling $\exp(i\varphi\sigma_S \otimes A_E)$, where σ_S is any Pauli matrix and A_E is a Hermitian operator of an arbitrarily complex environment [160–165].

5.2.2 Experimental test

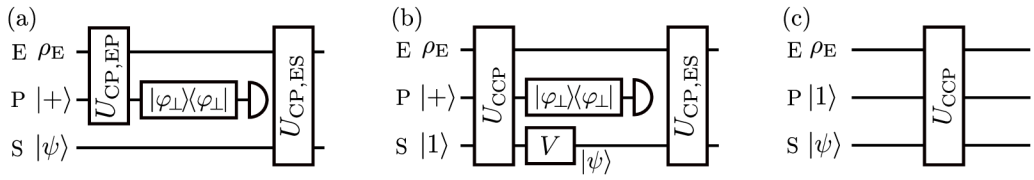

Figure 5.6: (a) Quantum circuit implementing the proof of principle test of decoherence suppression protocol. The circuit involves three qubits: environment (E), probe (P) and signal (S). Qubits E and P are coupled by U_{CP} gate. Projection of the qubit P onto the state $|\varphi_\perp\rangle$ heralds successful preparation of the qubit E in the dark state $|0\rangle$. The qubit S is then not altered by interaction with qubit E. **(b)** Experimentally implemented quantum circuit, equivalent to circuit (a). Here qubit S is initially prepared in a fixed state $|1\rangle$ and all three qubits E, P, and S are coupled by U_{CCP} operation. An arbitrary pure state $|\psi\rangle$ of the qubit S is then prepared with the use of a single-qubit gate V. **(c)** Reference quantum circuit for observing decoherence effects of the environment. This circuit is equivalent to the two-qubit gate U_{CP} acting on qubits E and S.

In the experiment, we aim to verify that the interaction with the environment was switched off by the above-described procedure. Since we encode qubits in photons whose detection is destructive, we utilize two different system qubits, probe P and signal S. The

probe serves for the prior control of the quantum state of the environment. Signal qubit is then used to test the success of the decoherence suppression protocol. The protocol thus requires two controlled-phase gates U_{CP}, one between the probe and environmental qubits and the other acting on the signal and environmental qubits, as depicted in Figure 5.6 (a).

With signal qubit initially prepared in state $|1\rangle_{\mathrm{S}}$, the U_{CCP} gate effectively acts as U_{CP} gate for the remaining qubits E and P. The experimentally implemented circuit depicted in Figure 5.6(b) is therefore fully equivalent to the circuit in Figure 5.6 (b). We also utilize the quantum circuit depicted in Figure 5.6 (c) that serves as a reference to directly observe the effect of unsuppressed decoherence.

In our experiment, we have direct access to the environmental qubit, but this access is only utilized to prepare a physically well-motivated initial state of the environment. Specifically, we consider the worst-case scenario and the environmental qubit is initially prepared in a maximally mixed state. Similarly, measurement of the output environmental qubit is performed only due to the way we technically implement our linear optical quantum gate that operates in coincidence basis. However, we effectively trace over the environmental qubit by summing the measured coincidence counts over all outcomes of measurements on this qubit. To maximize the homogeneity of this procedure, we sum over outcomes of sequential projective measurements in three mutually unbiased bases. The environment is thus effectively discarded and the information from measurement on the environmental qubit is erased and not used in the implemented protocol.

We have tested the performance of the protocol for various interaction strengths φ and for six signal qubit states from the set $\mathcal{S} = \{|0\rangle, |1\rangle, |+\rangle, |-\rangle, |\circlearrowleft\rangle, |\circlearrowright\rangle\}$ that contains three mutually unbiased bases. The environmental qubit is prepared in a maximally mixed state $\rho_{\mathrm{E}} = \frac{1}{2}I$, which is generated as an equal mixture of the six states from $\mathcal{S}$, and the probe qubit is initially prepared in pure input state $|+\rangle_{\mathrm{P}}$. The probe qubit was measured in the superposition basis $\frac{1}{\sqrt{2}}(|0\rangle \pm e^{i\varphi}|1\rangle)$ and projection onto $|\varphi_{\perp}\rangle = \frac{1}{\sqrt{2}}(|0\rangle - e^{i\varphi}|1\rangle)$ heralded decoupling of the environmental qubit. We have performed full quantum state tomography of the output signal qubits, which allowed us to completely characterize the performance of our protocol.

The results are depicted in Figure 5.7. The blue dots represent experimental data and the blue dashed lines indicate predictions of an ideal theoretical model of our quantum circuit, which does not consider any imperfections. For each of the six signal qubit states, we plot the dependence of the output state purity $\mathcal{P}_{\mathrm{S}} = \mathrm{Tr}[\rho_{\mathrm{S}}^2]$ and fidelity $F_{\mathrm{S}} = \langle\psi|\rho_{\mathrm{S}}|\psi\rangle$ on the phase shift φ. We also provide a plot of the relative success probability of our protocol $\tilde{P}_S(\varphi) = P_S(\varphi)/P_S(\pi)$. Since the total success probability of the protocol $P_S(\varphi)$ is influenced by various loss factors in the optical setup, it is hard to estimate. We therefore utilize the relative success probability that can be reliably determined from the collected data as a ratio of coincidence counts. This approach assumes that our source produces a constant number of photon pairs per second on average, which was confirmed by independent measurement. Note that besides the bona fide success probability of the protocol, $\tilde{P}_S$ also includes the success probability of the conditional three-qubit CCP gate, which depends on φ, $p_{\mathrm{CCP}} = \frac{1}{9+9|\sin\varphi|}$. The error bars were determined using the bootstrapping

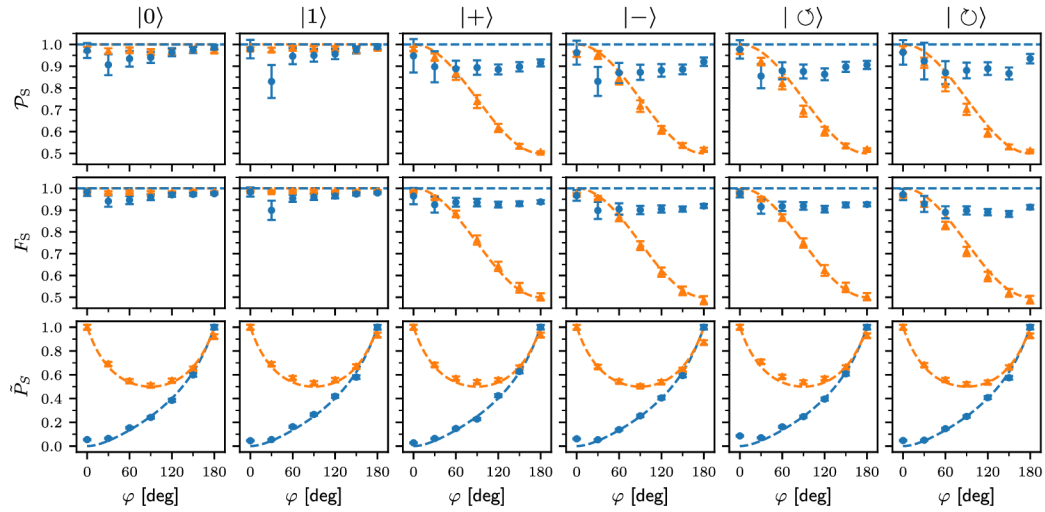

Figure 5.7: Experimental verification of decoherence suppression. The figure shows the output system qubit purity $\mathcal{P}_S$ (upper row) and fidelity F_S (middle row), as well as the normalized success probability of the protocol $\tilde{P}_S$ (bottom row) in dependence on the system-environment coupling strength φ. The results are plotted for six different input states of signal qubit that form three mutually unbiased bases. Blue dots represent experimental data and the blue dashed lines indicate predictions of a theoretical model. For comparison, orange triangles and lines show results for a reference scheme where the system qubit is unprotected and interacts with the environment. The environment qubit is initialized in a maximally mixed state. The error bars represent three standard deviations. Note that the plotted success probability $\tilde{P}_S$ includes the success probability of implementation of the linear optical CCP gate.

method. For completeness, we also repeated this test with the environment prepared in pure superposition state $|+\rangle$, the results are plotted in Fig. 5.8.

The measured fidelities in Figure 5.7 are smaller than 1, which indicates the presence of residual decoherence. Since in our experiment we have access to the output environmental qubit, we have performed its tomographic characterization to check whether we have indeed prepared the environment in the dark state. From the reconstructed density matrix, we have determined the residual population $p_{1,\mathrm{E}}$ of state $|1\rangle_E$ at the output of the protocol. The populations $p_{1,\mathrm{E}}$ are averaged over all six investigated input signal states and plotted as $\bar{p}_{1,\mathrm{E}}$ in Figure 5.9 as blue dots. Experimentally obtained populations $\bar{p}_{1,\mathrm{E}}$ are positive, although they should be ideally zero for every coupling strength. The residual population of $|1\rangle_E$ causes partial coupling of the signal and environment qubits which reduces the purity and fidelity of the output signal qubit.

Figure 5.9 indicates that $p_{1,E}$ increases with decreasing coupling strength φ. This can be easily understood since the weaker is the coupling strength, the lower is the success probability P_S because we are filtering out most of the photons. In the limit of weak coupling, the remote control of environmental qubit thus becomes very sensitive to experimental imperfections, such as partial distinguishability of the single photons, finite extinction ratio of polarizing components, wave-plate retardation and calibration errors, or interfer-

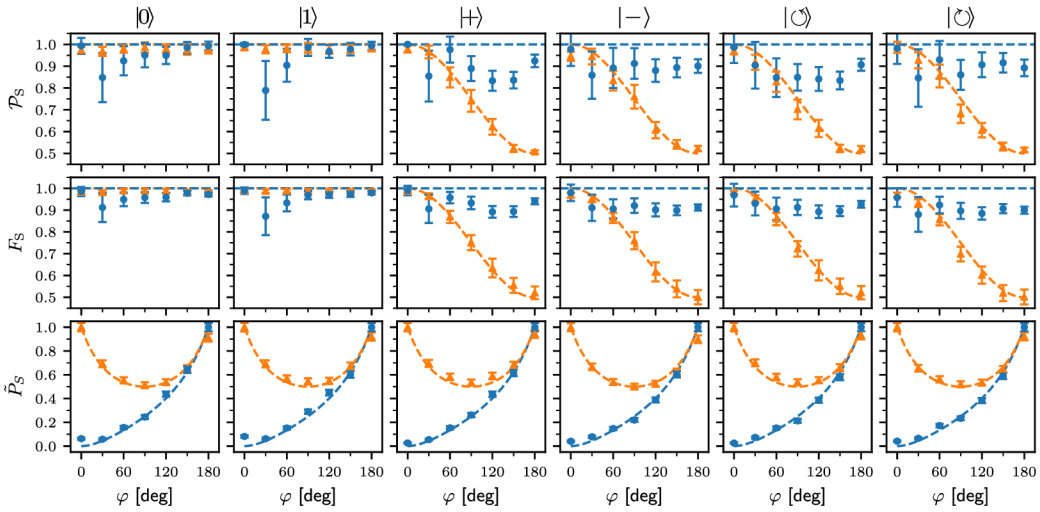

Figure 5.8: Verification of the protocol with a pure environment. The graphs is organized the same way as in Fig. 5.7.

ometric phase instability. The protocol is thus most efficient in the strong decoherence regime, when the decoherence suppression is most desirable, while it is not very effective for weak system-environment coupling when the decoherence effect is also weak. This can be contrasted with the standard quantum error correction that usually requires weak decoherence and a small probability of a single error to work efficiently. The resulting discrepancy between the ideal theoretical prediction and the observed experimental values in Figure 5.7 is the consequence of the interplay between the coupling strength φ and the residual population $p_{1,\mathrm{E}}$ caused by experimental imperfections.

As a reference and benchmark, we have also determined the change of the signal qubit induced by coupling to the environment when the protocol is not implemented and the probe qubit is not used. A quantum circuit of this reference measurement is shown in Figure 5.6(c). The probe qubit was set to state $|1\rangle$ and the signal qubit was prepared in the state $|\psi\rangle$ already at the input of the three-qubit CCP gate. The other gates were set to identity operations, and the output state of the signal qubit was again characterized by quantum state tomography. The experimental results for unsuppressed decoherence are plotted in Figure 5.7 as orange triangles together with predictions from an ideal theoretical model represented by orange dashed lines. It can be clearly seen that coupling to the environment causes dephasing of the signal qubit and reduces the purity and fidelity of all superposition states. The relative success probability for this reference measurement is defined as $\tilde{P}_S(\varphi) = P_S(\varphi)/P_S(0)$ since the largest P_S is observed for $\varphi = 0$. While the quantum logic circuit in Figure 5.6(c) as such does not involve any conditioning, our implementation of the CCP gate does. The observed explicit dependence of $\tilde{P}_S$ on φ thus essentially represents the dependence of the relative success probability of the CCP gate on φ.

From the collected tomographic data, we have reconstructed the process matrix χ of the effective single-qubit decoherence channel and evaluated its entanglement of forma-

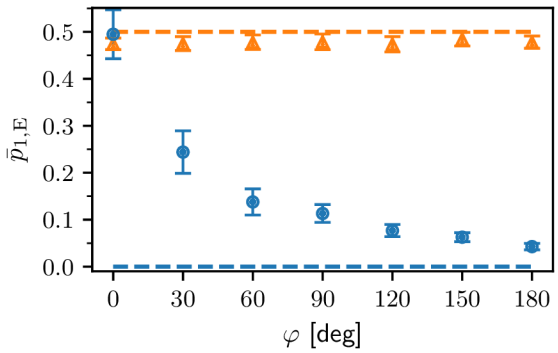

Figure 5.9: Mean population $\bar{p}_{1,E}$ after decoherence suppression (red dots) and without decoherence suppression (orange triangles). In both cases, the mean value is calculated over all six tested states of the signal qubit. The error bars show three standard deviations.

tion E_f (3.57) and fidelity F with the identity process matrix. Here we interpret the process matrix literally as a density matrix of a Bell state with one part transformed by the decoherence channel. The fidelity indicates how close the channel is to the ideal identity channel, and the entanglement of formation quantifies how the entanglement of the signal qubit with an external qubit is affected by the decoherence. Figure 5.10 shows the comparison between the cases with and without decoherence suppression protocol. The tested protocol helps to preserve entanglement in cases where the entanglement would be otherwise significantly reduced or even completely lost.

5.2.3 Conclusions and outlook

In summary, we have demonstrated a quantum decoherence suppression protocol that is based on *indirect* engineering of the environment's quantum state through the decoherence process. A crucial feature of the demonstrated protocol is that it involves only measurement on the system qubit subject to decoherence, and no direct manipulation with the environment or its measurement is required. The method is applicable whenever a dark state of the environment can be identified and the quantum correlations between signal, and environment established by their interaction have a suitable structure to allow indirect manipulation of the environmental state. The studied decoherence suppression protocol can be seen as complementary to the standard quantum error correction or dynamical decoupling and can be used in combination with such techniques. In particular, the protocol can be utilized at the beginning of a quantum information processing task to manipulate the environmental qubits and prepare them as close to the dark state as possible. The remaining residual effect of the environment during the quantum information processing could then be further suppressed by quantum error correction or dynamical decoupling. Beyond the already proposed application of this protocol to quantum dots [155], the method might be useful for decoherence suppression in many other physical platforms such as trapped ions [166, 167], superconducting circuits [168–170], or nanome-

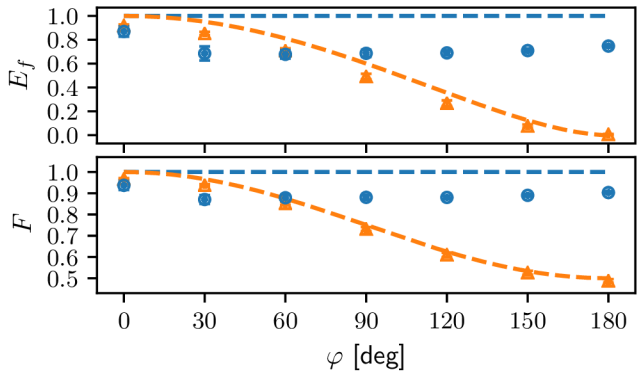

Figure 5.10: Parameters characterizing the single-qubit quantum channel representing decoherence of signal qubit. Entanglement of formation E_f (a) of the output signal qubit with an external qubit for an input maximally entangled Bell state and fidelity F (b) of the channel with the ideal identity channel are plotted for the decoherence suppression protocol (red dots) and for reference measurement with decoherence (orange triangles). Respective dashed lines show predictions from the ideal theoretical model. The error bars represent three standard deviations.

chanical oscillators [171–173].

Chapter 6

Fredkin gate

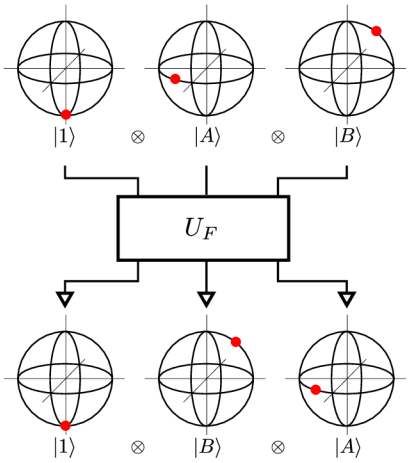

Figure 6.1: Action of the quantum Fredkin gate. The values of target qubits are swapped if the control qubit is active.

This chapter is based on publications [A3] and [A4]. The quantum Fredkin gate is a universal entangling three-qubit gate that implements a swap of two qubits controlled by another qubit, as illustrated in Fig. 6.1. The corresponding unitary operator was introduced in eq. (3.12). This chapter describes the gate's implementation and characterization and then its application in the direct measurement of nonlinear functionals of a density matrix.

Our implementation uses the decomposition into two controlled-not gates and a Toffoli gate, depicted in Fig. 6.2. Thanks to the deterministic implementation of controlled-not gates acting on hyper-encoded qubits, we implement the Fredkin gate with a theoretical success probability of 1/9. The success probability is equivalent to a single two-photon controlled-not gate [45–47]. We realize the Toffoli gate by applying a Hadamard gate on the input and output qubit of a three-qubit controlled-Z gate, defining a target qubit. The Hadamard gate is easy to implement on polarization qubits. Consequently, the

controlled-not gates in Fig. 6.2 are controlled by polarization. The controlled operation on hyper-encoded qubits implemented by path-specific waveplates is always controlled by path qubit. Therefore, we first need to swap the path and polarization qubits. Let us start the discussion there.

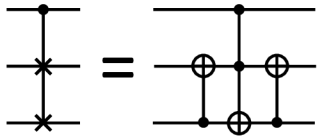

Figure 6.2: Decomposition of the Fredkin gate into two CNOTs and single Toffoli gate.

6.1 Swap gate for hyperencoded qubits

Section 3.2.4 described the hyperencoding in polarization and path degrees of freedom. The polarization degree of freedom is very easy to manipulate and analyze by using wave plates and polarizing components. The path degree of freedom can be implemented by employing a Mach-Zehnder interferometer (MZI), where the logical value of the qubit is determined by photon's path in the interferometer. When we place a polarization-manipulating element, such as a wave plate or a polarizer, into a single path of the interferometer, then the operation on the polarization qubit is performed if and only if the photon propagates through the path. We can say that the path qubit *controls* the polarization qubit. Unfortunately, it is not straightforward to manipulate the path qubit, except its phase, once encoded. To gain full and easy control over the path-encoded qubit, one can interchange both qubits using a SWAP gate, apply the required operation in the polarization domain, and swap both qubits back. The process of swapping two qubits is described by the following unitary operator

$$U_{\mathrm{sw}} = |00\rangle\langle 00| + |01\rangle\langle 10| + |10\rangle\langle 01| + |11\rangle\langle 11|, \tag{6.1}$$

where $|00\rangle$, $|01\rangle$, $|10\rangle$, and $|11\rangle$ represent computational basis states. The application of three consecutive CNOT gates exchanges the values of two arbitrary qubits. The swapping operation itself was examined theoretically [174–177] and experimentally [178] using momentum and polarization degrees of freedom of a single photon.

The working principle of our implementation is shown in Fig. 6.3. We assume two input spatial modes, ↑ and ↓, and two input polarization modes, H and V. The first qubit is encoded into the spatial mode and the second one into the polarization mode of a single photon. The logical states 0 and 1 in the second qubit correspond to polarization states H and V, respectively. The device is composed of two polarizing beam displacers (BD) separating H and V polarization components into different spatial modes and three waveplates (WP) changing H to V polarization state and vice versa.

The swap gate is implemented by a single-photon interference in two MZI formed by two beam displacers, depicted in Fig. 6.4. The two MZIs share one common path. In be-

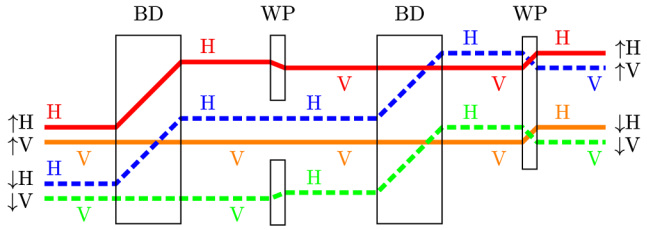

Figure 6.3: An illustrative scheme depicting the essence of our SWAP gate implementation for two photonic qubits encoded in path and polarization modes of a single photon. The different optical modes are denoted by the different colors and line styles to distinguish them.

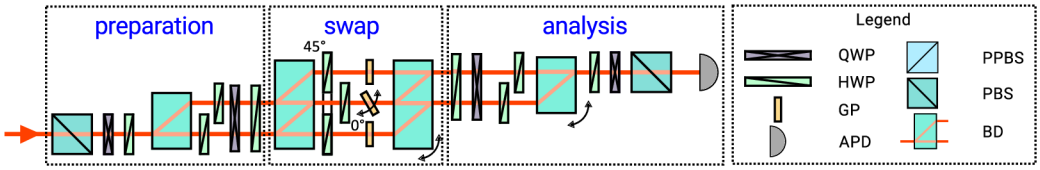

Figure 6.4: Experimental setup of the SWAP gate based on two coupled MZ interferometers. QWP - quarter-wave plate, HWP - half-wave plate, BD - beam displacer, GP - glass plate, PBS - polarizing beam splitter, APD - avalanche photodiode. See text for more details.

tween the beam displacers, there is a 45-degrees rotated ring-waveplate addressing outer paths and a small 6-mm waveplate addressing the inner path. Furthermore, there is one antireflectively coated glass plate of thickness 1 mm in each path to control the phase. The GPs in the top and bottom arms are tilted to set the individual phases in both interferometers and both phases are simultaneously tuned by tilting the beam displacer. To get the desired unitary operation (6.1), we apply σ_x operation to the output polarization qubit. We have merged this operation with the second qubit analysis in our realization. In principle, one could merge it with any subsequent polarization manipulation. The path length of the central interferometer was 320 mm. The fringe visibility of both MZI is calculated using the formula $V = (I_{\max} - I_{\min})/(I_{\max} + I_{\min})$, where $I_{\max}$ and $I_{\min}$ are the maximum and the minimum optical intensities at the output port, respectively. The interferometric visibility values for both MZI measured behind BD_3 by bulk photodetectors reach 0.974. We perform spatial filtering by coupling optical signal in the first qubit analysis block into a single-mode optical fiber. The spatial filtering increased the achieved visibility to 0.995 for both interferometers. We covered the whole experimental setup with a cardboard box to prevent unwanted phase fluctuations caused by air streams in the laboratory.

Alignment of the optical components and measurement of the setup's phase stability were done using classical laser light and PIN diodes. All other measurements were performed with a heralded SPDC single-photon source. It allowed us to test the gate under the same conditions as we will have for the Fredkin gate (single-photon level, same spectrum, same light source power, and polarization stability).

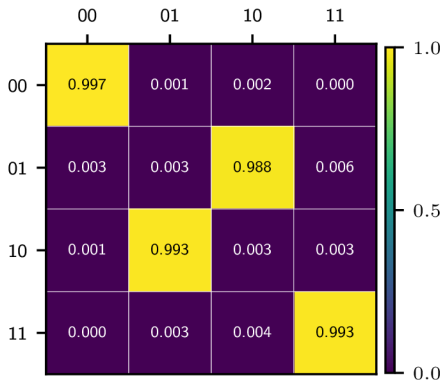

Figure 6.5: The truth table of the realized SWAP gate in computation basis estimated from experimental data. Rows represent prepared computational state and columns represent projection onto them. The numbers in cells and the color-coding represent normalized projection intensity.

The idler photons were fed directly to the fiber-coupled single-photon avalanche photodiode detector and served to herald the signal photons. Moreover, measurement in this coincidence regime allowed us to reduce the influence of the dark counts of APD detectors. We encode path and polarization qubits into the signal photons. Preparation and analysis of hyper-encoded qubits were described earlier in Section 3.2.4.

To show how the gate operates, we first measured the gate's truth table in the computation basis, depicted in Fig. 6.5. This demonstrates how the two-qubit SWAP gate operates. We also characterized the implemented two-qubit SWAP gate tomographically, using the standard approach with six Pauli eigenstates per qubit and reconstructed the process matrix χ using the maximum likelihood method.

Using the channel-state duality, we represent the ideal swap operation as a ket vector

$$|\chi_{sw}\rangle = \sum_{j,k=0}^{1} |jk\rangle|kj\rangle, \tag{6.2}$$

with the corresponding process matrix $\chi_{sw} = |\chi_{sw}\rangle\langle\chi_{sw}|$.

The quantum process fidelity of implemented two-qubit SWAP gate reaches $F_\chi = 0.9048(7)$ with process purity $P = 0.9021(1)$. The number in the parenthesis represents one standard deviation at the final decimal place. A possible source of the process fidelity reduction is an introduction of the phase shifts induced in one or more modes in the setup. Some of these phases can be compensated by suitable fixed phase corrections applied to process matrix χ on each of the two input and two output modes. After the application of single-qubit phase shifts both at the input and the output, the process fidelity reached $\tilde{F}_\chi = 0.9426(7)$. The theoretical and reconstructed process matrices χ of the SWAP gate after phase compensation are shown in Fig. 6.6. Statistical uncertainty of the results was estimated from 1000 bootstrap samples. In the next section, we show how we used the swap gates to implement the quantum Fredkin gate.

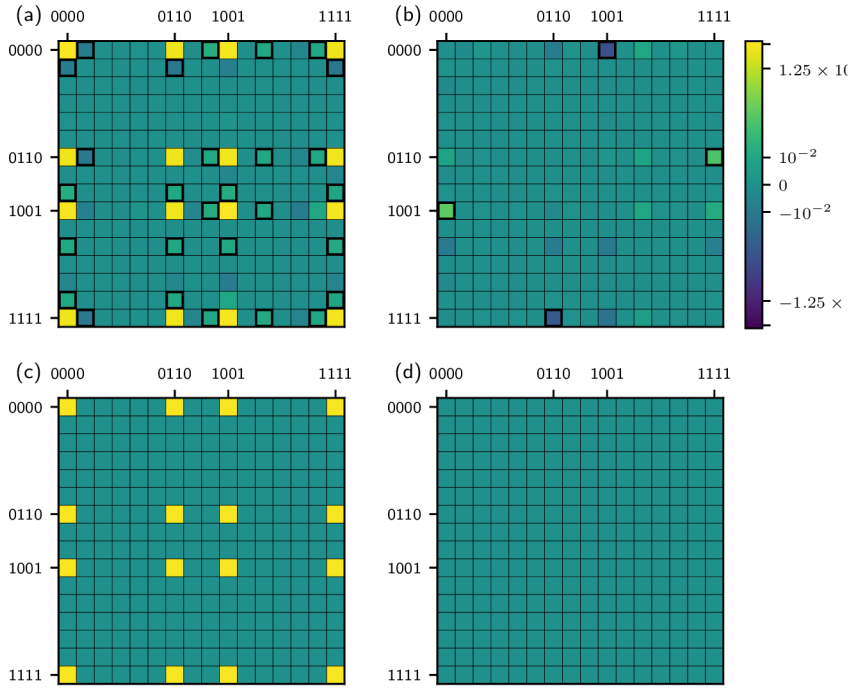

Figure 6.6: Reconstructed process matrices χ of the SWAP gate after phase compensation. The real (a) and imaginary (b) part of the reconstructed process matrix χ and its comparison to real (c) and imaginary (d) part of the theoretical process matrix χ_{th}. The matrices are plotted in computational basis, and ticks labels represent computational basis states. To highlight the differences, we plot the matrices in a symmetric logarithmic scale. Black highlighting in panel (a) mark parasitic elements with an absolute value greater than 0.01. Similarly, the highlighting in panel (b) marks the elements that deviate from the theory more than 5 deg in phase.

6.2 Quantum Fredkin gate

Our realization of the Fredkin gate includes two single-qubit Hadamard gates, two controlled-not and swap gates, and a three-qubit control-control-z (C^2Z) gate. Their arrangement is depicted in the circuit diagram in Fig. 6.7 (a). The target qubits are hyper-encoded into the path and polarization of the signal photon, while the control qubit is encoded into the polarization of the idler photon. State preparation and analysis are described in Section 3.2.2. The C^2Z gate with Hadamard gates applied on the target qubit's input and output side effectively realizes the Toffoli gate. The C^2Z gate is the only probabilistic component in our scheme and is implemented the same way as we described in Section 5. Visibility of the two-photon interference on the central PPBS largely decides the overall quality of the gate. In this experiment, we reached the visibility of Hong-Ou-Mandel dip $V_{\text{HOM}} = 0.966$. Before and after the C^2Z gate, we apply a swap gate on the hyperencoded qubits.

The CNOT gates operating on the hyperencoded qubits are implemented by inserting a HWP rotated by $\pi/4$ into a single spatial mode. It flips the state of the polarization qubit

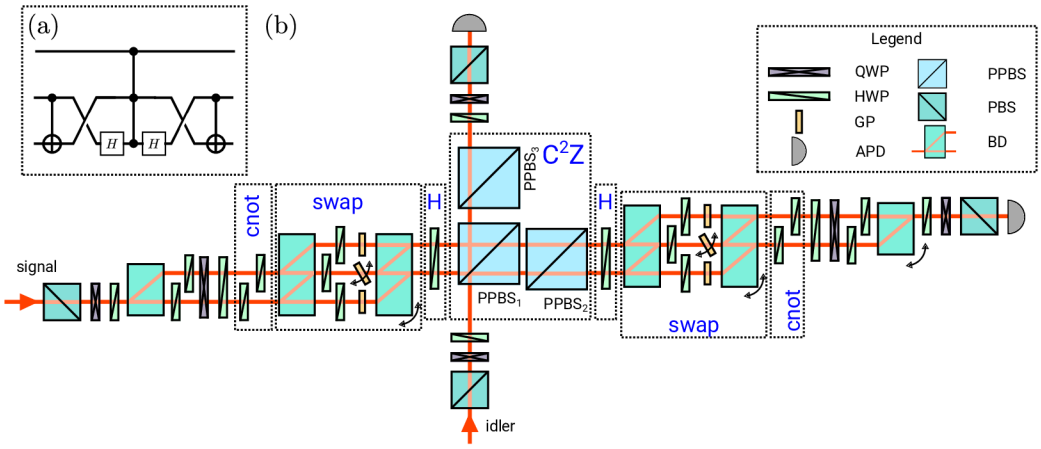

Figure 6.7: (a) Decomposition of the Fredkin gate into two CNOT gates and a Toffoli gate assisted by SWAP gates. (b) Experimental setup of the quantum Fredkin gate. The gate consists of a central probabilistic C^2Z gate and deterministic swap and CNOT gates operating on hyperencoded qubits.

but only for a single spatial qubit state. The Hadamard gates for the polarization qubit are realized by HWPs rotated by $\pi/8$ radians inserted into both paths.

Consequently, the experimental setup is composed of several Mach-Zehnder interferometers (MZI) with seven independent phases. Fig. 6.7 depicts the experimental setup. The challenge was to design a way to adjust all the interferometric phases. We had to sequentially reconfigure rotations of waveplates to let interfere only two optical paths at once and utilize the rest of the optical setup as a polarization analyzer. We created a computer program that performed these alignments automatically with the help of motorized waveplates, optical shutters [179], and piezo-enhanced prism turn-tables.

To demonstrate the function of the gate, we measured the truth table in computational basis, which we depict in Fig. 6.8. We calculate the classical fidelity $F_{\text{class.}} = 0.951$ as a mean over the truth table's row maxima. As before, we prepared a GHZ-like state $(|010\rangle + |101\rangle)\frac{1}{\sqrt{2}}$ to verify the entangling ability of the gate. We did so by preparing the target qubits in state $|01\rangle$ and the control qubit in the superposition state $|+\rangle$. The reconstructed density matrix of the resulting state is depicted in Fig. 6.9. The purity of the state was 0.904, and its fidelity to the ideal state was 0.941.

To quantify the gate's overall performance, we perform full quantum process tomography. We again used eigenstates of Pauli operators as probe and projection states. In total, we recorded $6^6 = 46\,656$ measurement records. To reduce the measurement time, we utilized both the reflection and transmission ports of the analyzer PBS and recorded all four two-fold coincidences simultaneously. We are aware of the potential systematic errors caused by the unequal losses and detection efficiency, but it was worth reducing the measurement time from 64 hours to 16 hours. During the tomography, roughly every two hours, the computer readjusted the optical phases in the setup.

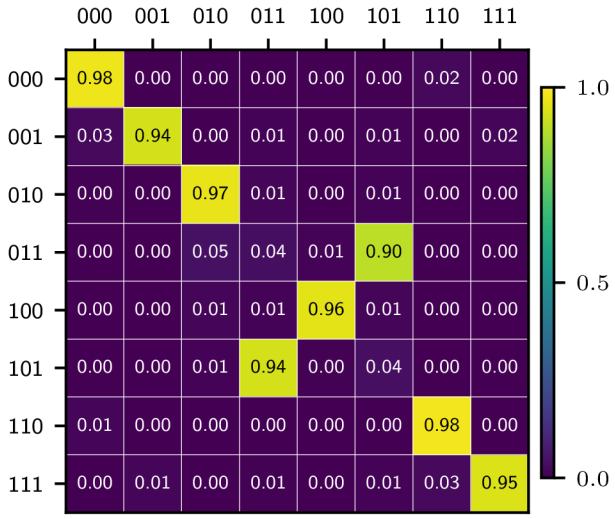

Figure 6.8: The truth table of the realized Fredkin gate in the computation basis estimated from experimental data. Rows represent prepared computational state and columns represent projection onto them. The numbers and color-coding represent the estimated projection probability.

We then use the maximum-likelihood estimation algorithm procedure to obtain the quantum process matrix χ_F, depicted in Fig. 6.10. The ket-vector

$$|\chi_{\mathrm{F}}\rangle = \sum_{i,j=0}^{1} (|ij0\rangle|ij0\rangle + |ij1\rangle|ji1\rangle) \tag{6.3}$$

describes the ideal quantum Fredkin gate using the channel-state duality. The gate's quality can be expressed by the process fidelity $F_{\chi_F} = \mathrm{Tr}[\chi\chi_{\mathrm{F}}]/(\mathrm{Tr}\chi\mathrm{Tr}\chi_{\mathrm{F}})$, where $\chi_{\mathrm{F}} = |\chi_{\mathrm{F}}\rangle\langle\chi_{\mathrm{F}}|$ is the process matrix of the ideal theoretical Fredkin gate. In our case, the process fidelity amounts to $F_\chi = 0.901$. We suspect that the imperfections that reduced the fidelity are mainly inherited from the imperfect two-photon interference, discussed theoretically in Section 3.2.3. Also, interferometric phase drift and fluctuations cause effective dephasing of qubits and imperfect waveplates cause both systematic errors of the gate itself and reconstruction artifacts, as we discussed in Section 3.2.5.

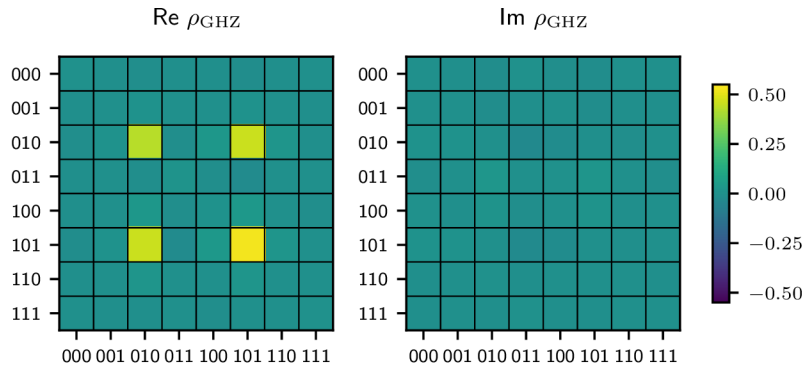

Figure 6.9: The matrix plot of the GHZ-like state prepared by the Fredkin gate.

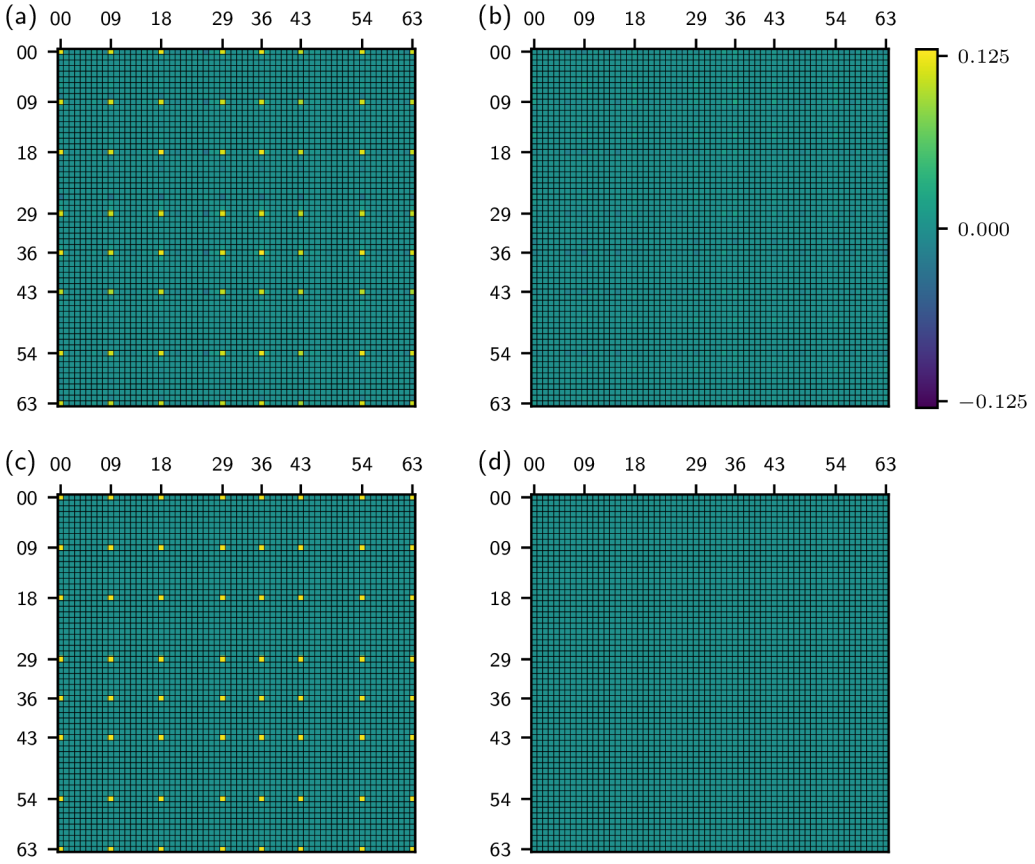

Figure 6.10: Reconstructed process matrices χ_F of the Fredkin gate after phase compensation. (a) The real and (b) imaginary part of the reconstructed process experimental matrix, respectively. The matrices are plotted in a computational basis. Ticks labels represent computational basis states represented as base-10 numbers. Real (c) and imaginary (d) part of the theoretical process matrix $\chi_{F,\mathrm{th}}$.

6.3 Symmetrization experiments with Fredkin gate

Projections on symmetric and antisymmetric subspaces play an important role in quantum measurements and quantum information processing. They allow direct measurements of nonlinear functionals of quantum states [180–182], direct evaluation of the overlap and Hilbert-Schmidt distance between different states [180, 181], and construction of programmable quantum multimeters [183, 184].

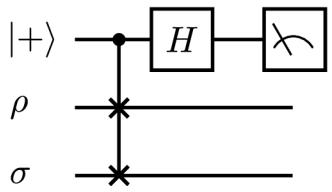

Figure 6.11: Quantum circuit for projecting state onto symmetric and antisymmetric subspaces. The outcome of the control qubit readout determines on which subspace the target qubits were projected.

Consider the situation depicted in Fig. 6.11. When the control qubit is initially in state $|+\rangle$, the circuit realizes projection onto either symmetric or antisymmetric subspace of the target qubits 1 and 2. These two operations correspond, respectively, to the action of operators $\Pi_S = |\Psi_-\rangle\langle\Psi_-|$, with $|\Psi_-\rangle = \frac{1}{2}(|01\rangle - |10\rangle)$ and $\Pi_A = 1 - \Pi_S$ onto the target qubits. Measurement of the control qubit in basis $|\pm\rangle$ reveals which projection was performed [180, 181]. Measurement results '+' and '-' indicate projection onto the symmetric and antisymmetric subspaces, respectively. It is inherently random whether the measurement outcome is '+' or '-'. Their probabilities depend on the state ρ_{12} of target qubits, $p_S = \mathrm{Tr}[\rho_{12}\Pi_S]$ and $p_A = 1 - p_S$. Using the operator of the Fredkin gate (3.12), we can show that the state post-selected with control qubit outcome $\pm$ is

$$\begin{aligned}\rho'_{12} &= \langle\pm|_3 U_{\mathrm{CSWAP}}(\rho_{12}\otimes|+\rangle\langle+|_3)U^\dagger_{\mathrm{CSWAP}}|\pm\rangle_3 = \\ &\frac{1}{4}\left[\rho_{12} + U_{\mathrm{swap}}\rho_{12}U^\dagger_{\mathrm{swap}} \pm \left(\rho_{12}U^\dagger_{\mathrm{swap}} + U_{\mathrm{swap}}\rho_{12}\right)\right].\end{aligned} \tag{6.4}$$

The trace of this state is

$$\mathrm{Tr}[\rho'_{12}]_\pm = \frac{1}{2}\{1 \pm \mathrm{Tr}\left[(\Pi_S - \Pi_A)\rho_{12}\right]\}, \tag{6.5}$$

where we used the relation between swap unitary operation and projector onto symmetric and antisymmetric subspaces, $U_{\mathrm{swap}} = \Pi_S - \Pi_A$. With the relation $\mathrm{Tr}[\Pi_S\rho_{12}] + \mathrm{Tr}[\Pi_A\rho_{12}] = 1$ we can rewrite (6.5) as

$$\begin{aligned}\mathrm{Tr}[\rho'_{12}]_+ &= \mathrm{Tr}\left[\Pi_S\rho_{12}\right], \\ \mathrm{Tr}[\rho'_{12}]_- &= \mathrm{Tr}\left[\Pi_A\rho_{12}\right].\end{aligned} \tag{6.6}$$

Let us now consider now separable input state on target qubits, $\rho_{12} = \rho\otimes\sigma$. With the relation $U_{\mathrm{swap}} = \Pi_S - \Pi_A$, one can show that

$$\mathrm{Tr}[(\rho\otimes\sigma)(\Pi_S - \Pi_A)] = \mathrm{Tr}[\rho\cdot\sigma]. \tag{6.7}$$

This equation provides a way to directly measure the overlap of two states and the purity of a state using its two copies. In the configuration depicted in Fig. 6.19, the Fredkin gate realizes a *nondestructive detector of exchange symmetry (NDES)*. We will distinguish two regimes in which we operate the NDES: when the control qubit is initially in the $|+\rangle$ state, we will say that the NDES is on. When the control qubit is initialized in state $|0\rangle$, and the device should implement identity operation, we will say the NDES is off. We use this regime for reference measurements.

The control qubit acts as an ancilla that can be destructively measured after interaction with the target qubits. The measurement reveals information about the two qubits in principle nondestructively. In this case, the quantum state is generally altered but the system itself is in principle not lost and can be processed further. However, full exploration of all features of the projective symmetrization [180, 181, 183, 184] requires versatile control of the input states and the ability to perform full quantum process tomography in addition to the high fidelity three-qubit gate. These were not simultaneously available in the previous implementation of the quantum Fredkin gate [138, 185].

As an example, consider the direct measurement of quantum state purity. The purity is a nonlinear functional which provides important information about the quantum state. Direct measurement of purity requires two copies of the state and for two identical polarization qubits it can be realized in the Hong-Ou-Mandel experiment [186, 187]. This, in practice, is just a destructive projection onto the symmetric and antisymmetric subspaces [180, 181]. With the help of the quantum Fredkin gate, these projections can also be realized without consuming the quantum systems. Unfortunately, our implementation of the Fredkin gate requires the detection of photons, so we have to consume the quantum systems in the end. However, prior to destroying the system, we can operate on them. To demonstrate this capability, we will perform quantum state tomography of the states after the symmetrization interaction.

6.3.1 Nondestructive direct purity measurement

Let us start with the first application, direct purity measurement [181]. We also verify the directly measured purities tomographically. The scheme is based on identity (6.7). It requires two copies of the investigated state ρ and employs them to measure the mean value $\langle \Pi_S - \Pi_A \rangle$. The individual operators Π_S and Π_A, corresponding to projection into the symmetric and antisymmetric subspaces, can be applied to the state and the estimated relative frequencies can be used for calculating the purity P as

$$P = \frac{f_S - f_A}{f_S + f_A}, \tag{6.8}$$

where f_S and f_A are the relative frequencies of the measurement outcomes on the control qubit, heralding the symmetric and antisymmetric projections. This technique was previously demonstrated for two polarization encoded qubits carried by single photons and destructive measurement based on the Hong-Ou-Mandel effect [186]. We use the NDES to demonstrate the preservation of the measured states.

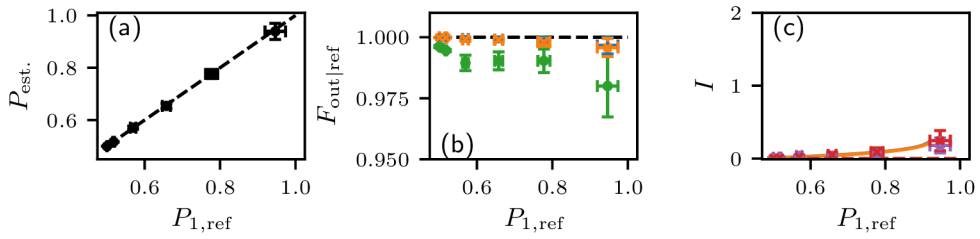

Figure 6.12: Data for the nondemolition measurement of purity using the NDES with error bars corresponding to one standard deviation. The shared horizontal axis shows the purity of a first reference target qubit $P_{1,\text{ref}}$ estimated from state reconstructions with the NDES off. It estimates the input purity. Dashed lines correspond to ideal theoretical predictions, while the points represent the experimental data. Error bars represent one standard deviation calculated over a set of six tested states. (a) Direct nondemolition measurement of purity using NDES. (b) Out-ref-fidelities obtained from tomographic data. Blue and orange color correspond to the first and second target qubit, respectively. Results for joint state target qubits are plotted by green color. (c) Mutual information estimated from the tomographic reconstruction of the target qubits. Purple color represents output state post measurement (NDES on), red colors reference (NDES off). The nearly overlapping solid lines are predictions based on the reconstructed process matrix.

We have tested the purity measurement for all eigenstates of Pauli operators. Data post-processing produces outcomes equivalent to the measurement of mixed states, as we described in Section 3.3.2. The pairs of identical input states have been prepared with average respective fidelity $F = 0.997(8)$. The number in the parenthesis represents one standard deviation at the final decimal place. The standard deviation was obtained by boostrapping and represents statistical error of the measured outcome.

We have performed full tomography of the target qubits, with the NDES on and off. The reconstructed reference (NDES off) density matrices were used to evaluate the input purities, which were compared to the ones obtained by the direct measurement, see Fig. 6.12 (a). The purities measured by the NDES closely match those obtained by the tomographic measurement. To verify that the measurement does not alter the state of target qubits, we have also analyzed the reconstructed output density matrices to compare the measured target qubits, in terms of their mutual information I, see Fig. 6.12 (c), and the fidelity of the output state with respect to the reference state (out-ref fidelity), see Fig. 6.12 (b).

For our purposes, we define the out-ref-fidelity of a quantum system as $F_{\text{out|ref}} = F(\rho_{\text{out}}, \rho_{\text{ref}})$, where ρ_{out} (ρ_{ref}) is the reconstructed density matrix of the system (either one or two qubits) when the NDES was on (off). The mutual information I is kept significantly below the possible maximum of two bits. The graph indicates that the measurement does not significantly increase the mutual information. The residual information is mainly caused by correlations in the input state. The initial correlations arise from the fact that the top and bottom interferometric paths were not perfectly identical in terms of polarization effects. At low purities, the residual correlation is hidden by mixing. The average out-ref fidelities are 0.999(1) for single qubits and 0.990(5) for the two-qubit states. The standard deviation is calculated over the set of six tested states. The error bar grows with increasing purity because the input states become more distinguishable and various

state-dependent imperfections manifest stronger.

Albeit the imperfections, the directly measured purity agrees with the tomographic reference measurements, and the measurement does not significantly introduce correlations nor alters the measured qubits. This nondemolition feature is caused by the initial exchange symmetry of input states.

6.3.2 Nondestructive direct overlap measurement

The next protocol we evaluate is the direct measurement of overlap between the target qubits [181]. Recall that when at least one of the qubits is pure, the overlap has the physical meaning of fidelity. Similarly to the purity measurement, we use the NDES to directly measure the overlap between the two target qubits. The overlap is

$$\mathrm{Tr}[\rho_1\rho_2] = \frac{f_S - f_A}{f_S + f_A}. \tag{6.9}$$

We started with the first target qubit in state $|0\rangle$ and the second in state $\cos\alpha|0\rangle + \sin\alpha|1\rangle$ and iterated the α parameter through 19 values ranging from 0 to $\pi/2$ radians. First, we measured and estimated density matrices for all input single- and two-qubit states when the NDES was turned on and then when it was turned off for reference. Then we used the NDES to directly measure the fidelity (overlap) in the nondestructive fashion.

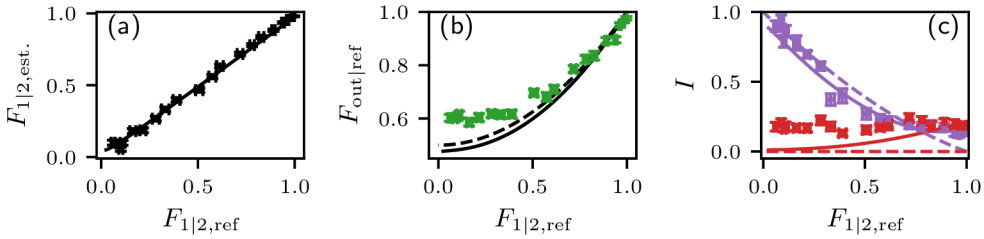

Figure 6.13: Overlap of target qubits. The shared horizontal axis $F_{1|2,\mathrm{ref}}$ corresponds to the respective fidelity between the reference target qubits, estimated from density matrices measured with NDES off. The dashed lines represent values given by the ideal theory, the solid lines give values obtained by simulation using the reconstructed process matrix, and the points denote measured experimental data. (a) Black circles mark the overlap of a and b directly measured by the nondemolition measurement. (b) Green markers show the out-ref-fidelity of the joint two-qubit system. (c) Quantum mutual information of the joint state of the target qubits. The red color corresponds to the reference (NDES off), purple to the output (NDES on). The error bars correspond to one standard deviation.

Our findings are summarized in Fig. 6.13, where we compared the values obtained by the measurement of the control qubit with the values obtained by ideal theoretical calculation and simulation employing the process matrix of the operation. The direct measurement closely follows the results obtained by tomography. Fig. 6.13 (a) shows the fidelity between the target qubits, $F_{1|2}$. Panel (b) shows the out-ref-fidelity of the joint two-qubit system, $F_{\mathrm{out}|\mathrm{ref}}$. We can see that the severity of the measurement back-action increases when the states are more distinct. The output two-qubit state is barely altered for identical input states, and the fidelity approaches unity. On the other hand, in the case of

orthogonal states on input, the measurement produces a balanced mixture of Bell states $\frac{1}{\sqrt{2}}(|01\rangle \pm |10\rangle)$, and the fidelity drops to 1/2. This demonstrates that the overlap measurement, while still nondestructive, influences the measured qubits.

This behavior can be analyzed in greater detail by looking at the correlations the NDES creates between the target qubits. Fig. 6.13 (b) shows the average mutual information between the two qubits. This quantity, which disregards the knowledge about which of the two projections has been performed, shows that the output states are most correlated when the input qubits were orthogonal, and the correlations diminish with increasing overlap of the two qubits until they vanish for identical states as predicted by the theory. We can also see that in the reference case when the NDES is off, the correlations are small but nonzero. This is again a consequence of the previously discussed experimental imperfections in the hyperencoding.

Let us note that the $F_{1|2}$ values on the x-axis are not uniformly sampled because $F_{1|2,\mathrm{ref}}$ is not our nominal choice, we nominally choose parameter α. Moreover, the values were determined experimentally and due to the various imperfections in preparation and the gate, the prepared state might be altered. The points cluster near the value $F_{1|2,\mathrm{ref}} \approx 0.1$ is the most visible manifestation of this problem.

NDES can also directly measure the fidelity between a pure and a mixed state. To test this, we have prepared the second target qubit as a mixture of $|0\rangle$ and the maximally mixed state and measured its fidelity with the state of the first target qubit, which was prepared either in $|1\rangle$ or in $|+\rangle$. We have repeated the measurement for different purities of the second target qubit. The measured fidelity between the target qubits is shown in Fig. 6.14 (a). In Fig. 6.14 (b), we evaluate the back action of the measurement by comparing the out-ref-fidelities of the individual target qubits. Fig. 6.14 (c) depicts the changes in the mutual information. The experimental results follow the theoretical predictions.

6.3.3 Hilbert-Schmidt distance measurement

With direct measurement of overlap $\mathrm{Tr}[\rho_1\rho_2]$ and purity $\mathrm{Tr}[\rho_1^2]$, it is also possible to directly measure the Hilbert-Schmidt distance of two density matrices $D = \frac{1}{2}\mathrm{Tr}[(\rho_1 - \rho_2)^\dagger(\rho_1 - \rho_2)]$ [181]. It comes from the identity

$$\mathrm{Tr}[(\rho_1 - \rho_2)^2] = \mathrm{Tr}\rho_1^2 + \mathrm{Tr}\rho_2^2 - 2\mathrm{Tr}[\rho_1\rho_2], \tag{6.10}$$

where the first two terms on the right-hand side are purities of the measured states and the last term is their overlap. Ideally, one could measure first the purities nondestructively and without perturbing the states, and after that, measure their overlap. Unfortunately, this would require more instances of NDES or quantum memory. In our test, we instead measured both purities and the overlap sequentially. This approach is still easier than the state tomography of both states.

First, we prepared the target qubits in all combinations of Pauli operator's eigenstates and measured D. We compare the measured results (a) with the ideal theory (c) in Fig. 6.15. We also prepared the first target in state $|0\rangle$ and mixed it with a maximally mixed state

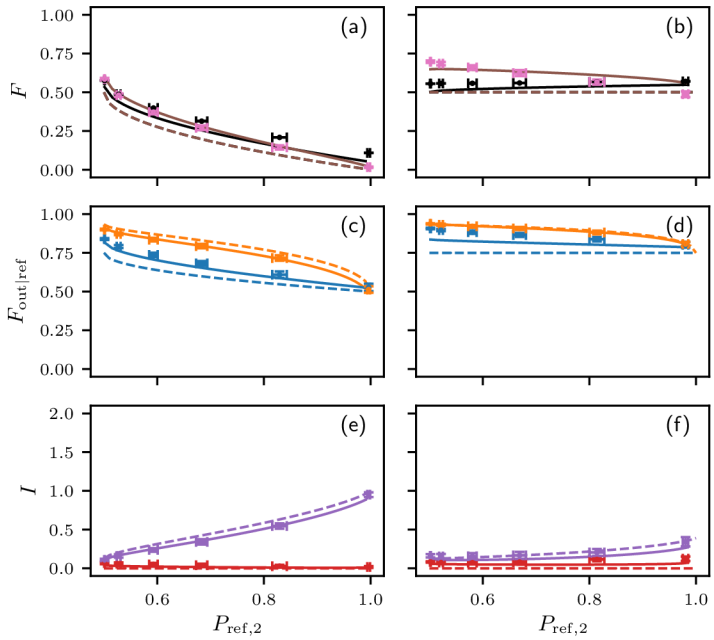

Figure 6.14: Measurement of the fidelity between a pure state and a mixed state. Left (a,c,e) and right (b,d,f) columns illustrate cases with the first target qubit set to $|1\rangle$ and $|+\rangle$, respectively. All graphs illustrate the dependence of observed quantities on the second target qubit's purity $P_{2,\mathrm{ref}}$. All dashed lines are ideal theoretical predictions, while all solid lines are predictions based on the reconstructed process matrix. In panels (a,b), we compare directly measured respective fidelity $F_{1|2}$ of target qubits (black markers) with fidelity $F_{1|2,\mathrm{ref}}$ calculated from the reconstructed reference density matrices, with the NDES turned off (pink markers). Panels (c,d) show single-qubit out-ref-fidelity for the first (blue markers) and second (orange markers) target qubit. Panels (e, f) depict the quantum mutual information I for the NDES on (black dots) and off (gray squares). The error bars correspond to one standard deviation obtained by bootstrapping on 100 samples.

to have the nominal purity P_1. Similarly, we prepared the second target qubit with the nominal purity P_2. We sampled the corresponding mixing factor uniformly for each qubit and measured D. Panel (b) in Fig. 6.15 shows the experimental data while panel (d) is the ideal theoretical outcome. Although results are systematically lower than the expected theory, due to the experimental imperfections, the structure of data agrees with the theory.

6.3.4 Qubit purification

Due to its nondestructive nature, the NDES can also be used to realize the *quantum purification* protocol [188, 189]. This protocol aims to improve the quality of quantum states affected by decoherence. For qubits, the input states can be given as $\rho_{in} = \Gamma(\psi; p)$, where $\Gamma(\psi; p) = p|\psi\rangle\langle\psi| + (1-p)\mathbb{1}_2\frac{1}{2}$. Through the purification operation, several copies of a partially mixed state are converted into fewer copies exhibiting higher purity, expressed by $\Gamma(\psi; p)^{\otimes n_1} \to \Gamma(\psi; p')^{\otimes n_2}$ with $p' > p$ and $n_1 > n_2$. In our realization, we used two identical copies of a partially mixed quantum state as input states of the target qubits. We again

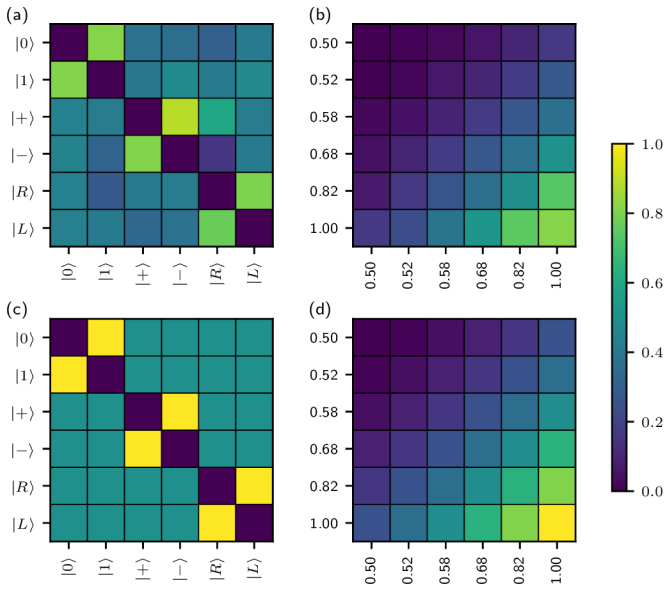

Figure 6.15: Measurement of Hilbert-Schmidt distance D. (a,c) Both qubits are prepared in a pure state. The state of the first (second) target qubit is denoted by the corresponding row (column) label. (b,d) Both target qubits are prepared in state $|0\rangle$, but they are individually mixed with a maximally mixed state. The first (second) target qubit's resulting purity is denoted by the corresponding row (column). The selected purities are not uniformly sampled, but the corresponding nominal mixing factor is. Panels (a,b) are related to the measured data, while panels (c,d) present the theoretical expectations. Color-coding represents the value of the distance.

used the six eigenstates of Pauli operators as a testing set. Post-selection of '+' results on the control qubit selects the projection onto the symmetric subspace and the resulting purity should increase. We performed quantum state tomography of the post-selected target qubits. As a reference, we use the reconstruction that we previously measured with NDES off. Actually, the data were already obtained during the direct purity measurement and all we had to do was to select the right subset from the whole using the method described in Section 3.3.1.

Fig. 6.16 (a,b) demonstrates improvement in purity of both target qubits. Panels (c,d) illustrate the fidelity increase of the output state related to its pure version. It means that the protocol increases the purity of the state while not changing the eigenstate of maximal eigenvalue.

6.3.5 Approximate qubit cloning

The active projection onto the symmetrical subspace can also be used to implement optimal quantum cloning [190–192]. Quantum cloning is a protocol that takes one or more copies of an unknown quantum state $|\psi\rangle$ and creates a higher number of copies. Such copies are always imperfect and their quality diminishes with their number. In our case, we have created two clones of a single unknown pure quantum state realizing transforma-

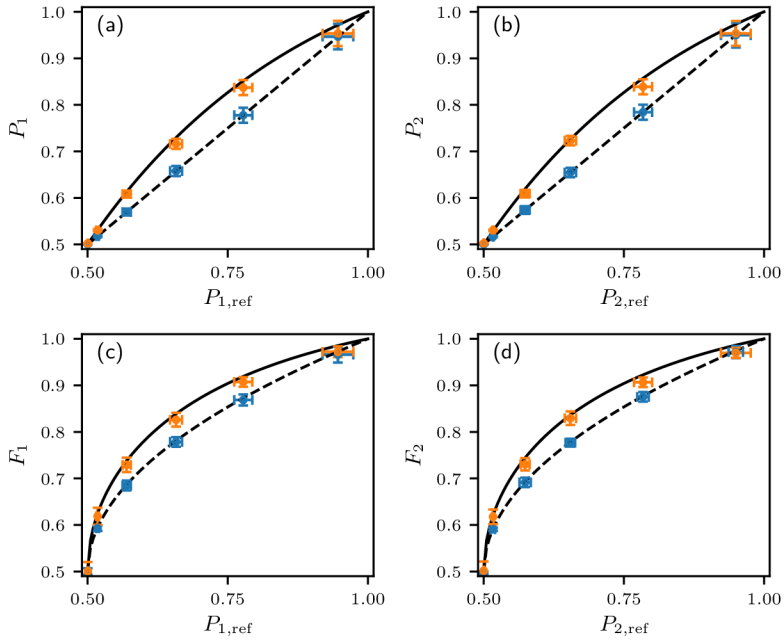

Figure 6.16: Purity (a,b) and fidelity (c,d) the first (a,c) and second (b,d) target qubit. Fidelity is related to the pure version of the measured state. The blue color indicates the reference situation before the purification that was obtained with NDES off. The orange color represents the situation after purification. Error bars indicate one standard deviation obtained from the set of six tested states.

tion $|\psi\rangle \rightarrow \frac{2}{3}|\psi\rangle\langle\psi| \otimes |\psi\rangle\langle\psi| + \frac{1}{3}|S\rangle\langle S|$, where $|S\rangle = \frac{1}{\sqrt{2}}(|\psi\rangle|\psi^{\perp}\rangle + |\psi^{\perp}\rangle|\psi\rangle)$ is the symmetric superposition of the initial state and the state orthogonal to it. The state of one target qubit can be cloned when the other target qubit is initialized in the maximally mixed state, and the NDES is used to probabilistically project two qubits onto the symmetric subspace [193]. We have realized the operation for the six eigenstates of Pauli operators and used tomographic reconstruction to characterize the two clones.

In Fig. 6.17 (a), we compare the clones to the input state to be copied. Due to the experimental imperfections, the cloner is not entirely symmetric and is slightly sensitive to the input state. Still, average clone fidelities are $\bar{F}_1 = 0.81(4)$ and $\bar{F}_2 = 0.80(3)$, significantly above the classical threshold of 2/3. The values approach the optimal theoretical limit of 5/6. The number in parenthesis represents one standard deviation obtained from the set of tested inputs. For reference, we also plot in Fig. 6.17 (b) the fidelity of the clones related to the theoretically expected output of the approximate cloner. The fidelity is close to one, reporting that the output states agree with our theoretical expectations. These results are comparable to the previous realizations of quantum cloning [194, 195].

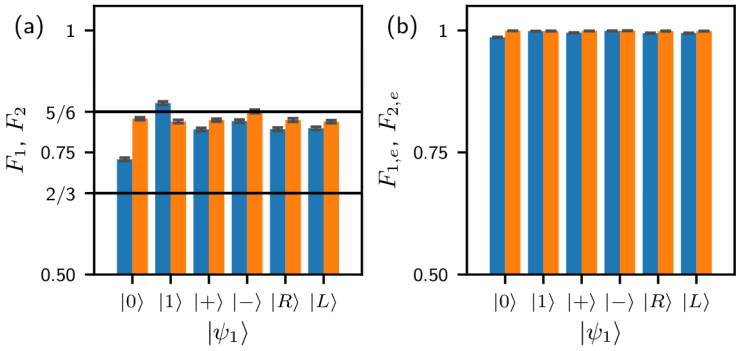

Figure 6.17: Quantum cloning. Fidelity F_1 of the first (blue) and fidelity F_2 of the second (orange) target qubit. The cloning fidelity is related to (a) the state to be copied and (b) the expected theoretical state of the imperfect clone. The fidelity is plotted for each of the tested input states. The barely visible error bar represents three standard deviations obtained by bootstrapping.

6.3.6 Programmable quantum multimeter

Von Neumann's projective measurement of a qubit can be realized in an arbitrary basis given by orthogonal states $|b\rangle$ and $|b_\perp\rangle$. Quantum multimeter is a device with the ambition to implement the full set of such measurements while controlling the measurement basis by a finite programmable quantum register. This makes them usable as a part of a larger quantum processing circuit. It is impossible to construct a deterministic multimeter performing arbitrary measurement controlled by a finite quantum state [183]. It comes from the fact that each distinct unitary transformation implemented by a deterministic quantum gate array requires increasing the dimension of the program state. Because the set of all unitary operations is infinite, the finite program register is not enough [196]. It was shown in [184] that when the signal and the program are single qubits, the optimal approximate scheme is based on the projection into the symmetric and antisymmetric subspaces.

We have used our controlled exchange interaction to implement a nondestructive quantum multimeter for unknown signal state $|a\rangle$ of the first target qubit, which is programmed by the quantum state $|b\rangle$ of the other target qubit. The control qubit, initially prepared in quantum state $|+\rangle$, has been used to read out the measurement result. Measurement outcomes '+' or '-' can be interpreted as an indication that qubit a was found most likely in state $|b\rangle$ or $|b_\perp\rangle$, respectively. The POVM elements corresponding to these measurement results are

$$\Pi_+ = |b\rangle\langle b| + \frac{1}{2}|b_\perp\rangle\langle b_\perp|, \quad \Pi_- = \frac{1}{2}|b_\perp\rangle\langle b_\perp|. \tag{6.11}$$

The quality of the measurement can be evaluated with the help of the conditional probabilities $p(x|y)$, which represent the probability that measurement of control qubit returned value x when the initial state of the first target qubit was $|y\rangle$. In our case $x = \pm$ and $|y\rangle = |a\rangle$ or $|a^\perp\rangle$. These conditional probabilities generally depend on the overlap $F_{1|2,\mathrm{ref}} = |\langle a|b\rangle|^2$ between the signal and the program state.

The natural way to benchmark the quality of the experimental quantum multimeter is by evaluating its performance as a quantum discriminator [183, 184]. In this regime, in which we attempt to discriminate between known orthogonal states $|a\rangle$ and $|a_\perp\rangle$ appearing with equal probabilities, the program qubit is prepared in state $|b\rangle = |a\rangle$. The quality of the discriminator can be quantified by the *discrimination fidelity* [184]:

$$F_{\text{disc}} = \frac{1}{2}\left[p(+|a) + p(-|a_\perp)\right], \tag{6.12}$$

which should be, up to experimental imperfections, equal to 3/4.

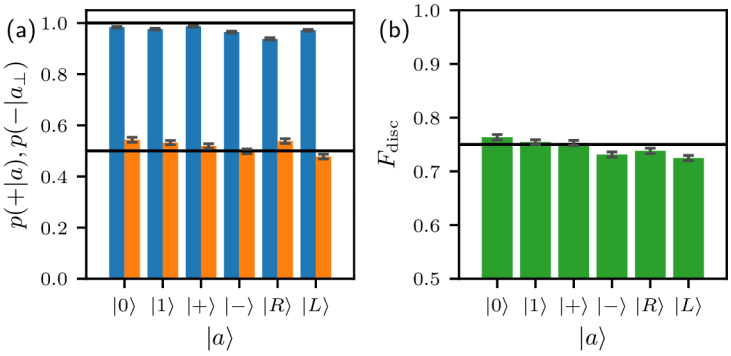

Figure 6.18: Quantum multimeter used as a state discriminator. (a) The conditional probability of outcome '+' in the presence of state $|a\rangle$ (blue) and outcome '+' in the presence of state $|a_\perp\rangle$ (orange). (b) The discrimination fidelity. All quantities are plotted for six tested input states. The black line denotes theoretical discrimination fidelity 3/4. Error bars represent one standard deviation. We obtained them from measured count rates by error-propagation with an assumption of Poisson statistics.

We have experimentally tested the multimeter for the same six testing states as before. Using these six states as probes and projecting states, we recorded a process tomogram of a NDES device on and off. From the measured counts, we directly estimated the probabilities

$$p(+|a) = \frac{C_{a,+}}{C_{a,+} + C_{a,-}},$$

$$p(-|a_\perp) = \frac{C_{a\perp,-}}{C_{a\perp,+} + C_{a\perp,-}},$$

where $C_{a,i,\pm}$ is the total number of coincidences in state tomogram corresponding to input $|a\rangle$ post-selected to control qubit outcome $\pm$. We obtained a statistical error by error-propagation assuming Poisson statistics of coincidence counts. The measured probabilities $p(+|a)$ and $p(-|a_\perp)$ are plotted in Fig. 6.18 (a) with blue and orange bars, respectively. The corresponding discrimination fidelity is plotted in panel (b). Although the discrimination fidelities are slightly unequal, their average over the six separate settings is $\bar{F}_{\text{disc}} = 0.74(1)$. We therefore conclude that the measured value agrees well with the theoretical predictions.

The multimeter is nondestructive, but it still introduces correlations between the signal and the program, which diminishes the single-qubit qualities. The extent to which this

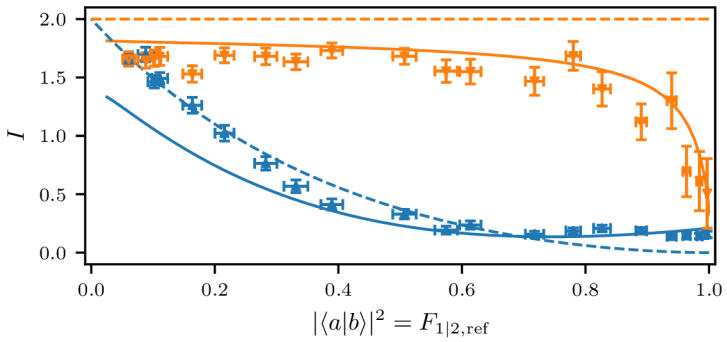

Figure 6.19: Mutual quantum information of the output system. Blue color corresponds to successful projection onto a symmetric subspace, while the orange color corresponds to successful projection onto an antisymmetric subspace. Solid lines are the predictions based on the measured process matrix, and dashed lines represent the ideal theoretical predictions.

happens depends on their overlap and it can be evaluated with the help of mutual information I, which is depicted in Fig. 6.19 (c). The situation is different for each of the two possible measurement results, '+' and '−'. The measurement result '−' corresponding to the projection onto the antisymmetric subspace produces a two-qubit state with maximal mutual information as long as the qubit states differ. When the qubits are in identical states, the projection never succeeds, which manifests as a discontinuity in the theoretical description. In the experimental reality, however, the reduction of the probability of success leads to larger measurement errors together with higher sensitivity to experimental imperfections. This causes the drop of correlations between highly overlapping states. Nevertheless, this situation leads to qubits that are individually in the maximally mixed state and unsuitable for further processing. On the other hand, correlations introduced by the measurement result '+' are generally lower. As a consequence, both the signal and the program qubits can be recovered with average theoretical fidelity $\overline{F}_{\mathrm{th}} = 0.793$. In our experiment, we managed to obtain fidelities $\overline{F}_a = 0.761$ and $\overline{F}_b = 0.809$, respectively.

Chapter 7

Summary

The goal of this thesis, and my Ph.D. program, was to construct and apply the three quantum logic gates, namely four-qubit controlled-Z gate, three-qubit controlled-phase gate, and a Fredkin gate. We realized these gates with linear-quantum optic, using two-photon interference and encoding multiple quantum bits into a single photon. My contribution is explained in Preface. After a short presentation of the context of the work, I described the key concepts and used experimental methods. Then the three gates and their applications follow, each in its chapter.

With the four-qubit controlled-Z gate described in Chapter 4, we showed how to characterize multi-qubit gates of a similar scale experimentally. We estimated the quantum process fidelity using Monte-Carlo sampling and Hofmann bounds. Then we showed that the four-qubit CZ gate could support two logical qubits, each encoded in two physical qubits, and operate as the two-qubit controlled-Z gate in decoherence-free subspace. Our results indicate that the implemented quantum gate was resilient to collective dephasing acting on the physical qubits. Such resilience could be helpful in applications where the used communication channels are influenced by the noise evenly.

With the second implemented quantum gate, the three-qubit controlled-phase gate, we remained on the topic of decoherence protection. Let us remark that the previously constructed controlled-Z gate served as a core for the controlled-phase gate. Once we built and characterized the gate, we used it as a simulator of the decoherence mechanism. With such a simulator, we tested another protocol for decoherence protection. A single qubit simulated the environment, and the phase gate represented system-environment coupling. Our results experimentally verify that we can use suitable measurement on an auxiliary qubit and the decoherence-responsible interaction to turn the environment into a dark state, in which the decoherence is turned off. The protocol has its potential application in qubits that are coupled to a small neighboring quantum system.

The last presented gate is the quantum Fredkin gate, which conditionally swaps two target qubits. Another qubit controls the swapping. The construction relies on two swap gates to exchange path and polarization qubits. The swap gate is discussed as an intermediate result. Let us remark that our implementation differs from the previously demonstrated implementations that required two pairs of entangled photons [138, 185]. Thanks

to the hyperencoding of qubits, we had a coincidence count rate high enough to easily perform numerous experiments and perform a full quantum process tomography of an optical quantum Fredkin gate for the first time. We applied the gate to experimentally demonstrate protocols that relied on symmetrization procedure, namely direct measurement of purity, overlap, Hilbert-Schmidt distance, purification and cloning of qubits, and performing quantum measurements controlled by another qubit. These experiments were already done earlier using the two-photon interference on a balanced beam-splitter, but this time we could access the measured quantum state after the symmetrization. We tomographically investigated the back-action of these measurements on the measured qubits.

Linear quantum optics in the KLM approach in the standard circuit model is difficult to scale up. Moreover, the hyperencoding forces us to interpret some of the obtained results as a photonic simulation of the implemented gates. Albeit these facts, the thesis showed that linear quantum optics still could serve as a valuable tool for experimental tests of various small-scale protocols and strategies in quantum information and communication.

I hope to use the know-how that I acquired during these experiments to test more interesting quantum information protocols and prepare more states with various exotic properties. I also believe that this thesis would help me transfer the acquired experience to anyone who would like to continue in this kind of experiment.

References

Articles covering the presented results

A1 R. Stárek, M. Mičuda, M. Miková, I. Straka, M. Dušek, M. Ježek, and J. Fiurášek:
"Experimental investigation of a four-qubit linear-optical quantum logic circuit,"
Scientific Reports **6**, 10.1038/srep33475 (2016).

A2 M. Mičuda, R. Stárek, J. Fiurášek, and R. Filip:
"Decoherence-resilient linear optical two-qubit quantum gate,"
Phys. Rev. Applied **14**, 054066 (2020).

A3 R. Stárek, M. Mičuda, M. Miková, I. Straka, M. Dušek, P. Marek, M. Ježek, R. Filip, and J. Fiurášek:
"Nondestructive detector for exchange symmetry of photonic qubits,"
npj Quantum Information **4**, 10.1038/s41534-018-0087-x (2018).

A4 R. Stárek, M. Miková, I. Straka, M. Dušek, M. Ježek, J. Fiurášek, and M. Mičuda:
"Experimental realization of SWAP operation on hyper-encoded qubits,"
Optics Express **26**, 8443 (2018).

A5 R. Stárek, M. Mičuda, I. Straka, M. Nováková, M. Dušek, M. Ježek, J. Fiurášek, and R. Filip:
"Experimental quantum decoherence control by dark states of the environment,"
New Journal of Physics **22**, 093058 (2020).

Books

B1 M. Nielsen and I. Chuang:
Quantum computation and quantum information: 10th anniversary edition,
(Cambridge University Press, 2010).

B2 E. Cheney and D. Kincaid:
Linear algebra: theory and applications,
(Jones and Bartlett Publishers, 2009).

Articles, proceedings and theses

1 I. Straka:
"Generation, detection and characterization of photonic quantum states,"
PhD thesis (Palacky University Olomouc, 2019).

2 M. Mičuda, M. Miková, I. Straka, M. Sedlák, M. Dušek, M. Ježek, and J. Fiurášek:
"Tomographic characterization of a linear optical quantum toffoli gate,"
Phys. Rev. A **92**, 032312 (2015).

3 M. Novaková:
"Quantum optical experiments focused on quantum information processing,"
PhD thesis (Palacky University Olomouc, 2017).

4 R. P. Feynman:
"Simulating physics with computers,"
International Journal of Theoretical Physics **21**, 467–488 (1982).

5 D. Deutsch and R. Penrose:
"Quantum theory, the church;turing principle and the universal quantum computer,"
Proceedings of the Royal Society of London. A. Mathematical and Physical Sciences **400**, 97–117 (1985).

6 D. Deutsch and R. Jozsa:
"Rapid solution of problems by quantum computation,"
Proceedings of the Royal Society of London. Series A: Mathematical and Physical Sciences **439**, 553–558 (1992).

7 P. W. Shor:
"Algorithms for quantum computation: discrete logarithms and factoring,"
in Proceedings 35th annual symposium on foundations of computer science (1994), pp. 124–134.

8 D. P. DiVincenzo:
"The physical implementation of quantum computation,"
Fortschritte der Physik **48**, 771–783 (2000).

9 F. Arute et al.:
"Quantum supremacy using a programmable superconducting processor,"
Nature **574**, 505–510 (2019).

10 Y. Wu et al.:
"Strong quantum computational advantage using a superconducting quantum processor,"
Phys. Rev. Lett. **127**, 180501 (2021).

11 M. Kliesch and I. Roth:
"Theory of quantum system certification,"
PRX Quantum **2**, 010201 (2021).

12 T. Proctor, K. Rudinger, K. Young, E. Nielsen, and R. Blume-Kohout:
"Measuring the capabilities of quantum computers,"
Nature Physics, 10.1038/s41567-021-01409-7 (2021).

13 J. S. Lundeen, B. Sutherland, A. Patel, C. Stewart, and C. Bamber:
"Direct measurement of the quantum wavefunction,"
Nature **474**, 188–191 (2011).

14 J. S. Lundeen and C. Bamber:
"Procedure for direct measurement of general quantum states using weak measurement,"
Phys. Rev. Lett. **108**, 070402 (2012).

15 G. S. Thekkadath, L. Giner, Y. Chalich, M. J. Horton, J. Banker, and J. S. Lundeen:
"Direct measurement of the density matrix of a quantum system,"
Phys. Rev. Lett. **117**, 120401 (2016).

16 L. Calderaro, G. Foletto, D. Dequal, P. Villoresi, and G. Vallone:
"Direct reconstruction of the quantum density matrix by strong measurements,"
Phys. Rev. Lett. **121**, 230501 (2018).

17 D. Gross, Y.-K. Liu, S. T. Flammia, S. Becker, and J. Eisert:
"Quantum state tomography via compressed sensing,"
Phys. Rev. Lett. **105**, 150401 (2010).

18 A. Shabani, R. L. Kosut, M. Mohseni, H. Rabitz, M. A. Broome, M. P. Almeida, A. Fedrizzi, and A. G. White:
"Efficient measurement of quantum dynamics via compressive sensing,"
Phys. Rev. Lett. **106**, 100401 (2011).

19 G. Tóth, W. Wieczorek, D. Gross, R. Krischek, C. Schwemmer, and H. Weinfurter:
"Permutationally invariant quantum tomography,"
Phys. Rev. Lett. **105**, 250403 (2010).

20 T. Moroder, P. Hyllus, G. Tóth, C. Schwemmer, A. Niggebaum, S. Gaile, O. Gühne, and H. Weinfurter:
"Permutationally invariant state reconstruction,"
New Journal of Physics **14**, 105001 (2012).

21 Y. S. Teo, H. Zhu, B.-G. Englert, J. Řeháček, and Z. Hradil:
"Quantum-state reconstruction by maximizing likelihood and entropy,"
Phys. Rev. Lett. **107**, 020404 (2011).

22 H. F. Hofmann:
"Complementary classical fidelities as an efficient criterion for the evaluation of experimentally realized quantum operations,"
Phys. Rev. Lett. **94**, 160504 (2005).

23 J. Emerson, M. Silva, O. Moussa, C. Ryan, M. Laforest, J. Baugh, D. G. Cory, and R. Laflamme:
"Symmetrized characterization of noisy quantum processes,"
Science **317**, 1893–1896 (2007).

24 S. T. Flammia and Y.-K. Liu:
"Direct fidelity estimation from few pauli measurements,"
Phys. Rev. Lett. **106**, 230501 (2011).

25 M. P. da Silva, O. Landon-Cardinal, and D. Poulin:
"Practical characterization of quantum devices without tomography,"
Phys. Rev. Lett. **107**, 210404 (2011).

26 L. Steffen, M. P. da Silva, A. Fedorov, M. Baur, and A. Wallraff:
"Experimental monte carlo quantum process certification,"
Phys. Rev. Lett. **108**, 260506 (2012).

27 D. M. Reich, G. Gualdi, and C. P. Koch:
"Minimum number of input states required for quantum gate characterization,"
Phys. Rev. A **88**, 042309 (2013).

28 Y. Zhou, E. M. Stoudenmire, and X. Waintal:
"What limits the simulation of quantum computers?"
Phys. Rev. X **10**, 041038 (2020).

29 C. H. Bennett and G. Brassard:
"Quantum cryptography: public key distribution and coin tossing,"
Theoretical Computer Science **560**, Theoretical Aspects of Quantum Cryptography – celebrating 30 years of BB84, 7–11 (2014).

30 S.-K. Liao et al.:
"Satellite-relayed intercontinental quantum network,"
Phys. Rev. Lett. **120**, 030501 (2018).

31 J.-P. Chen et al.:
"Sending-or-not-sending with independent lasers: secure twin-field quantum key distribution over 509 km,"
Phys. Rev. Lett. **124**, 070501 (2020).

32 X. Ma, X. Yuan, Z. Cao, B. Qi, and Z. Zhang:
"Quantum random number generation,"
npj Quantum Information **2**, 10.1038/npjqi.2016.21 (2016).

33 J. Aasi et al.:
"Enhanced sensitivity of the ligo gravitational wave detector by using squeezed states of light,"
Nature Photonics **7**, 613–619 (2013).

34 O. Hosten and P. Kwiat:
"Observation of the spin hall effect of light via weak measurements,"
Science **319**, 787–790 (2008).

35 R. Stárek, M. Mičuda, R. Hošák, M. Ježek, and J. Fiurášek:
"Experimental entanglement-assisted weak measurement of phase shift,"
Opt. Express **28**, 34639–34655 (2020).

36 R. Amiri, R. Stárek, D. Reichmuth, I. V. Puthoor, M. Mi čuda, L. Mi šta Jr., M. Du šek, P. Wallden, and E. Andersson:
"Imperfect 1-out-of-2 quantum oblivious transfer: bounds, a protocol, and its experimental implementation,"
PRX Quantum **2**, 010335 (2021).

37 M. Mičuda, R. Stárek, J. Provazník, O. Leskovjanová, and L. Mišta:
"Verifying genuine multipartite entanglement of the whole from its separable parts,"
Optica **6**, 896–901 (2019).

38 E. Knill, R. Laflamme, and G. J. Milburn:
"A scheme for efficient quantum computation with linear optics,"
Nature **409**, 46–52 (2001).

39 C. K. Hong, Z. Y. Ou, and L. Mandel:
"Measurement of subpicosecond time intervals between two photons by interference,"
Phys. Rev. Lett. **59**, 2044–2046 (1987).

40 M. Koashi, T. Yamamoto, and N. Imoto:
"Probabilistic manipulation of entangled photons,"
Physical Review A **63**, 10.1103/physreva.63.030301 (2001).

41 P. Kok et al.:
"Linear optical quantum computing with photonic qubits,"
Rev. Mod. Phys. **79**, 135–174 (2007).

42 T. B. Pittman, B. C. Jacobs, and J. D. Franson:
"Demonstration of nondeterministic quantum logic operations using linear optical elements,"
Phys. Rev. Lett. **88**, 257902 (2002).

43 J. L. O'Brien, G. J. Pryde, A. G. White, T. C. Ralph, and D. Branning:
"Demonstration of an all-optical quantum controlled-NOT gate,"
Nature **426**, 264–267 (2003).

44 S. Gasparoni, J.-W. Pan, P. Walther, T. Rudolph, and A. Zeilinger:
"Realization of a photonic controlled-not gate sufficient for quantum computation,"
Phys. Rev. Lett. **93**, 020504 (2004).

45 N. Kiesel, C. Schmid, U. Weber, R. Ursin, and H. Weinfurter:
"Linear optics controlled-phase gate made simple,"
Phys. Rev. Lett. **95**, 210505 (2005).

46 N. K. Langford, T. J. Weinhold, R. Prevedel, K. J. Resch, A. Gilchrist, J. L. O'Brien, G. J. Pryde, and A. G. White:
"Demonstration of a simple entangling optical gate and its use in bell-state analysis,"
Phys. Rev. Lett. **95**, 210504 (2005).

47 R. Okamoto, H. F. Hofmann, S. Takeuchi, and K. Sasaki:
"Demonstration of an optical quantum controlled-not gate without path interference,"
Phys. Rev. Lett. **95**, 210506 (2005).

48 Z. Zhao, A.-N. Zhang, Y.-A. Chen, H. Zhang, J.-F. Du, T. Yang, and J.-W. Pan:
"Experimental demonstration of a nondestructive controlled-not quantum gate for two independent photon qubits,"
Phys. Rev. Lett. **94**, 030501 (2005).

49 R. Raussendorf and H. J. Briegel:
"A one-way quantum computer,"
Phys. Rev. Lett. **86**, 5188–5191 (2001).

50 M. A. Nielsen:
"Optical quantum computation using cluster states,"
Phys. Rev. Lett. **93**, 040503 (2004).

51 P. Walther, K. J. Resch, T. Rudolph, E. Schenck, H. Weinfurter, V. Vedral, M. Aspelmeyer, and A. Zeilinger:
"Experimental one-way quantum computing,"
Nature **434**, 169–176 (2005).

52 T. C. Ralph, A. Gilchrist, G. J. Milburn, W. J. Munro, and S. Glancy:
"Quantum computation with optical coherent states,"
Phys. Rev. A **68**, 042319 (2003).

53 A. Gilchrist, K. Nemoto, W. J. Munro, T. C. Ralph, S. Glancy, S. L. Braunstein, and G. J. Milburn:
"Schrödinger cats and their power for quantum information processing,"
Journal of Optics B: Quantum and Semiclassical Optics **6**, S828–S833 (2004).

54 L. S. Costanzo, A. S. Coelho, N. Biagi, J. Fiurášek, M. Bellini, and A. Zavatta:
"Measurement-induced strong kerr nonlinearity for weak quantum states of light,"
Phys. Rev. Lett. **119**, 013601 (2017).

55 A. Reiserer and G. Rempe:
"Cavity-based quantum networks with single atoms and optical photons,"
Rev. Mod. Phys. **87**, 1379–1418 (2015).

56 L.-M. Duan and H. J. Kimble:
"Scalable photonic quantum computation through cavity-assisted interactions,"
Phys. Rev. Lett. **92**, 127902 (2004).

57 B. Hacker, S. Welte, G. Rempe, and S. Ritter:
"A photon–photon quantum gate based on a single atom in an optical resonator,"
Nature **536**, 193–196 (2016).

58 E. Urban, T. A. Johnson, T. Henage, L. Isenhower, D. D. Yavuz, T. G. Walker, and M. Saffman:
"Observation of rydberg blockade between two atoms,"
Nature Physics **5**, 110–114 (2009).

59 A. V. Gorshkov, J. Otterbach, M. Fleischhauer, T. Pohl, and M. D. Lukin:
"Photon-photon interactions via rydberg blockade,"
Phys. Rev. Lett. **107**, 133602 (2011).

60 S. Baur, D. Tiarks, G. Rempe, and S. Dürr:
"Single-photon switch based on rydberg blockade,"
Phys. Rev. Lett. **112**, 073901 (2014).

61 D. Tiarks, S. Schmidt-Eberle, T. Stolz, G. Rempe, and S. Dürr:
"A photon–photon quantum gate based on rydberg interactions,"
Nature Physics **15**, 124–126 (2018).

62 C.-Y. Lu, D. E. Browne, T. Yang, and J.-W. Pan:
"Demonstration of a compiled version of shor's quantum factoring algorithm using photonic qubits,"
Phys. Rev. Lett. **99**, 250504 (2007).

63 M. Reck, A. Zeilinger, H. J. Bernstein, and P. Bertani:
"Experimental realization of any discrete unitary operator,"
Phys. Rev. Lett. **73**, 58–61 (1994).

64 N. J. Cerf, C. Adami, and P. G. Kwiat:
"Optical simulation of quantum logic,"
Phys. Rev. A **57**, R1477–R1480 (1998).

65 B. P. Lanyon, M. Barbieri, M. P. Almeida, T. Jennewein, T. C. Ralph, K. J. Resch, G. J. Pryde, J. L. O'Brien, A. Gilchrist, and A. G. White:
"Simplifying quantum logic using higher-dimensional hilbert spaces,"
Nature Physics **5**, 134–140 (2008).

66 M. Mičuda, M. Sedlák, I. Straka, M. Miková, M. Dušek, M. Ježek, and J. Fiurášek:
"Efficient experimental estimation of fidelity of linear optical quantum toffoli gate,"
Phys. Rev. Lett. **111**, 160407 (2013).

67 D. C. Burnham and D. L. Weinberg:
"Observation of simultaneity in parametric production of optical photon pairs,"
Phys. Rev. Lett. **25**, 84–87 (1970).

68 P. G. Kwiat, K. Mattle, H. Weinfurter, A. Zeilinger, A. V. Sergienko, and Y. Shih:
"New high-intensity source of polarization-entangled photon pairs,"
Phys. Rev. Lett. **75**, 4337–4341 (1995).

69 M. M. Weston, H. M. Chrzanowski, S. Wollmann, A. Boston, J. Ho, L. K. Shalm, V. B. Verma, M. S. Allman, S. W. Nam, R. B. Patel, S. Slussarenko, and G. J. Pryde:
"Efficient and pure femtosecond-pulse-length source of polarization-entangled photons,"
Opt. Express **24**, 10869–10879 (2016).

70 B. L. Glebov, J. Fan, and A. Migdall:
"Deterministic generation of single photons via multiplexing repetitive parametric downconversions,"
Applied Physics Letters **103**, 031115 (2013).

71 J. Tang, L. Tang, H. Wu, Y. Wu, H. Sun, H. Zhang, T. Li, Y. Lu, M. Xiao, and K. Xia:
"Towards on-demand heralded single-photon sources via photon blockade,"
Phys. Rev. Applied **15**, 064020 (2021).

72 M. Halder, A. Beveratos, R. T. Thew, C. Jorel, H. Zbinden, and N. Gisin:
"High coherence photon pair source for quantum communication,"
New Journal of Physics **10**, 023027 (2008).

73 A. Fedrizzi, T. Herbst, A. Poppe, T. Jennewein, and A. Zeilinger:
"A wavelength-tunable fiber-coupled source of narrowband entangled photons,"
Opt. Express **15**, 15377–15386 (2007).

74 J. S. Neergaard-Nielsen, B. M. Nielsen, H. Takahashi, A. I. Vistnes, and E. S. Polzik:
"High purity bright single photon source,"
Opt. Express **15**, 7940–7949 (2007).

75 F. Kaneda and P. G. Kwiat:
"High-efficiency single-photon generation via large-scale active time multiplexing,"
Science Advances **5**, 10.1126/sciadv.aaw8586 (2019).

76 W. Wieczorek, R. Krischek, N. Kiesel, P. Michelberger, G. Tóth, and H. Weinfurter:
"Experimental entanglement of a six-photon symmetric dicke state,"
Phys. Rev. Lett. **103**, 020504 (2009).

77 X.-C. Yao, T.-X. Wang, P. Xu, H. Lu, G.-S. Pan, X.-H. Bao, C.-Z. Peng, C.-Y. Lu, Y.-A. Chen, and J.-W. Pan:
"Observation of eight-photon entanglement,"
Nature Photonics **6**, 225–228 (2012).

78 X.-L. Wang et al.:
"Experimental ten-photon entanglement,"
Phys. Rev. Lett. **117**, 210502 (2016).

79 H.-S. Zhong et al.:
"12-photon entanglement and scalable scattershot boson sampling with optimal entangled-photon pairs from parametric down-conversion,"
Phys. Rev. Lett. **121**, 250505 (2018).

80 L. J. Wang, C. K. Hong, and S. R. Friberg:
"Generation of correlated photons via four-wave mixing in optical fibres,"
Journal of Optics B: Quantum and Semiclassical Optics **3**, 346–352 (2001).

81 R. J. A. Francis-Jones, R. A. Hoggarth, and P. J. Mosley:
"All-fiber multiplexed source of high-purity single photons,"
Optica **3**, 1270–1273 (2016).

82 X. Guo, C.-l. Zou, C. Schuck, H. Jung, R. Cheng, and H. X. Tang:
"Parametric down-conversion photon-pair source on a nanophotonic chip,"
Light: Science & Applications **6**, e16249–e16249 (2016).

83 A. Beveratos, S. Kühn, R. Brouri, T. Gacoin, J.-P. Poizat, and P. Grangier:
"Room temperature stable single-photon source,"
The European Physical Journal D-Atomic, Molecular, Optical and Plasma Physics **18**, 191–196 (2002).

84 A. Sipahigil et al.:
"Quantum interference of single photons from remote nitrogen-vacancy centers in diamond,"
Phys. Rev. Lett. **108**, 143601 (2012).

85 S. Li, C.-H. Li, B.-W. Zhao, Y. Dong, C.-C. Li, X.-D. Chen, Y.-S. Ge, and F.-W. Sun:
"A bright single-photon source from nitrogen-vacancy centers in diamond nanowires,"
Chinese Physics Letters **34**, 096101 (2017).

86 F. De Martini, G. Di Giuseppe, and M. Marrocco:
"Single-mode generation of quantum photon states by excited single molecules in a microcavity trap,"
Physical review letters **76**, 900 (1996).

87 C. Brunel, B. Lounis, P. Tamarat, and M. Orrit:
"Triggered source of single photons based on controlled single molecule fluorescence,"
Physical Review Letters **83**, 2722 (1999).

88 B. Lounis and W. E. Moerner:
"Single photons on demand from a single molecule at room temperature,"
Nature **407**, 491–493 (2000).

89 R. Lettow, Y. L. A. Rezus, A. Renn, G. Zumofen, E. Ikonen, S. Götzinger, and V. Sandoghdar:
"Quantum interference of tunably indistinguishable photons from remote organic molecules,"
Phys. Rev. Lett. **104**, 123605 (2010).

90 K. G. Lee, X. W. Chen, H. Eghlidi, P. Kukura, R. Lettow, A. Renn, V. Sandoghdar, and S. Götzinger:
"A planar dielectric antenna for directional single-photon emission and near-unity collection efficiency,"
Nature Photonics **5**, 166–169 (2011).

91 D. Rattenbacher, A. Shkarin, J. Renger, T. Utikal, S. Götzinger, and V. Sandoghdar:
"Coherent coupling of single molecules to on-chip ring resonators,"
New Journal of Physics **21**, 062002 (2019).

92 J.-M. Gérard and B. Gayral:
"Strong purcell effect for inas quantum boxes in three-dimensional solid-state microcavities,"
Journal of lightwave technology **17**, 2089–2095 (1999).

93 P. Michler, A. Kiraz, C. Becher, W. Schoenfeld, P. Petroff, L. Zhang, E. Hu, and A. Imamoglu:
"A quantum dot single-photon turnstile device,"
science **290**, 2282–2285 (2000).

94 V. Zwiller, H. Blom, P. Jonsson, N. Panev, S. Jeppesen, T. Tsegaye, E. Goobar, M.-E. Pistol, L. Samuelson, and G. Björk:
"Single quantum dots emit single photons at a time: antibunching experiments,"
Applied Physics Letters **78**, 2476–2478 (2001).

95 C. Santori, M. Pelton, G. Solomon, Y. Dale, and Y. Yamamoto:
"Triggered single photons from a quantum dot,"
Physical Review Letters **86**, 1502 (2001).

96 C. Santori, D. Fattal, J. Vučković, G. S. Solomon, and Y. Yamamoto:
"Indistinguishable photons from a single-photon device,"
Nature **419**, 594–597 (2002).

97 Z. Yuan, B. E. Kardynal, R. M. Stevenson, A. J. Shields, C. J. Lobo, K. Cooper, N. S. Beattie, D. A. Ritchie, and M. Pepper:
"Electrically driven single-photon source,"
science **295**, 102–105 (2002).

98 M. Müller, H. Vural, C. Schneider, A. Rastelli, O. G. Schmidt, S. Höfling, and P. Michler:
"Quantum-dot single-photon sources for entanglement enhanced interferometry,"
Phys. Rev. Lett. **118**, 257402 (2017).

99 H. Wang, Y.-M. He, T.-H. Chung, H. Hu, Y. Yu, S. Chen, X. Ding, M.-C. Chen, J. Qin, X. Yang, R.-Z. Liu, Z.-C. Duan, J.-P. Li, S. Gerhardt, K. Winkler, J. Jurkat, L.-J. Wang, N. Gregersen, Y.-H. Huo, Q. Dai, S. Yu, S. Höfling, C.-Y. Lu, and J.-W. Pan:
"Towards optimal single-photon sources from polarized microcavities,"
Nature Photonics **13**, 770–775 (2019).

100 M. D. Eisaman, J. Fan, A. Migdall, and S. V. Polyakov:
"Invited review article: single-photon sources and detectors,"
Review of Scientific Instruments **82**, 071101 (2011).

101 P. Lodahl, S. Mahmoodian, and S. Stobbe:
"Interfacing single photons and single quantum dots with photonic nanostructures,"
Rev. Mod. Phys. **87**, 347–400 (2015).

102 M. Davanco, J. Liu, L. Sapienza, C.-Z. Zhang, J. V. D. M. Cardoso, V. Verma, R. Mirin, S. W. Nam, L. Liu, and K. Srinivasan:
"Heterogeneous integration for on-chip quantum photonic circuits with single quantum dot devices,"
Nature Communications **8**, 10.1038/s41467-017-00987-6 (2017).

103 J. Carolan et al.:
"Universal linear optics,"
Science **349**, 711–716 (2015).

104 F. Flamini, N. Spagnolo, and F. Sciarrino:
"Photonic quantum information processing: a review,"
Reports on Progress in Physics **82**, 016001 (2018).

105 A. Crespi, R. Ramponi, R. Osellame, L. Sansoni, I. Bongioanni, F. Sciarrino, G. Vallone, and P. Mataloni:
"Integrated photonic quantum gates for polarization qubits,"
Nature Communications **2**, 10.1038/ncomms1570 (2011).

106 G. Corrielli et al.:
"Rotated waveplates in integrated waveguide optics,"
Nature Communications **5**, 10.1038/ncomms5249 (2014).

107 A. Politi, M. J. Cryan, J. G. Rarity, S. Yu, and J. L. O'Brien:
"Silica-on-silicon waveguide quantum circuits,"
Science **320**, 646–649 (2008).

108 A. Politi, J. C. F. Matthews, and J. L. O'Brien:
"Shor's quantum factoring algorithm on a photonic chip,"
Science **325**, 1221–1221 (2009).

109 B. J. Metcalf, J. B. Spring, P. C. Humphreys, N. Thomas-Peter, M. Barbieri, W. S. Kolthammer, X.-M. Jin, N. K. Langford, D. Kundys, J. C. Gates, B. J. Smith, P. G. R. Smith, and I. A. Walmsley:
"Quantum teleportation on a photonic chip,"
Nature Photonics **8**, 770–774 (2014).

110 N. J. D. Martinez, M. Gehl, C. T. Derose, A. L. Starbuck, A. T. Pomerene, A. L. Lentine, D. C. Trotter, and P. S. Davids:
"Single photon detection in a waveguide-coupled ge-on-si lateral avalanche photodiode,"
Opt. Express **25**, 16130–16139 (2017).

111 S. Ferrari, C. Schuck, and W. Pernice:
"Waveguide-integrated superconducting nanowire single-photon detectors,"
Nanophotonics **7**, 1725–1758 (2018).

112 Z. Hradil, J. Řeháček, J. Fiurášek, and M. Ježek:
"3 maximum-likelihood methods in quantum mechanics,"
in *Quantum state estimation*, edited by M. Paris and J. Řeháček (Springer Berlin Heidelberg, Berlin, Heidelberg, 2004), pp. 59–112.

113 A. Jamiołkowski:
"Linear transformations which preserve trace and positive semidefiniteness of operators,"
Reports on Mathematical Physics **3**, 275–278 (1972).

114 M.-D. Choi:
"Completely positive linear maps on complex matrices,"
Linear Algebra and its Applications **10**, 285–290 (1975).

115 M. Ježek, J. Fiurášek, and Z. Hradil:
"Quantum inference of states and processes,"
Phys. Rev. A **68**, 012305 (2003).

116 M. D. de Burgh, N. K. Langford, A. C. Doherty, and A. Gilchrist:
"Choice of measurement sets in qubit tomography,"
Phys. Rev. A **78**, 052122 (2008).

117 Y. I. Bogdanov, G. Brida, M. Genovese, S. P. Kulik, E. V. Moreva, and A. P. Shurupov:
"Statistical estimation of the efficiency of quantum state tomography protocols,"
Phys. Rev. Lett. **105**, 010404 (2010).

118 Y. I. Bogdanov, G. Brida, I. D. Bukeev, M. Genovese, K. S. Kravtsov, S. P. Kulik, E. V. Moreva, A. A. Soloviev, and A. P. Shurupov:
"Statistical estimation of the quality of quantum-tomography protocols,"
Phys. Rev. A **84**, 042108 (2011).

119 C. Schwemmer et al.:
"Systematic errors in current quantum state tomography tools,"
Phys. Rev. Lett. **114**, 080403 (2015).

120 R. Stárek:
Qolo snippets,
https://github.com/RobStarek/, 2020.

121 A. Peres:
"Separability criterion for density matrices,"
Phys. Rev. Lett. **77**, 1413–1415 (1996).

122 W. K. Wootters:
"Entanglement of formation of an arbitrary state of two qubits,"
Phys. Rev. Lett. **80**, 2245–2248 (1998).

123 M. Lewenstein, B. Kraus, J. I. Cirac, and P. Horodecki:
"Optimization of entanglement witnesses,"
Phys. Rev. A **62**, 052310 (2000).

124 G. Tóth and O. Gühne:
"Detecting genuine multipartite entanglement with two local measurements,"
Phys. Rev. Lett. **94**, 060501 (2005).

125 R. H. BROWN and R. Q. TWISS:
"Correlation between photons in two coherent beams of light,"
Nature **177**, 27–29 (1956).

126 J. Wittenburg,
Multibody System Dynamics **9**, 353–375 (2003).

127 T. C. Ralph, N. K. Langford, T. B. Bell, and A. G. White:
"Linear optical controlled-not gate in the coincidence basis,"
Phys. Rev. A **65**, 062324 (2002).

128 H. F. Hofmann and S. Takeuchi:
"Quantum phase gate for photonic qubits using only beam splitters and postselection,"
Phys. Rev. A **66**, 024308 (2002).

129 I. Straka:
"Optical frequency conversion and non-classical light generation,"
PhD thesis (Palacky University Olomouc, 2012).

130 X.-Q. Zhou, T. C. Ralph, P. Kalasuwan, M. Zhang, A. Peruzzo, B. P. Lanyon, and J. L. O'Brien:
"Adding control to arbitrary unknown quantum operations,"
Nature Communications **2**, 10.1038/ncomms1392 (2011).

131 L. Bartůšková, A. Černoch, R. Filip, J. Fiurášek, J. Soubusta, and M. Dušek:
"Optical implementation of the encoding of two qubits to a single qutrit,"
Phys. Rev. A **74**, 022325 (2006).

132 C. Vitelli, N. Spagnolo, L. Aparo, F. Sciarrino, E. Santamato, and L. Marrucci:
"Joining the quantum state of two photons into one,"
Nature Photonics **7**, 521–526 (2013).

133 S. K. Goyal and T. Konrad:
"Teleporting photonic qudits using multimode quantum scissors,"
Scientific Reports **3**, 10.1038/srep03548 (2013).

134 M. Bielak, R. Stárek, V. Krčmarský, M. Mičuda, and M. Ježek:
Accurate polarization preparation and measurement using liquid crystal displays,
2020.

135 A. M. Brańczyk, D. H. Mahler, L. A. Rozema, A. Darabi, A. M. Steinberg, and D. F. V. James:
"Self-calibrating quantum state tomography,"
New Journal of Physics **14**, 085003 (2012).

136 R. Hošák, R. Stárek, and M. Ježek:
"Optimal reordering of measurements for photonic quantum tomography,"
Opt. Express **26**, 32878–32887 (2018).

137 A. Černoch, J. Soubusta, L. Bartůšková, M. Dušek, and J. Fiurášek:
"Experimental realization of linear-optical partial swap gates,"
Phys. Rev. Lett. **100**, 180501 (2008).

138 R. B. Patel, J. Ho, F. Ferreyrol, T. C. Ralph, and G. J. Pryde:
"A quantum fredkin gate,"
Science Advances **2**, 10.1126/sciadv.1501531 (2016).

139 B. Schumacher:
"Sending entanglement through noisy quantum channels,"
Phys. Rev. A **54**, 2614–2628 (1996).

140 M. Horodecki, P. Horodecki, and R. Horodecki:
"General teleportation channel, singlet fraction, and quasidistillation,"
Phys. Rev. A **60**, 1888–1898 (1999).

141 M. Horodecki, P. Horodecki, and R. Horodecki:
"Separability of mixed states: necessary and sufficient conditions,"
Physics Letters A **223**, 1–8 (1996).

142 B. M. Terhal:
"Bell inequalities and the separability criterion,"
Physics Letters A **271**, 319–326 (2000).

143 B. Jungnitsch, T. Moroder, and O. Gühne:
"Entanglement witnesses for graph states: general theory and examples,"
Phys. Rev. A **84**, 032310 (2011).

144 B. Jungnitsch, S. Niekamp, M. Kleinmann, O. Gühne, H. Lu, W.-B. Gao, Y.-A. Chen, Z.-B. Chen, and J.-W. Pan:
"Increasing the statistical significance of entanglement detection in experiments,"
Phys. Rev. Lett. **104**, 210401 (2010).

145 O. Moussa, M. P. da Silva, C. A. Ryan, and R. Laflamme:
"Practical experimental certification of computational quantum gates using a twirling procedure,"
Phys. Rev. Lett. **109**, 070504 (2012).

146 D. Lu, H. Li, D.-A. Trottier, J. Li, A. Brodutch, A. P. Krismanich, A. Ghavami, G. I. Dmitrienko, G. Long, J. Baugh, and R. Laflamme:
"Experimental estimation of average fidelity of a clifford gate on a 7-qubit quantum processor,"
Phys. Rev. Lett. **114**, 140505 (2015).

147 T. Monz, K. Kim, A. S. Villar, P. Schindler, M. Chwalla, M. Riebe, C. F. Roos, H. Häffner, W. Hänsel, M. Hennrich, and R. Blatt:
"Realization of universal ion-trap quantum computation with decoherence-free qubits,"
Phys. Rev. Lett. **103**, 200503 (2009).

148 S. Giacomini, F. Sciarrino, E. Lombardi, and F. De Martini:
"Active teleportation of a quantum bit,"
Phys. Rev. A **66**, 030302 (2002).

149 M. Riebe, H. Häffner, C. F. Roos, W. Hänsel, J. Benhelm, G. P. T. Lancaster, T. W. Körber, C. Becher, F. Schmidt-Kaler, D. F. V. James, and R. Blatt:
"Deterministic quantum teleportation with atoms,"
Nature **429**, 734–737 (2004).

150 R. Prevedel, P. Walther, F. Tiefenbacher, P. Böhi, R. Kaltenbaek, T. Jennewein, and A. Zeilinger:
"High-speed linear optics quantum computing using active feed-forward,"
Nature **445**, 65–69 (2007).

151 M. Miková, H. Fikerová, I. Straka, M. Mi čuda, J. Fiurá šek, M. Je žek, and M. Du šek:
"Increasing efficiency of a linear-optical quantum gate using electronic feed-forward,"
Phys. Rev. A **85**, 012305 (2012).

152 L. Steffen, Y. Salathe, M. Oppliger, P. Kurpiers, M. Baur, C. Lang, C. Eichler, G. Puebla-Hellmann, A. Fedorov, and A. Wallraff:
"Deterministic quantum teleportation with feed-forward in a solid state system,"
Nature **500**, 319–322 (2013).

153 W. Pfaff, B. J. Hensen, H. Bernien, S. B. van Dam, M. S. Blok, T. H. Taminiau, M. J. Tiggelman, R. N. Schouten, M. Markham, D. J. Twitchen, and R. Hanson:
"Unconditional quantum teleportation between distant solid-state quantum bits,"
Science **345**, 532–535 (2014).

154 C. H. Bennett, D. P. DiVincenzo, P. W. Shor, J. A. Smolin, B. M. Terhal, and W. K. Wootters:
"Remote state preparation,"
Phys. Rev. Lett. **87**, 077902 (2001).

155 K. Roszak, R. Filip, and T. Novotný:
"Decoherence control by quantum decoherence itself,"
Scientific Reports **5**, 10.1038/srep09796 (2015).

156 M. Ziman, P. Štelmachovič, V. Bužek, M. Hillery, V. Scarani, and N. Gisin:
"Diluting quantum information: an analysis of information transfer in system-reservoir interactions,"
Phys. Rev. A **65**, 042105 (2002).

157 M.-C. Chen, H.-S. Zhong, Y. Li, D. Wu, X.-L. Wang, L. Li, N.-L. Liu, C.-Y. Lu, and J.-W. Pan:
"Emergence of classical objectivity of quantum darwinism in a photonic quantum simulator,"
Science Bulletin **64**, 580–585 (2019).

158 A. N. Korotkov and K. Keane:
"Decoherence suppression by quantum measurement reversal,"
Phys. Rev. A **81**, 040103 (2010).

159 Y.-S. Kim, J.-C. Lee, O. Kwon, and Y.-H. Kim:
"Protecting entanglement from decoherence using weak measurement and quantum measurement reversal,"
Nature Physics **8**, 117–120 (2012).

160 J. M. Taylor, A. Imamoglu, and M. D. Lukin:
"Controlling a mesoscopic spin environment by quantum bit manipulation,"
Phys. Rev. Lett. **91**, 246802 (2003).

161 W. Yao, R.-B. Liu, and L. J. Sham:
"Restoring coherence lost to a slow interacting mesoscopic spin bath,"
Phys. Rev. Lett. **98**, 077602 (2007).

162 P. Cappellaro, L. Jiang, J. S. Hodges, and M. D. Lukin:
"Coherence and control of quantum registers based on electronic spin in a nuclear spin bath,"
Phys. Rev. Lett. **102**, 210502 (2009).

163 H. Bluhm, S. Foletti, D. Mahalu, V. Umansky, and A. Yacoby:
"Enhancing the coherence of a spin qubit by operating it as a feedback loop that controls its nuclear spin bath,"
Phys. Rev. Lett. **105**, 216803 (2010).

164 G.-Q. Liu, H. C. Po, J. Du, R.-B. Liu, and X.-Y. Pan:
"Noise-resilient quantum evolution steered by dynamical decoupling,"
Nature Communications **4**, 10.1038/ncomms3254 (2013).

165 J. Hansom, C. H. H. Schulte, C. L. Gall, C. Matthiesen, E. Clarke, M. Hugues, J. M. Taylor, and M. Atatüre:
"Environment-assisted quantum control of a solid-state spin via coherent dark states,"
Nature Physics **10**, 725–730 (2014).

166 D. Lv, S. An, Z. Liu, J.-N. Zhang, J. S. Pedernales, L. Lamata, E. Solano, and K. Kim:
"Quantum simulation of the quantum rabi model in a trapped ion,"
Phys. Rev. X **8**, 021027 (2018).

167 C. Flühmann, T. L. Nguyen, M. Marinelli, V. Negnevitsky, K. Mehta, and J. P. Home:
"Encoding a qubit in a trapped-ion mechanical oscillator,"
Nature **566**, 513–517 (2019).

168 F. Yoshihara, T. Fuse, S. Ashhab, K. Kakuyanagi, S. Saito, and K. Semba:
"Superconducting qubit-oscillator circuit beyond the ultrastrong-coupling regime,"
Nature Physics **13**, 44–47 (2016).

169 N. K. Langford, R. Sagastizabal, M. Kounalakis, C. Dickel, A. Bruno, F. Luthi, D. J. Thoen, A. Endo, and L. DiCarlo:
"Experimentally simulating the dynamics of quantum light and matter at deep-strong coupling,"
Nature Communications **8**, 10.1038/s41467-017-01061-x (2017).

170 J. Braumüller, M. Marthaler, A. Schneider, A. Stehli, H. Rotzinger, M. Weides, and A. V. Ustinov:
"Analog quantum simulation of the rabi model in the ultra-strong coupling regime,"
Nature Communications **8**, 10.1038/s41467-017-00894-w (2017).

171 M. D. LaHaye, J. Suh, P. M. Echternach, K. C. Schwab, and M. L. Roukes:
"Nanomechanical measurements of a superconducting qubit,"
Nature **459**, 960–964 (2009).

172 J.-M. Pirkkalainen, S. U. Cho, J. Li, G. S. Paraoanu, P. J. Hakonen, and M. A. Sillanpää:
"Hybrid circuit cavity quantum electrodynamics with a micromechanical resonator,"
Nature **494**, 211–215 (2013).

173 M. V. Gustafsson, T. Aref, A. F. Kockum, M. K. Ekstrom, G. Johansson, and P. Delsing:
"Propagating phonons coupled to an artificial atom,"
Science **346**, 207–211 (2014).

174 H.-F. Wang, X.-Q. Shao, Y.-F. Zhao, S. Zhang, and K.-H. Yeon:
"Linear optical implementation of an ancilla-free quantum SWAP gate,"
Physica Scripta **81**, 015011 (2010).

175 W.-A. Li:
"Quantum swap gate with atomic ensembles in two distant cavities,"
Optics Communications **284**, 685–690 (2011).

176 M.-Z. Zhu and L. Ye:
"Implementation of swap gate and fredkin gate using linear optical elements,"
International Journal of Quantum Information **11**, 1350031 (2013).

177 J. C. Garcia-Escartin and P. Chamorro-Posada:
"A SWAP gate for qudits,"
Quantum Information Processing **12**, 3625–3631 (2013).

178 M. Fiorentino and F. N. C. Wong:
"Deterministic controlled-not gate for single-photon two-qubit quantum logic,"
Phys. Rev. Lett. **93**, 070502 (2004).

179 M. Ježek:
30 ms optical shutter using rc servo,
http://quantum.opticsolomouc.org/archives/1177, 2012.

180 A. K. Ekert, C. M. Alves, D. K. L. Oi, M. Horodecki, P. Horodecki, and L. C. Kwek:
"Direct estimations of linear and nonlinear functionals of a quantum state,"
Phys. Rev. Lett. **88**, 217901 (2002).

181 R. Filip:
"Overlap and entanglement-witness measurements,"
Phys. Rev. A **65**, 062320 (2002).

182 S. M. Lee, S.-K. Choi, and H. S. Park:
"Experimental direct estimation of nonlinear functionals of photonic quantum states via interferometry with a controlled-swap operation,"
Optics Express **21**, 17824 (2013).

183 M. Dušek and V. Bužek:
"Quantum-controlled measurement device for quantum-state discrimination,"
Phys. Rev. A **66**, 022112 (2002).

184 J. Fiurášek, M. Dušek, and R. Filip:
"Universal measurement apparatus controlled by quantum software,"
Phys. Rev. Lett. **89**, 190401 (2002).

185 T. Ono, R. Okamoto, M. Tanida, H. F. Hofmann, and S. Takeuchi:
"Implementation of a quantum controlled-SWAP gate with photonic circuits,"
Scientific Reports **7**, 10.1038/srep45353 (2017).

186 M. Hendrych, M. Dušek, R. Filip, and J. Fiurášek:
"Simple optical measurement of the overlap and fidelity of quantum states,"
Physics Letters A **310**, 95–100 (2003).

187 R. B. A. Adamson, L. K. Shalm, and A. M. Steinberg:
"Preparation of pure and mixed polarization qubits and the direct measurement of figures of merit,"
Phys. Rev. A **75**, 012104 (2007).

188 J. I. Cirac, A. K. Ekert, and C. Macchiavello:
"Optimal purification of single qubits,"
Phys. Rev. Lett. **82**, 4344–4347 (1999).

189 M. Ricci, F. D. Martini, N. J. Cerf, R. Filip, J. Fiurá šek, and C. Macchiavello:
"Experimental purification of single qubits,"
Phys. Rev. Lett. **93**, 170501 (2004).

190 V. Bužek and M. Hillery:
"Quantum copying: beyond the no-cloning theorem,"
Phys. Rev. A **54**, 1844–1852 (1996).

191 V. Scarani, S. Iblisdir, N. Gisin, and A. Acín:
"Quantum cloning,"
Rev. Mod. Phys. **77**, 1225–1256 (2005).

192 N. J. Cerf and J. Fiurášek:
"Optical quantum cloning,"
in *Progress in optics* (Elsevier, 2006), pp. 455–545.

193 R. F. Werner:
"Optimal cloning of pure states,"
Phys. Rev. A **58**, 1827–1832 (1998).

194 M. Ricci, F. Sciarrino, C. Sias, and F. De Martini:
"Teleportation scheme implementing the universal optimal quantum cloning machine and the universal not gate,"
Phys. Rev. Lett. **92**, 047901 (2004).

195 A. Černoch, J. Soubusta, L. Bartůšková, M. Dušek, and J. Fiurášek:
"Experimental implementation of partial symmetrization and anti-symmetrization of two-qubit states,"
New Journal of Physics **11**, 023005 (2009).

196 M. A. Nielsen and I. L. Chuang:
"Programmable quantum gate arrays,"
Phys. Rev. Lett. **79**, 321–324 (1997).